MISSILE IMPACT CRATERS (WHITE SANDS MISSILE RANGE, NEW MEXICO) AND APPLICATIONS TO LUNAR RESEARCH

CONTRIBUTIONS
TO
ASTROGEOLOGY

GEOLOGICAL SURVEY PROFESSIONAL PAPER 812-B

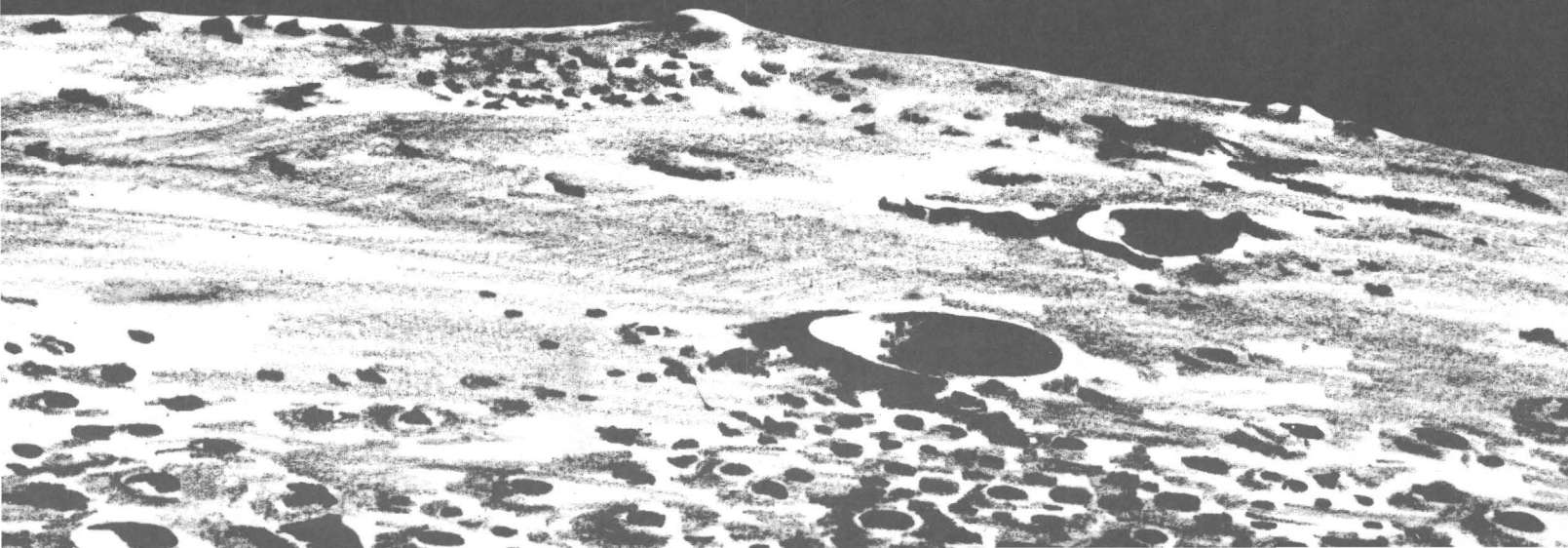

MISSILE IMPACT CRATERS (WHITE SANDS MISSILE RANGE, NEW MEXICO) AND APPLICATIONS TO LUNAR RESEARCH

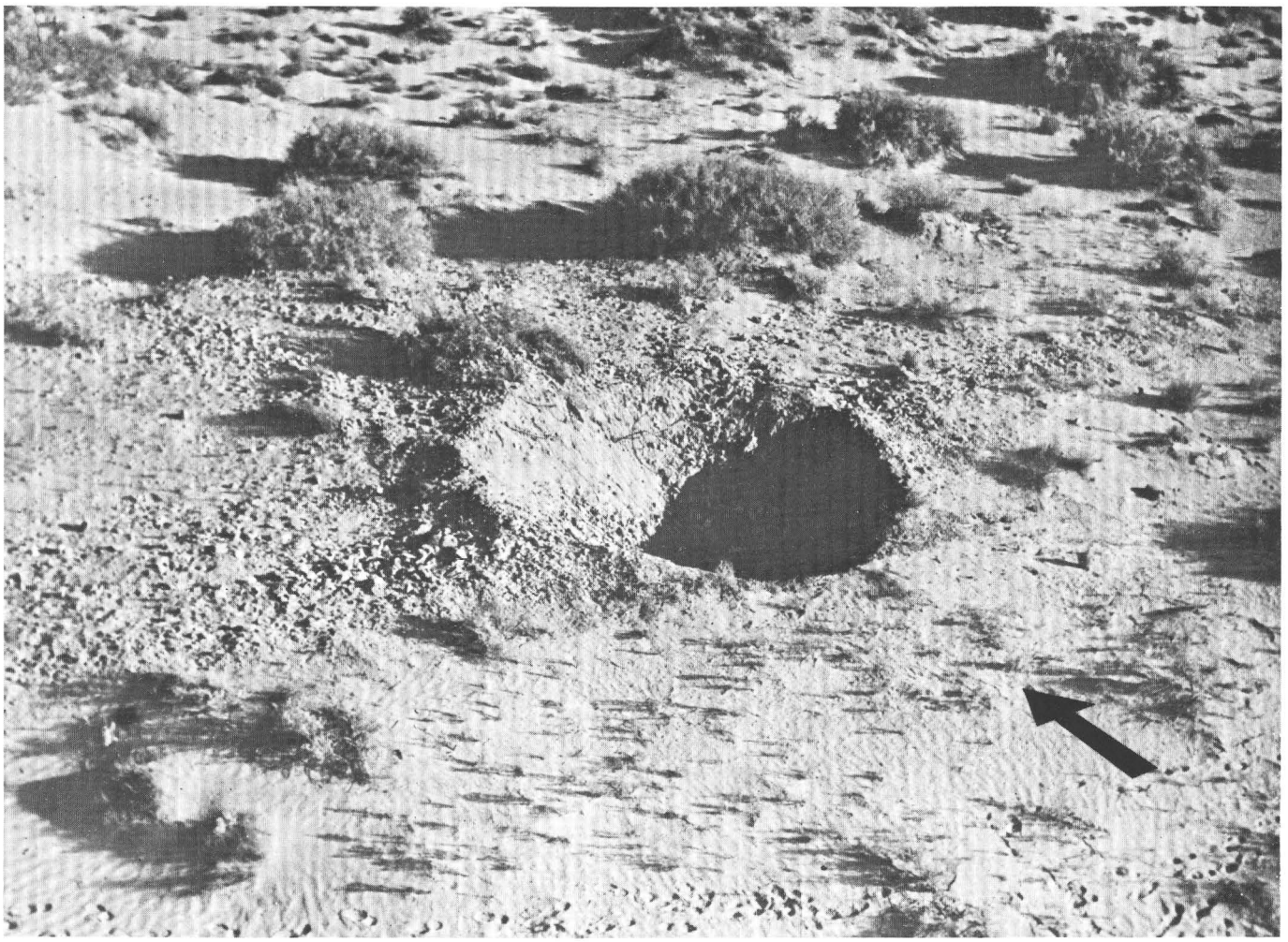

Crater produced by missile impact in silty sand and sandy silt, oblique view. Missile traveled along an oblique trajectory, 45.8° from the horizontal with a kinetic energy of 25.1×10^{14} ergs. The crater, about 6 metres across, and ejecta have bilateral symmetry because of the oblique trajectory. Trace of path of missile is shown by arrow. Small depressions in foreground are footprints. Crater 24; photograph courtesy of U.S. Army.

Missile Impact Craters (White Sands Missile Range, New Mexico) and Applications to Lunar Research

By H. J. MOORE

CONTRIBUTIONS TO ASTROGEOLOGY

GEOLOGICAL SURVEY PROFESSIONAL PAPER 812-B

UNITED STATES GOVERNMENT PRINTING OFFICE, WASHINGTON : 1976

UNITED STATES DEPARTMENT OF THE INTERIOR

THOMAS S. KLEPPE, *Secretary*

GEOLOGICAL SURVEY

V. E. McKelvey, *Director*

Library of Congress Cataloging in Publication Data

Moore, Henry J.
Missile impact craters (White Sands Missile Range, New Mexico) and their applications to lunar research. (Contributions to astrogeology)

(Geological Survey Professional Paper 812-B)
Bibliography: p. B41-B43.
Supt. of Docs. No.: I 19.16:812-B
1. Lunar craters. 2. Cryptoexplosion structures--New Mexico--White Sands region. 3. Lunar geology. 4. Guided missiles. I. Title: Missile impact craters. . . II. Series. III. Series: United States. Geological Survey. Professional Paper 812-B.
QB591.M57 551.3 75-619096

For sale by the Superintendent of Documents, U.S. Government Printing Office
Washington, D.C. 20402

Stock Number 024-001-02786-1

CONTENTS

ILLUSTRATIONS

TABLES

METRIC-ENGLISH EQUIVALENTS

Metric unit		English equivalent	
Length			
millimetre (mm)	=	0.03937	inch (in)
metre (m)	=	3.28	feet (ft)
kilometre (km)	=	.62	mile (mi)
Area			
square metre (m^2)	=	10.76	square feet (ft^2)
square kilometre (km^2)	=	.386	square mile (mi^2)
hectare (ha)	=	2.47	acres
Volume			
cubic centimetre (cm^3)	=	0.061	cubic inch (in^3)
litre (l)	=	61.03	cubic inches
cubic metre (m^3)	=	35.31	cubic feet (ft^3)
cubic metre	=	.00081	acre-foot (acre-ft)
cubic hectometre (hm^3)	=	810.7	acre-feet
litre	=	2.113	pints (pt)
litre	=	1.06	quarts (qt)
litre	=	.26	gallon (gal)
cubic metre	=	.00026	million gallons (Mgal or 10^6 gal)
cubic metre	=	6.290	barrels (bbl) (1 bbl=42 gal)
Weight			
gram (g)	=	0.035	ounce, avoirdupois (oz avdp)
gram	=	.0022	pound, avoirdupois (lb avdp)
tonne (t)	=	1.1	tons, short (2,000 lb)
tonne	=	.98	ton, long (2,240 lb)
Specific combinations			
kilogram per square centimetre (kg/cm^2)	=	0.96	atmosphere (atm)
kilogram per square centimetre	=	.98	bar (0.9869 atm)
cubic metre per second (m^3/s)	=	35.3	cubic feet per second (ft^3/s)
litre per second (l/s)	=	.0353	cubic foot per second
cubic metre per second per square kilometre [$(m^3/s)/km^2$]	=	91.47	cubic feet per second per square mile [$(ft^3/s)/mi^2$]
metre per day (m/d)	=	3.28	feet per day (hydraulic conductivity) (ft/d)
metre per kilometre (m/km)	=	5.28	feet per mile (ft/mi)
kilometre per hour (km/h)	=	.9113	foot per second (ft/s)
metre per second (m/s)	=	3.28	feet per second
metre squared per day (m^2/d)	=	10.764	feet squared per day (ft^2/d) (transmissivity)
cubic metre per second (m^3/s)	=	22.826	million gallons per day (Mgal/d)
cubic metre per minute (m^3/min)	=	264.2	gallons per minute (gal/min)
litre per second (l/s)	=	15.85	gallons per minute
litre per second per metre [(l/s)/m]	=	4.83	gallons per minute per foot [(gal/min)/ft]
kilometre per hour (km/h)	=	.62	mile per hour (mi/h)
metre per second (m/s)	=	2.237	miles per hour
gram per cubic centimetre (g/cm^3)	=	62.43	pounds per cubic foot (lb/ft^3)
gram per square centimetre (g/cm^2)	=	2.048	pounds per square foot (lb/ft^2)
gram per square centimetre	=	.0142	pound per square inch (lb/in^2)
Temperature			
degree Celsius (°C)	=	1.8	degrees Fahrenheit (°F)
degrees Celsius (temperature)	=	[(1.8×°C)+32]	degrees Fahrenheit

MISSILE IMPACT CRATERS (WHITE SANDS MISSILE RANGE, NEW MEXICO) AND APPLICATIONS TO LUNAR RESEARCH

By H. J. MOORE

ABSTRACT

Craters in natural materials at White Sands Missile Range, N. Mex., were produced by the impact of high-velocity to hypervelocity missiles traveling along oblique trajectories with kinetic energies between 2.1 and 81×10^{14} ergs. The oblique impacts produce craters 2 to 10 m across with morphologies and ejecta that are bilaterally symmetrical with respect to the plane of the missile trajectory. Rims are high and the amount of ejecta large in down-trajectory and lateral directions, whereas rims are low to nonexistent and ejecta thin to absent up-trajectory. Symmetry development and modifications of the symmetry are a function of target material, local topography, and angle of impact.

Seven mappable units can be recognized in and around the craters. Three of these are ejecta: *thick ejecta* near the crater, *thin to discontinuous ejecta* at greater distances, and *scattered* ejecta at the greatest distances to the limit of throwout. These ejecta units may be absent on the up-trajectory side; if present, they are rarely as thick or continuous as on other sides of the crater. Three units are target materials: *undeformed target material* exposed in local patches through thin to discontinuous ejecta and everywhere between the fragments of scattered ejecta, *tilted and broken target material* exposed in upper crater walls, and *shattered and fractured target material* exposed on the up-trajectory crater wall. The seventh unit is *slope material* composed of talus and fallback within the crater. Development, character, and exposure of these units varies chiefly with the target material.

Ejecta from the craters is chiefly broken but relatively undeformed target material that may range in size from very fine grained debris to large blocks. Where the target is porous, significant amounts of the ejecta are composed of sheared and compressed fragments, some coated with dark layers of mixed projectile pieces, powder, and fused metal mixed with crushed target material. For layered targets, the original stratigraphic sequence is crudely preserved and in inverted order in thick ejecta.

Secondary impact craters are produced by the impact of ejected fragments when the surrounding surface materials are sufficiently weak. A wide variety of secondary impact crater relations may result. Secondary craters nearest the primary crater have blocks in them that are larger than or the same size as the crater they produced. Farther from the primary crater, the fragments are generally smaller than the secondary crater and are ejected from it.

Excavation of four craters revealed a mixed breccia beneath the crater floor composed of missile pieces, sheared and compressed target material, and crushed debris. Banded, disaggregated target material and nonmixed breccia surrounded the mixed breccia, and these breccias were surrounded by a zone of conjugate fractures. Beneath the ejecta on the lateral and down-trajectory crater flanks, the target materials were tilted upward and broken. Up-trajectory, open fractures and downward displacement occurred in two of the craters. No displacement was observed for the other two.

Beneath the down-trajectory rims of craters with distinct layering, overturned synclines were observed.

Missile breakup and behavior during cratering are a function of target and missile properties. Missile breakup depends on missile velocity and is most extensive at high velocities, where the missile is fragmented, powdered, and partly fused. Burial of missile or its fragmented, powdered, and fused remains is greatest for porous targets and least for dense cohesive targets. For very porous targets, camouflet structures containing the fragmented missile may form.

Least squares fit to the data on craters in dry to moist targets indicate

$$V_a = 10^{-11.433} E_p^{1.205},$$

where V_a is the volume of the apparent crater and E_p is the kinetic energy of the missile. This equation is consistent with expectations of the equations relating apparent depth and radius to kinetic energy. Extrapolation of displaced masses and kinetic energies for laboratory impacts with sand and rock converge near 10^{15} to 10^{16} ergs, where the extrapolations are near the data on missile impact craters, corrected for impact angle.

Displaced masses of craters produced by missile impacts and by chemical explosives with small scaled depths of burial are about the same when the kinetic energies of the missiles (corrected for angle of impact) are equal to the TNT equivalent energy of the explosive. The problem of equivalent scaled depth of burst for an impact crater is complicated and not entirely resolved, however. Both missile impact craters and chemical explosive craters in water-saturated targets are larger than their counterparts in dry to moist materials.

Data collected during the study of missile impact craters have helped resolve a number of problems in lunar research: (1) the soillike nature of lunar surface materials was predicted, (2) sizes of craters produced by artificial impacts were correctly predicted, (3) certain features imaged by Surveyor were found to be analogous to features associated with missile impact craters, (4) missile impacts were used in support of the Apollo passive seismic experiment, (5) craters seen in Apollo orbital photographs were found to be similar to some missile impact craters, (6) missile impact craters supplied data on sample collection and crater phenomenology used in training astronauts, and (7) some returned lunar samples are similar to coated, sheared, and compressed fragments ejected from missile impact craters.

INTRODUCTION

The advent of lunar exploration with manned and unmanned spacecraft brought renewed interest in experimental and natural craters produced by projectile impacts in natural materials. Experiments producing

craters by the impact of low-velocity projectiles with clay, powder, and mud were employed by early investigators in their lunar studies (for example, Hooke, 1664, p. 242–246; Meydenbauer, 1882; Gilbert, 1893). Later, morphologies of craters produced by bombs with explosive warheads were compared with morphologies of lunar craters (Ives, 1919, and Baldwin, 1949). Baldwin (1949, 1963) included craters with shallow depths of burial in his lunar studies and estimated the energy required to produce Meteor Crater in Arizona. Shoemaker (1960, 1962) mapped and studied craters produced by nuclear explosives with shallow depths of burial, compared them structurally with Meteor Crater, then developed a ballistics model that accounts for ejecta from lunar craters.

Light-gas guns capable of accelerating projectiles to velocities exceeding 7.0 km/s (Curtis, 1962, Charters and others, 1957) permitted experimentation with targets of rock and sand under conditions where high pressures were attained during impact cratering (Charters, 1960; Shoemaker and others, 1963; Moore and others, 1962; Moore and others, 1964a; Gault and others, 1965; and Oberbeck, 1970). Most of the craters in these experiments were 1.0 to 70 cm or so across. Microparticle accelerators provided data on micrometre-size impact craters (Mandeville and Vedder, 1971). These data have been applied to lunar studies in many ways.

PURPOSE AND SCOPE OF REPORT

Studies of more than 50 craters produced by the impact of missiles were conducted by the U.S. Geological Survey at White Sands Missile Range, N. Mex., from February 1964 to January 1973. The purposes of these studies were to extend our knowledge of hypervelocity experimental impact craters in natural terrestrial materials to large craters produced by projectiles with large kinetic energies, to compare the dimensions and characteristics of the impact craters with craters produced by chemical explosives, and to apply the knowledge gained from the impact craters to lunar problems. This paper provides data on missile impact craters 2 to 10 m across produced in natural materials by missiles with kinetic energies between 2.1×10^{14} and 81×10^{14} ergs traveling along oblique trajectories.

Information released earlier on missile impact craters is available in preliminary status reports and short papers (Moore, 1971a, 1969, 1968a, 1966a, b, c; Moore and Lugn, 1965; Moore and others, 1964a; Moore and others, 1968; Moore and others, 1967; Latham and others, 1970) that present preliminary results and interpretations, some of which have been modified since the reports were written.

FIELDWORK

Fieldwork was begun in February 1964 by Reuben Kachadoorian of the U.S. Geological Survey, who studied the first three impact craters. H. J. Moore mapped and studied two craters in April 1964. Fieldwork continued through January 1973, conducted primarily by H. J. Moore, Reuben Kachadoorian, and Peter Margolin of the U.S. Geological Survey.

ACKNOWLEDGMENTS

The Command at White Sands Missile Range, N. Mex., made this study possible by allowing access to the craters, furnishing kinetic energies and angles of impact of the missiles, providing ground and aerial photography, and helping in countless other ways. Without this support, the study could not have been conducted.

The author wishes to specifically acknowledge the contributions of the following individuals who were within the Command at White Sands during the study: Paul K. Arthur, Robert E. Ball, Carlos A. Bustamonte, Donald Cramer, Captain Ronald J. Hoekzema, S. V. Jennings, Johnnie G. Losack, Frank A. McKenna, Eli H. Mabry, John J. Ofenloch, Major George Wallace, and many others. Valuable help was furnished by the Inland Range Field Office in particular by Captain John Thau and Lt. James Forman. The many geologists of the U.S. Geological Survey and other individuals who helped in mapping of craters are acknowledged in table 2 (p.B25). Sustained mapping by Reuben Kachadoorian and Peter Margolin is especially appreciated. During the early phases of the study aid was given by Donald E. Gault, William L. Quaide, and Verne R. Oberbeck, of Ames Research Center, National Aeronautics and Space Administration, Moffett Field, Calif. Richard V. Lugn and Francis G. Robertson provided useful support in drafting, planimetry, and measurements of densities and moisture contents of samples. Experiments using commercial explosives were designed and performed by Gary V. Latham, Arthur McGarr, and William G. McDonald, of the Lamont-Doherty Geological Observatory of Columbia University. Work was performed under NASA contracts R–66 and W–13,130.

In addition to the photography furnished by the Command at White Sands, vertical photography and imagery of selected craters was obtained using color, black and white, and ultraviolet film and an infrared scanner by the Natural Resources Program Remote Sensing Aircraft (NASA 926 CV 240A) piloted by Kenneth Haugen of the Manned Spacecraft Center, Houston, Tex.

The U.S. National Park Service allowed access to several craters.

PROCEDURES

SUPPORT DATA

Data on kinetic energies and angles of impact were supplied by the Command at White Sands from known masses, velocities, and trajectories of the missiles. When unclassified, measured velocities and masses of the missiles were furnished.

MAPPING

Topographic maps of the craters were prepared using a telescopic alidade, planetable, stadia rod, and tape at scales of 1:24 to 1:48, depending on the size of the crater. Part of the ejecta and limits of throwout were mapped at smaller scales. Some mapping was facilitated using photography and imagery furnished by the Command at White Sands Missile Range and the Earth Resources Program of NASA. Cross sections along trenches were prepared using a planetable, alidade, and tape for primary control. A stretched tape was used to fill in details.

Crater dimensions were obtained from the topographic maps. Crater volumes were calculated using areas obtained with a compensating planimeter from the topographic maps and the known contour interval. Dimensions taken from images were measured directly on the images, then computed using scales obtained by comparing lengths between image points and measured distances between corresponding points on the ground.

TARGET MATERIALS

Target materials ranged widely in their physical properties; they include rock, cohesive gypsum sand (fixed gypsum dunes), lake beds, alluvium, colluvium, soils, and sand. In general, target materials were dry to moist but some lake beds were water-saturated. In table 2 target materials for each crater are briefly described using the Unified Soil Classification System (U.S. Army Corps of Engineers, 1953), along with geologic descriptions, densities, and moisture contents obtained using techniques outlined in the Earth Manual (U.S. Bureau of Reclamation, 1963). Special precautions had to be taken, because many of the target materials contained gypsum, which changes to water, basanite, and anhydrite when heated to 90°C and higher.

Measurements of target strength and changes in strength resulting from deformation were obtained using shear vanes, a small compression apparatus, and a shear box. Sound velocities were obtained for two target types using standard seismic equipment. Properties of target materials are summarized in table 1 insofar as possible.

EXPLOSIVES USED

Explosive experiments were designed and performed by Gary V. Latham, Art McGarr, and William McDonald of the Lamont-Doherty Geological Observatory of Columbia University, using 5 to 100 kg (11 to 220 lb) of sticks of Amogel 1 (Apache Powder Co.) and Amodyte 1 (Atlas Chemical Industries).[1] According to the manufacturers, the energy release of these explosives is about 3.9×10^{13} ergs/kg (1.77×10^{13} ergs/lb). By comparison, TNT yields about 4.2×10^{13} ergs/kg (1.9×10^{13} ergs/lb) (Nordyke and Wray, 1964, p. 675).

DEFINITIONS

A number of parameters are defined below and illustrated in figure 1.

TRAJECTORY TERMS

Path of missile: The line described by the inflight missile just before impact (BO).

Plane of trajectory: The plane defined by the path of the missile in flight and the local vertical (BOC).

Trace of missile: A line formed by the intersection of the plane of the trajectory and the local horizon-

[1]Mention of these companies and their products does not constitute an endorsement of them by the U.S. Geological Survey.

TABLE 1.—*General classification of target materials for missile impacts*

Target material	Moisture content	Bulk density, g/cm³	Sound velocity, km/s	Shear-vane strength[1], bars	Unified Soil Class
Water-saturated gypsum lake beds	Wet, up to 30 percent water	1.2–1.85	----	30 (1 m)	SM, SC, ML
Gypsum lake beds	Moist, 7–13 percent water	1.8–1.9	----	3.0 (s)	CL, ML
Fixed gypsum dunes	Dry, 1–7 percent water	1.37–1.56	0.93	0.8–4.0 (s) 3.0–6.0 (1 m)	ML
Colluvium	Dry, 1–7 percent water	1.2–1.8	----	0 (s) 2.0 (0.3 m)	SM ML
Alluvium and soil	Usually dry, 1–7 percent water	1.1–2.1	.25	0.5–2.0 (s) 5 –11.5 (1 m)	
Sand	Dry, 1–7 percent water	1.35–1.60	----	0 (s) 5 (1 m)	SW SP
Rock	Dry, no water	2.5	----	Very large	Rock

[1]Number in parenthesis is depth for shear-vane strength; s is near surface.

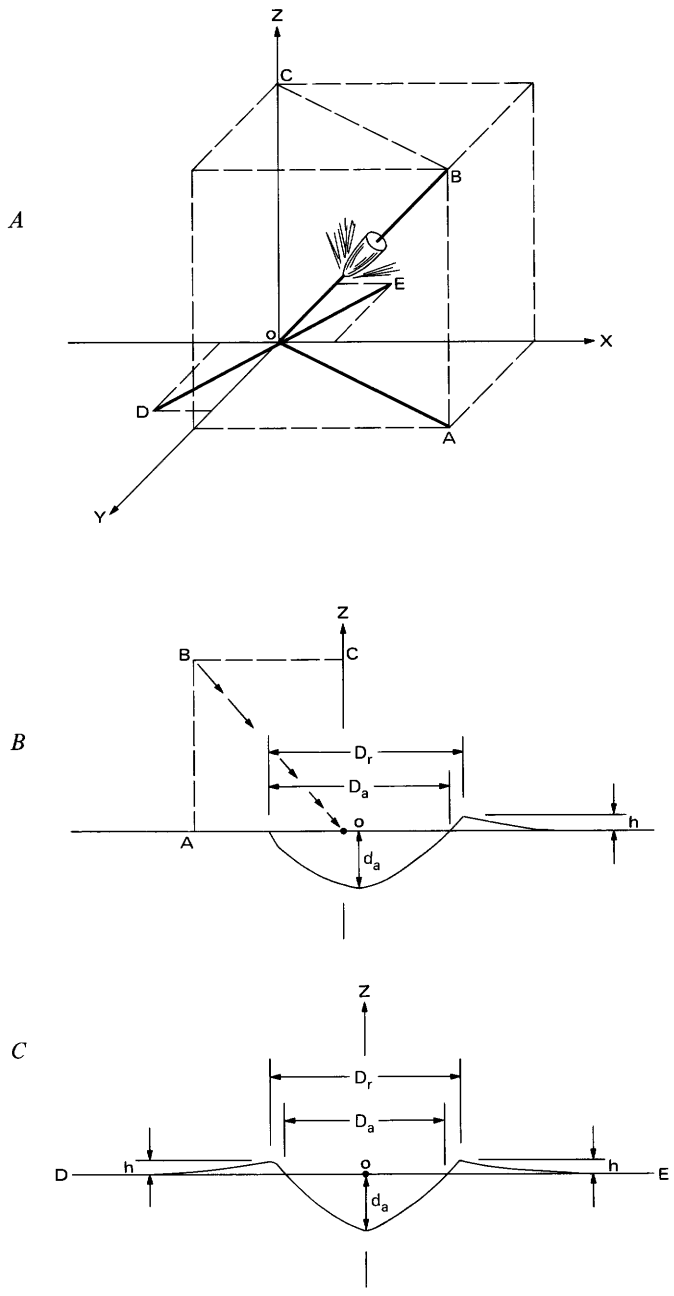

FIGURE 1.—Physical parameters, terms defined in text. *A*: BO, path of missile; AO, trace of missile; BOC, plane of trajectory; O to A, up-trajectory direction; A to O, down-trajectory direction; area near AO, beneath the trajectory; OD, OE, lateral directions; angle AOB, angle of impact; O, point of impact; z is vertical and x and y are horizontal. *B*: D_r, rim diameter; D_a, apparent diameter; d_a, apparent crater depth; h, rim height. *C*, Plane perpendicular to plane of trajectory.

tal plane, terminating at the point of impact (AO).

Up-trajectory: The general direction from the point of impact toward the origin or launch site of the missile (direction of OA ± several tens of degrees).

Down-trajectory: The general direction from the point of impact away from the origin or launch site of the missile (direction of AO ± several tens of degrees).

Beneath the trajectory: Areas near the crater that are below the path of the missile (near the line AO).

Lateral direction(s): The direction(s) from the point of impact more or less perpendicular to the plane of the trajectory (direction(s) of OD and OE ± several tens of degrees).

Angle of impact (Θ): The angle measured in the plane of trajectory between the local horizontal and the path of the missile at impact (angle AOB).

Kinetic energy of projectile (E_p): One-half the product of the mass and square of the velocity of the missile at impact.

CRATER TERMS

Rim diameter (D_r): The maximum distance measured across the crater along a line from one rim crest to the opposite rim crest or from the rim crest on the down-trajectory side of the crater to the crater edge on the up-trajectory side (where a rim may be absent) of the crater.

Rim radius (r_r): The sum of the rim diameter in the plane of the trajectory and the rim diameter normal to the trajectory plane divided by four.

Apparent diameter (D_a): The maximum distance measured across the crater along a line in the plane of the original ground surface from one side of the crater to the other.

Apparent radius (r_a): The sum of the apparent diameter in the plane of the trajectory and the apparent diameter normal to the trajectory plane divided by four.

Rim height (h): The elevation of the crater rim above the local original ground surface.

Average rim height ($\bar{h}$): The average of four elevations of the crater rim above the local original ground surface measured in the plane of the trajectory and at right angles to it.

Apparent crater depth (d_a): The depth of the crater measured from the projected original ground surface to the bottom of the crater.

Apparent crater volume (V_a): The volume of the crater below the original ground surface.

Displaced mass (M_d): The product of the original target density and apparent crater volume.

DESCRIPTION OF CRATERS

CRATER MORPHOLOGY

Crater morphology is a function of the missile trajectory, crater size, target material, and slope. As a

result of the oblique trajectories, the missile impact craters exhibit some bilateral symmetry about the plane of the trajectory (frontispiece). The average ratio of crater rim diameter along the trace of the missile, and the rim diameter perpendicular to it is 1.07 ± 0.17 (1σ), and values of the ratio ranged from 0.87 to 1.62. The craters are generally elongate parallel to the plane of the trajectory, but a substantial number of craters are elongate in directions perpendicular to the trajectory. Typically, crater rims are low to nonexistent beneath the trajectory and well developed on the down-trajectory side of the crater. Mean slopes of crater walls beneath the trajectory are commonly steeper than those on the opposite wall so that, in plan view, the deepest part of the crater is displaced up-trajectory with respect to the midpoint of the apparent diameter parallel to the trajectory plane. Crater flanks beneath the trajectory are commonly at the original ground surface, those on the down-trajectory side slope gently away from the elevated crater rim. Mirror image rims, crater walls, and gently outward-sloping crater flanks are found in the lateral directions. A topographic map of a typical missile impact crater is shown in figure 2.

Crater morphology changes with size. Large craters produced by missiles with oblique trajectories in cohesive targets tend to have elevated rims in all directions whereas small craters are commonly rimless beneath the trajectory. This tendency is well illustrated by craters in moist gypsum lake beds (figs. 3 and 4). Two small craters, 2.0–3.6 m across, are rimless on the up-trajectory side (see for example, fig. 3). All three large craters in the same material, 7.4 m across, have well-developed rims on the up-trajectory side (see for example fig. 4). Similar results are observed for impact and explosive craters in rock and cohesive materials. Centimetre- to metre-size craters in rock are rimless and large pie-shaped spalls are ejected from the crater (Moore and others, 1962; Gault and others, 1966; Hörz, 1969; Duvall and Atchison, 1957; Johnson, 1962). Large craters in rock, on the order of tens and hundreds of metres across, are surrounded by rims containing blocks of ejecta that are small relative to crater diameter (Nordyke and Wray, 1964; Shoemaker, 1960; Boutwell, 1928; Spruill and Paul, 1965).

Physical properties of the target materials partly control crater morphology, particularly for small craters. Small craters in cohesive rock tend to be rimless, whereas those in moderately cohesive alluvium, colluvium, and fixed gypsum dunes have well-developed rims in down-trajectory directions. Craters in nearly cohesionless materials such as sand have continuous rims, best developed in the lateral and down-trajectory directions and weakly developed up-trajectory (fig. 5). Profiles of craters in more cohesive materials have steep

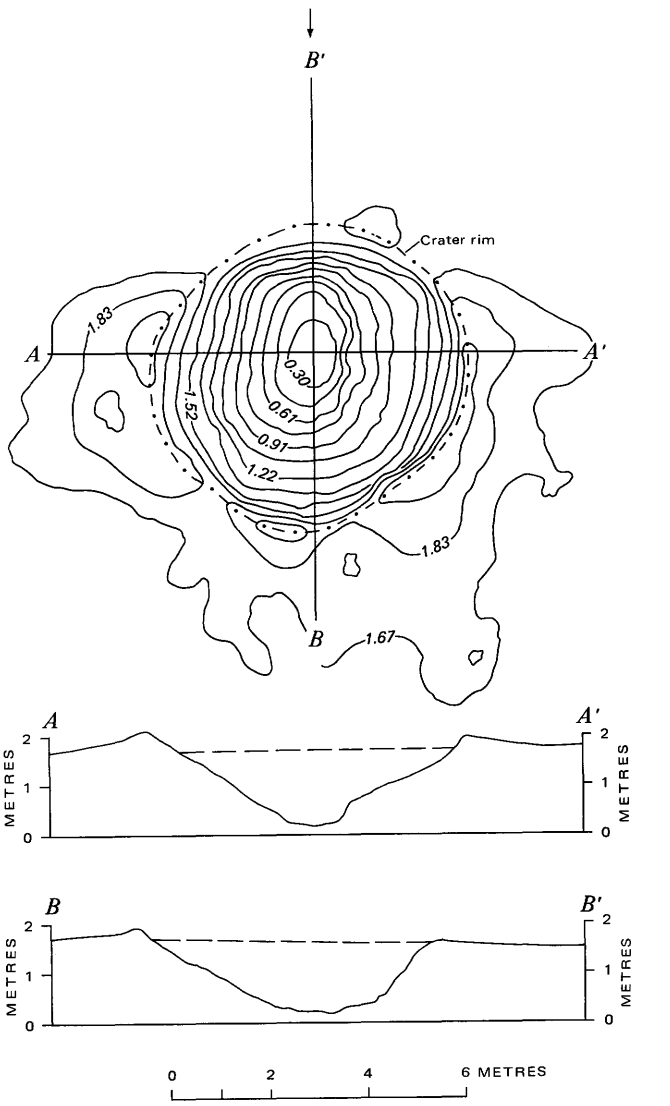

FIGURE 2.—Contour map and profiles illustrating bilateral symmetry of typical crater produced by missile impact in gypsiferous alluvium and fixed gypsum dune. Contour interval, 0.1525 m (½ ft). Arrow indicates trace of missile. The profile labeled B–B' is in the plane of the trajectory; A–A' is perpendicular to the plane of the trajectory. Dot-dash line represents crater rim; dashed lines in profile show original ground surface. Note steep wall on up-trajectory crater wall, symmetry of crater and rims in profile A–A' and lack of it in profile B–B', and bilateral symmetry of plan view. ($E_p = 19.7 \times 10^{14}$ ergs, $\Theta = 45.0°$. Crater 17.)

slopes, particularly in the upper part of the crater walls and on the up-trajectory wall (figs. 2, 3, and 4). For less cohesive targets such as sand and colluvium, craters tend to be conical (fig. 6). Rimless to nearly rimless craters may result when the target is very porous and moderately cohesive (crater 12). Small craters less than about 1 m across in materials with low cohesion, such as sand, produced by projectile impact in the laboratory (Gault and others, 1966) and by chemical explosives with small depths of burial (Oberbeck, 1971) are

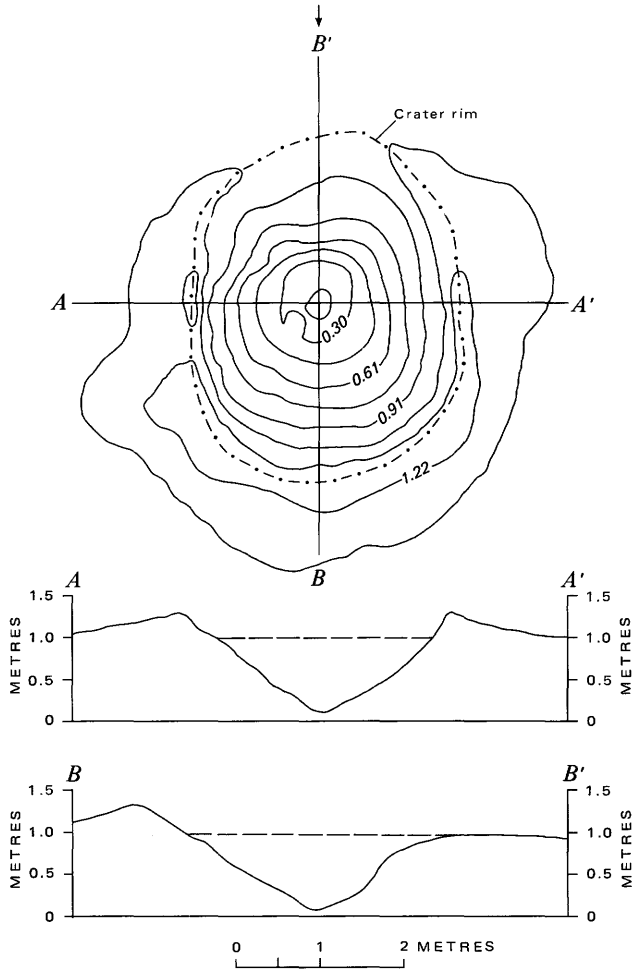

FIGURE 3.—Contour map and profiles illustrating partial rim and marked bilateral symmetry of small crater in gypsum lake beds produced by missile impact. Contour interval 0.1525 m (½ ft). Arrow indicates trace of missile. The profile *B–B'* is in the plane of the trajectory, *A–A'* is perpendicular to the plane of the trajectory. Dot-dash line on map represents crater rim; dashed lines in profiles show original ground surface. Note asymmetry of profile *B–B'*, absence of rim on up-trajectory side of crater, and symmetry of profile *A–A'*. (E_p=5.92×10^{14} ergs, Θ=51.0°. Crater 11.)

characterized by elevated continuous rims and conical shapes, although some have concentric structures on their floors (Fullmer, 1966).

For several missile impact craters on steep slopes (craters 2, 9, and 58), crater rims and flanks were low to nonexistent on the upslope part of the crater as well as on the up-trajectory side, and well developed downslope. Slope is thus shown to affect the symmetry of the craters.

MAP UNITS

Generally, seven mappable units are exposed in and around the craters (fig. 7). Three of these are ejecta units: thick ejecta (te), thin to discontinuous ejecta (td), and scattered ejecta (ts). Three are target materials: undeformed target material (tm), tilted and broken target material (tb), and shattered and fractured target material (sf). The seventh is slope material and debris on the crater floor (sm). These units, for a typical crater, are described below.

Thick ejecta is a blanket of debris with lobate extensions, about 5 to 30 cm thick, deposited from the crater rim to distances of several metres with bilateral symmetry about the plane of the trajectory (frontispiece and fig. 7). Normally, it is deposited in down-trajectory

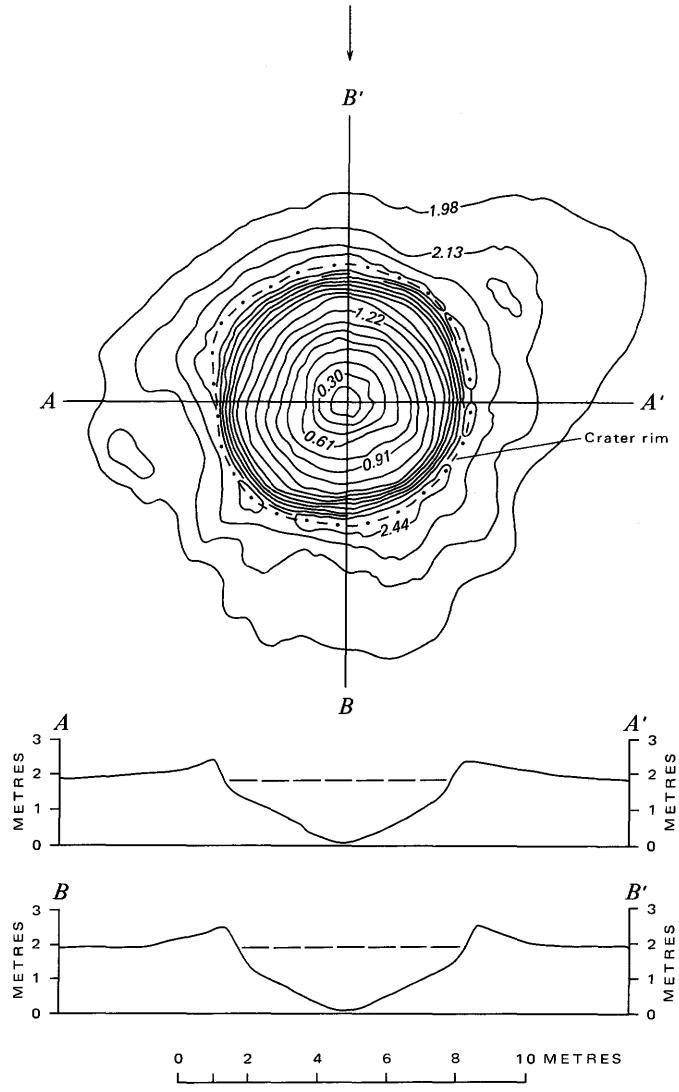

FIGURE 4.—Contour map and profiles illustrating complete rim around large crater in gypsum lake beds produced by a missile impact. Bilateral symmetry is less well developed than in smaller craters. Contour interval 0.1525 m (½ ft). Arrow indicates trace of missile. The profile *B–B'* is in the plane of the trajectory and *A–A'* is perpendicular to the plane of the trajectory. Dot-dash line on map represents crater rim; dashed lines in profiles show original ground surface. Note difference between this crater and the small crater in figure 3. (E_p=23.2×10^{14} ergs, Θ=46.2°. Crater 50.)

and lateral directions and absent beneath the trajectory. It is composed of particles ranging in size from powder to sizeable fragments (fig. 8) that in some materials may be as large as ¾ m. Most of the ejecta is disaggregated and fragmented target material, but as much as 20 to 30 percent may be sheared and compressed fragments of target material. Pieces of projectile are found in this unit. At most places, where the target material is layered, the sequence of the original layering is preserved in the ejecta but inverted (figs. 9 and 10).

Thin to discontinuous ejecta (fig. 11) surrounds the thick ejecta and may extend a small distance in the up-trajectory directions. Fragments in this unit are generally smaller than those in the thick ejecta but consist of the same three types of material. Fragments are scattered to distances near 12 to 16 m at right angles to the plane of the trajectory and 20 m or so in the forward direction when the crater diameter is near 5 to 6 m across. At some craters small tongues of this unit extend short distances up-trajectory.

Scattered ejecta (fig. 12) is gradational with thin to discontinuous ejecta, between it and the limit of throwout beyond which no fragments are found. In this unit, isolated fragments are found widely separated from one another. Where the uppermost surface of the target is nearly cohesionless, the fragments produce secondary impact craters; where the uppermost surface is cohesive, only scattered fragments and debris are found. The limit of throwout from most craters is about 130 m; from some, it may be as far as 330 m. Boundaries of the limit of throwout have the same type of symmetry as other ejecta units and extend chiefly in the down-trajectory direction (fig. 13). For some craters, scattered ejecta composed mainly of projectile fragments is found up-trajectory.

FIGURE 5.—Crater in sand produced by missile impact. Note small rim to upper left, up-trajectory side of crater. Crater is about 2.7 m across. Metal object (shown by arrow) is piece of missile. (E_p=6.63×10^{19} ergs, Θ=51.0°. Crater 13.) Photograph courtesy of U.S. Army.

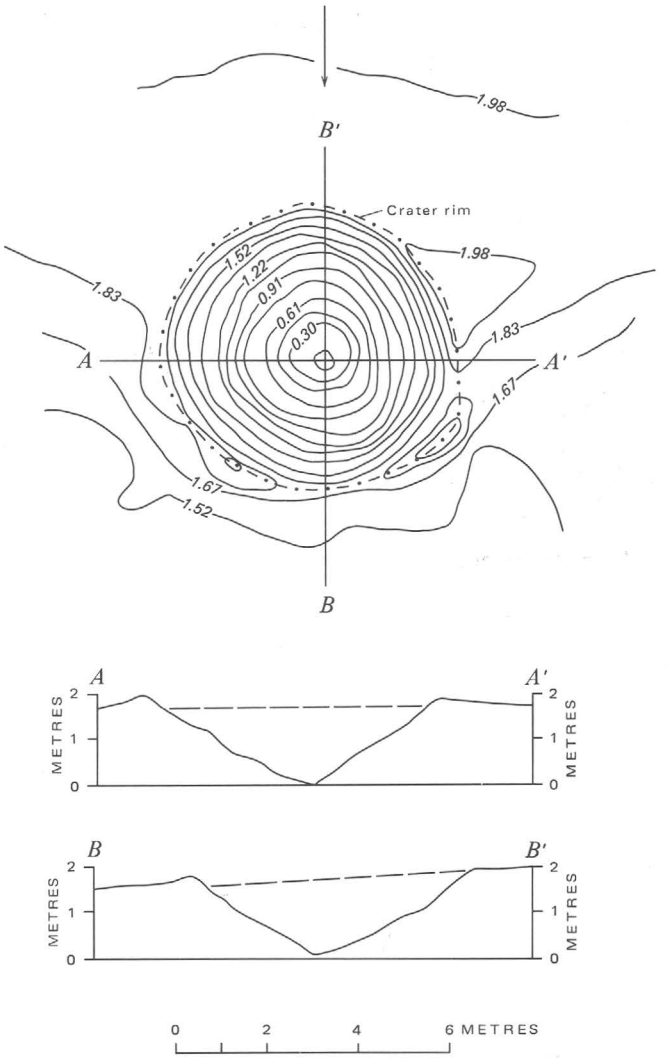

FIGURE 6.—Contour map and profiles of crater in colluvium illustrating conical shape of craters in weakly cohesive targets. Crater produced by missile impact. Contour interval 0.1525 m (½ ft). Arrow indicates trace of missile. Profile *B–B'* is in the plane of the trajectory; *A–A'* is perpendicular to the plane of the trajectory. Dot-dash line on map represents crater rim; dashed lines in profiles show original ground surface. Note difference in profiles for this crater and those in figures 2 and 4. (E_p=31.4×10^{14} ergs, Θ=45.0°. Crater 16.)

Undeformed target material is undeformed material surrounding the crater and underlying part of the ejecta. The distribution and character of other units depend

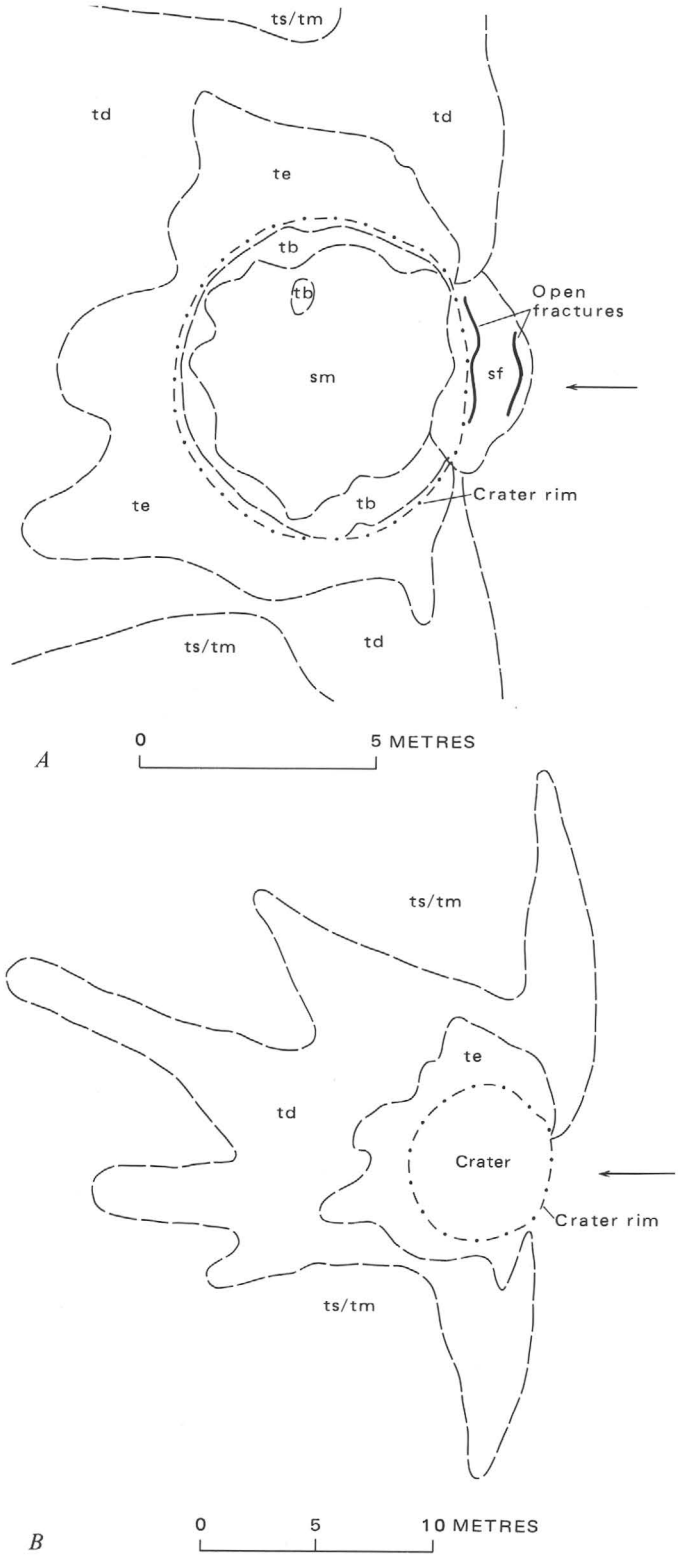

FIGURE 7.—Crater produced in fixed gypsum dune by missile impact: tm, target material; te, thick ejecta; td, thin to discontinuous ejecta; ts, scattered ejecta; tb, tilted and broken target material; sf, shattered and fractured target material; and sm, slope material. *A*, Detail near crater; *B*, Distribution of thin to discontinuous ejecta and thick ejecta around crater. Arrow indicates trace of missile. (E_p=24.1×10^{14} ergs, Θ=45.7°. Crater 18.)

FIGURE 8.—Thick ejecta from crater produced in dry sandy alluvium by missile impact. Note ejecta range in size from fine debris to fragments 10 or more cm across. Arrow "p" points to projectile fragment, "c," sheared and compressed target material partly coated with powdered projectile, "f," relatively undeformed target material. (E_p=20.4×10^{14} ergs, Θ=46.4°. Crater 31.) Photograph courtesy of U.S. Army.

on the characteristics of the target material summarized in the introduction. Cohesion and water content of the target material are critical. In the typical case, the target material was dry to moist, weakly cohesive silts and sands.

Tilted and broken target material underlies the thick ejecta below the rim and beneath the flanks (fig. 9). Here target material is warped upward and fractured. Rotation and upward warping rapidly decrease outward from the rim crest. Generally, upward warping of the target material is absent on the up-trajectory side. Tilted and broken target material is generally exposed

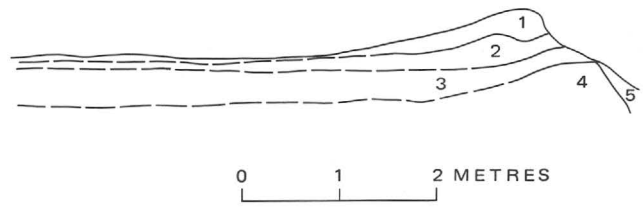

1. Ejecta, lower horizon
2. Ejecta, upper horizon
3. Tilted upper horizon
4. Tilted lower horizon
5. Slope material

FIGURE 9.—Profile through down-trajectory flank of crater in alluvium produced by missile impact showing inverted stratigraphy. Note lower horizon unit of ejecta (1) overlies upper horizon unit of ejecta although it was originally stratigraphically lower. Original ground surface was tilted upward and broken near crater. (E_p=13.8×10^{14} ergs, Θ=46.4°. Crater 6.)

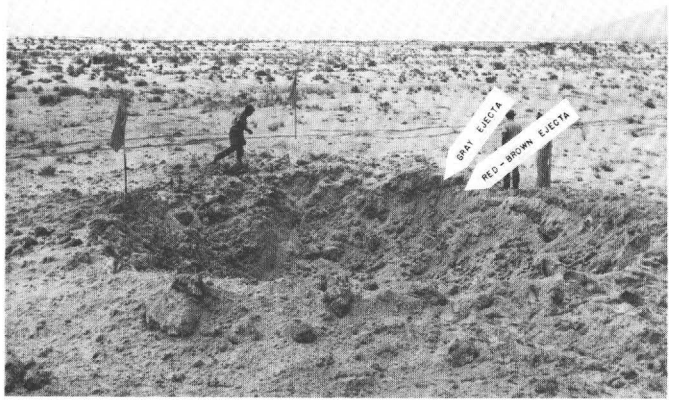

FIGURE 10.—Target materials in inverted sequence exposed in upper crater wall of crater in water-saturated gypsum lake beds. Darker gray ejecta overlies lighter red-brown ejecta; red-brown unit overlies gray unit in undisturbed target material. (E_p=15.7×10^{14} ergs, Θ=45.9°. Crater 7.) Photograph courtesy of U.S. Army.

along the upper crater walls in the lateral- and down-trajectory directions and, rarely, on the flanks.

Shattered and fractured target material (fig. 14) is exposed on the steep crater wall and edge beneath the trajectory. Open fractures concentric to the crater edge and even downward faulting occur near the crater edge. This unit may include material with closely spaced conjugate fractures showing sheared surfaces and coatings of powdered projectile.

Slope material is composed of cohesionless debris at or below the angle of repose within the crater and debris on the crater floor. Some of this material is the result of fallback of ejecta, some the result of slumping. Pieces of

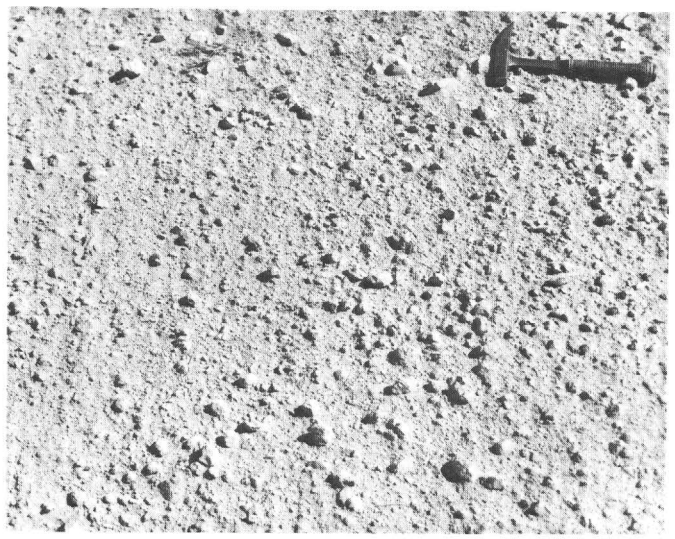

FIGURE 11.—Thin to discontinuous ejecta around crater in silty alluvium produced by missile impact. Pick is 30.5 cm long. Note finer ejecta between fragments. (E_p=24.1×10^{14} ergs, Θ=45.7°. Crater 15. Photograph courtesy of U.S. Army.

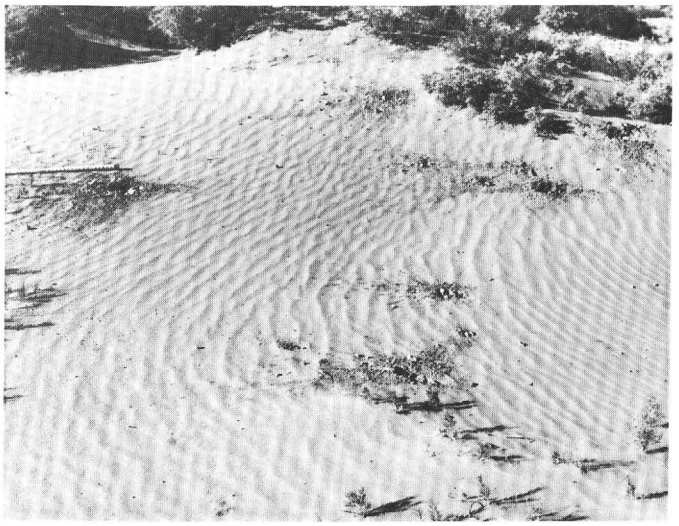

FIGURE 12.—Scattered ejecta from crater in clayey silt and silty clay. Ejected fragments have produced secondary impact craters in moist ripple-marked sand. (Crater 20.) Photograph courtesy of U.S. Army.

broken target material, sheared and compressed material, and the projectile are found in this unit. Slope material is best developed on lower parts of crater walls, especially down-trajectory, and lateral walls.

DISTRIBUTION

Variations in the distribution and character of the map units described are a function of target material and crater size. When the target material is alluvium,

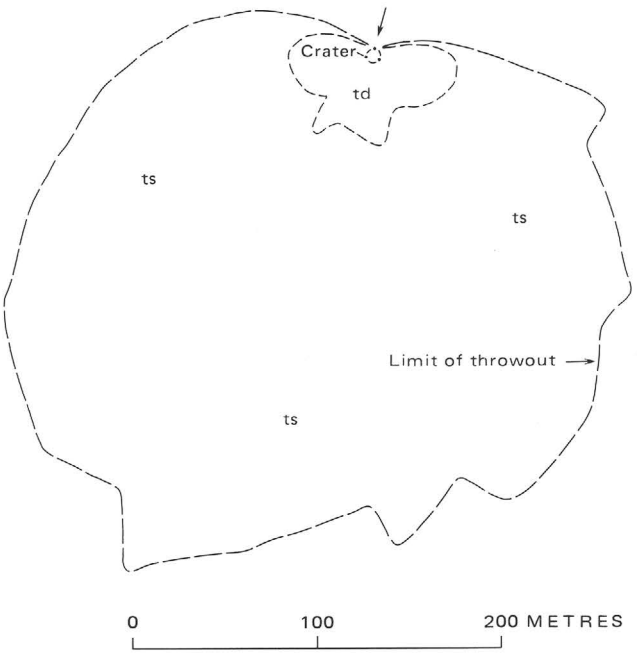

FIGURE 13.—Map illustrating limit of throwout and scattered ejecta, extending 330 m from crater produced in clayey silt by missile impact. Arrow indicates trace of missile. (E_p=25.2×10^{14} ergs, Θ=25.8°. Crater 20.)

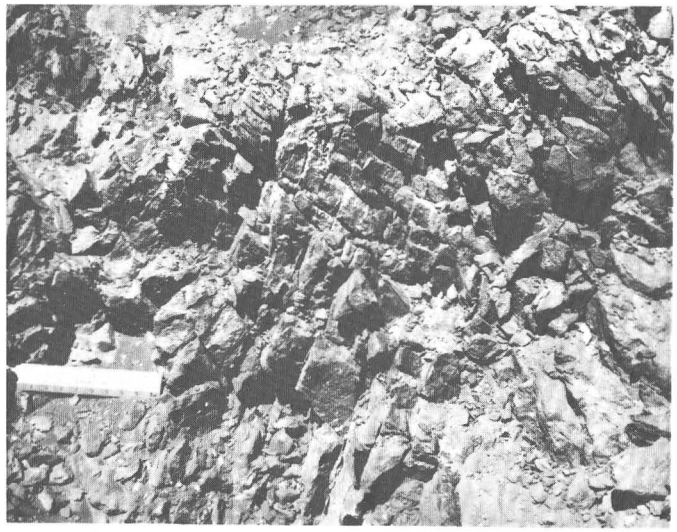

FIGURE 14.—Shattered and fractured target material exposed on up-trajectory wall of crater in dry silty sand. Note conjugate fractures producing diamond-shaped pattern; some of the fractures are coated with projectile material. Tensile fractures mainly parallel to plane of photograph, formed later and do not have coatings. Scale is about 16 cm long. (E_p=69.9×10^{14} ergs, Θ=40.6°. Crater 53.) Photograph courtesy of U.S. Army.

colluvium, fixed gypsum dunes, and rock, thick ejecta is absent in the up-trajectory direction. Aprons of thick ejecta on the down-trajectory side of the crater (fig. 15*A*) are common and many craters have concentrations of ejecta that form lobes in lateral directions (fig. 15*B*). In some cases, more debris is found in lateral directions than in the down-trajectory direction (fig. 15*C*). Around some craters, isolated islands of thick ejecta are found beyond a main layer of thick ejecta. Thick ejecta completely surrounds craters in water-saturated gypsum lake beds and large craters in moist gypsum lake beds. At these craters, such ejecta is thicker and extends farther in the lateral and down-trajectory directions than in the up-trajectory direction, with one exception. At crater number 44, in a water-saturated lake bed, thick ejecta actually extended farther up-trajectory than down-trajectory and laterally. Craters in weakly cohesive sand are characterized by small amounts of thick ejecta in the up-trajectory direction (fig. 5).

For layered targets, materials ejected from both upper and lower layers retain some discernible layer

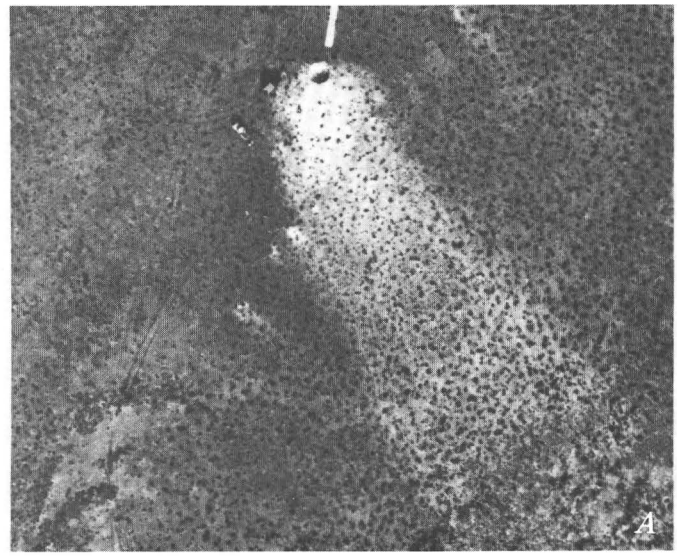

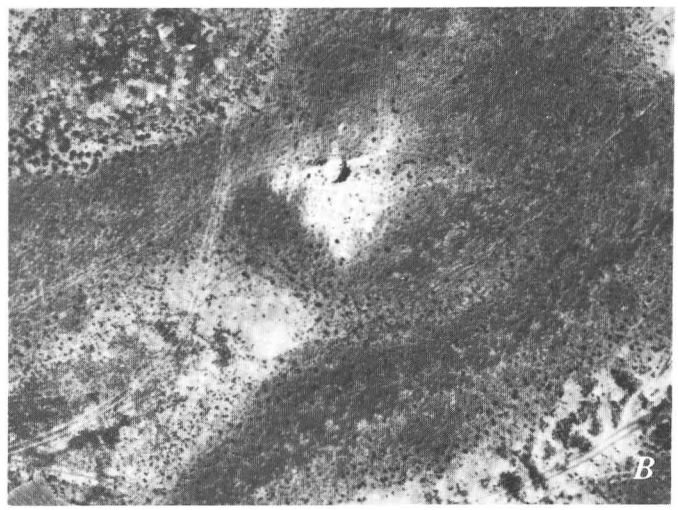

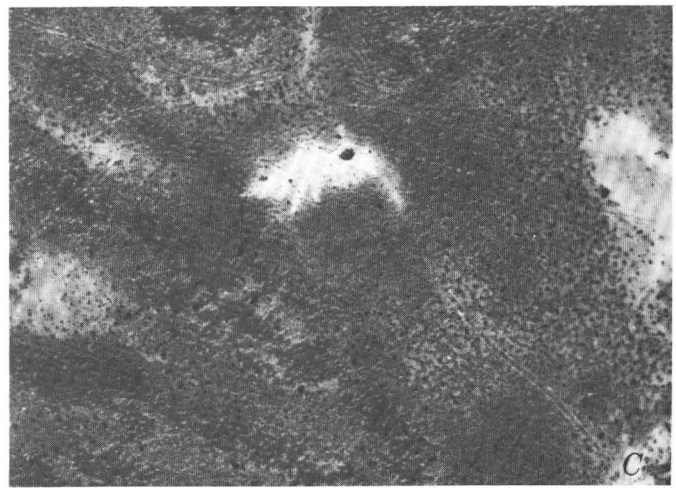

FIGURE 15.—Variations in ejecta distribution around craters in fixed gypsum dunes. *A*, Apron of very light ejecta parallel to trajectory plane on down-trajectory side. Diffuse light material alined 45° to trajectory trace is windblown ejecta. White panel on up-trajectory side is 15.2 m long and parallel to trace of missile (Crater 37). *B*, Bilateral symmetry of ejecta with radial extensions of ejecta in lateral and down-trajectory directions (Crater 18, see also fig. 7). Trace of missile is from top of photograph to crater. *C*, Ejecta developed chiefly in lateral directions without bilateral symmetry. Trace of missile is from top of photograph to crater. Note maximum extent of ejecta is in lateral directions and more extensive to left than to right (Crater 30). Photograph taken by NASA Remote Sensing Aircraft.

coherence in their distribution; ejecta falls in a bilaterally symmetrical pattern, and original stratigraphic relations are inverted. This is shown by a crater in a layered target of gypsiferous lake beds overlain by alluvium (fig. 16*A*). Material from the lower white gypsum layer is concentrated in the down-trajectory direction where it overlies the darker ejecta from the upper layers. In lateral directions little or no white gypsum is found superposed on the darker alluvium from the upper layers. A similar effect can be seen at a crater in silty sand and sandy silt, where dark-reddish materials from the upper layers are found on the up-trajectory side of the crater and materials from the lower reddish-gray layers are found in down-trajectory and lateral directions. When the gypsum layer is deep relative to the crater diameter, isolated patches of white gypsum are found near the crater rim and superposed on ejected alluvium from the upper layers (fig. 16*B*).

Variations in distribution patterns of thin to discontinuous ejecta are similar to those in thick ejecta but differ in these respects: the distribution of thin to discontinuous ejecta may be greatly affected by the wind; deposition of debris is more common in the up-trajectory direction; and the outer boundary of the thin-ejecta units tends to be more irregular, with fingerlike extensions. Craters in dry to moist targets of alluvium, colluvium, fixed gypsum dunes, and rock have the least amount of thin to discontinuous ejecta up-trajectory; craters in water-saturated gypsum lake beds and large craters in moist gypsum lake beds have somewhat larger amounts of debris up-trajectory.

Scattered ejecta and the limit of throwout are controlled by target material, static atmosphere, and wind. The static atmosphere decelerates fine-grained ejected debris more than coarse ejected debris; the grain size of ejecta depends on the cohesion of the target material. Deceleration by the atmosphere may be illustrated by comparing craters in fixed gypsum dunes, where fragments in the scattered ejecta are centimetre size and less, with craters in clayey silt, where scattered ejecta fragments are 15 cm and less. For gypsum, the limit of throwout is near 100 m or so, and for clayey silt, near 330 m. Wind can greatly affect the scatter of ejecta. When the craters shown in figures 15*B* and 15*C* were formed, there was little or no wind, but, at the crater of 15*A*, the wind distributed the ejecta along a path about 45° to the trace of the missile. For craters in clayey silt with coarse ejecta, the limit of throwout and scattered ejecta may be skewed in the direction of the wind.

SECONDARY IMPACTS

Cratering by impact of ejected debris produced by missile impact is a function of the mechanical properties

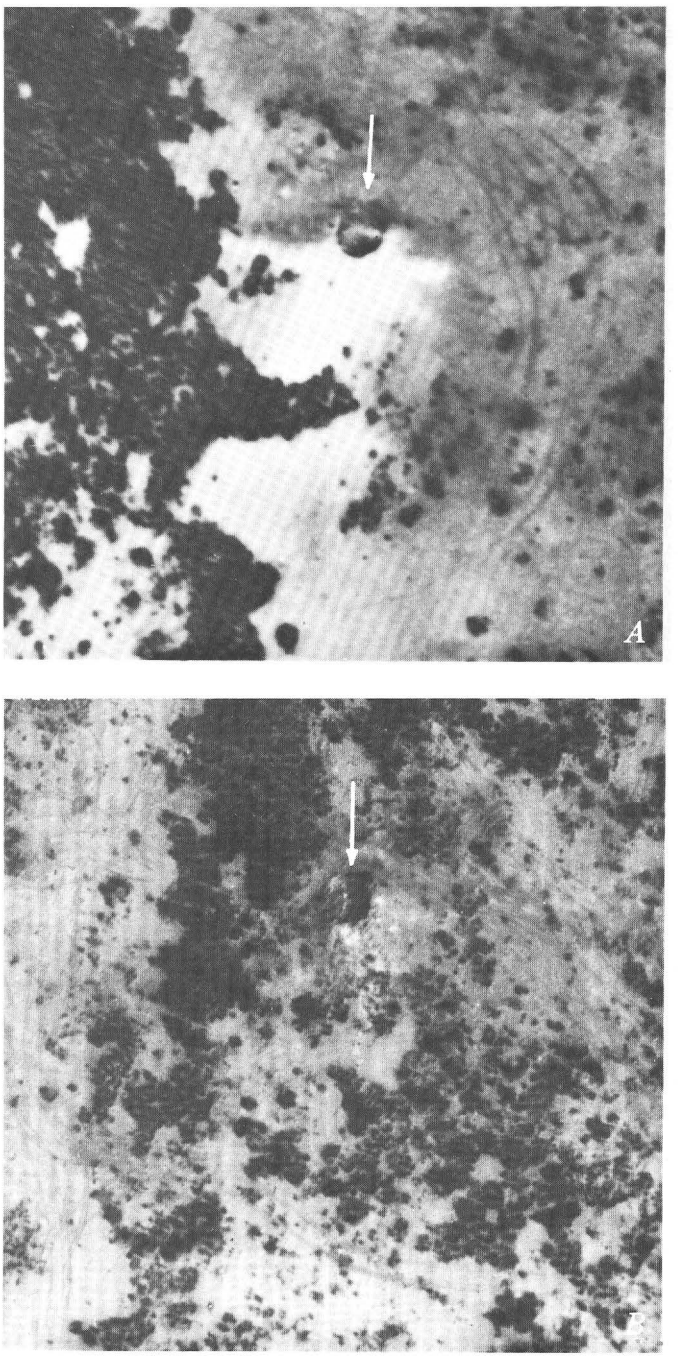

FIGURE 16.—Ejecta from craters in layered targets. Arrows indicate craters and traces of missiles. *A*, Crater in gypsum overlain by 0.6 m of alluvium. Light ejecta from lower layer superposed on darker ejecta from upper layers with bilateral symmetry. Ejecta from lower gypsum layer is displaced down-trajectory with respect to ejecta from overlying darker alluvium. Original gypsum layer can be seen in crater (Crater 36, about 5 m across). *B*, Crater in gypsum overlain by 1.0 m of alluvium. Scattered light ejecta of gypsum from lower layer superposed on darker ejecta from lower layer. Gypsum ejecta is spotty because of greater thickness of overlying alluvium (Crater 35, about 5 m across). Photograph taken by NASA Remote Sensing Aircraft.

of the near-surface materials, the character of the ejecta, and distance from the crater. A great number of secondary impact craters are produced by ejected debris where surface materials, such as sand, have low cohesion. Where near-surface materials are strong and more cohesive, no secondary impact craters are produced; rather, the surface is littered with scattered fragments and blocks, and piles of fine debris. Large secondary impact craters are produced when fragmentation of the target results in large blocks and clods. Where ejected debris is fine, as from craters in weakly cohesive sand, small secondary craters are produced. Secondary impact craters tend to be larger relative to the size of the ejected fragment at greater distances from the crater because the velocities, and therefore specific energies, are greater.

Where secondary craters are produced by debris ejected from craters produced by oblique impacts, their distribution is bilaterally symmetrical about the plane of the trajectory, and each secondary crater may be bilaterally symmetrical about the plane of the oblique trajectory of the ejected fragment that produced it.

Well-developed secondary impact phenomena were studied at a crater (Crater 7) produced in water-saturated gypsum lake beds where ejecta characteristics and surface properties were favorable. The surface layering, from the top down, is 9–12 cm of cohesionless gypsum sand, 40 cm of very pale red-brown, moist, cohesive gypsum and gray cohesive water-saturated gypsum lake beds of unknown thickness. The impact (fig. 10) ejected large and small fragments from the cohesive gypsum layers. These fragments impacted the ejecta from the crater as well as the surrounding cohesionless gypsum sand at the surface. Mapping revealed the presence of map units common to other missile impact craters (fig. 17). Thick ejecta and thin to discontinuous ejecta mapped completely around the rim and both were bilaterally symmetrical across the plane of the trajectory. Secondary impact craters were found throughout these units but were most abundant in the region of the scattered ejecta where their distribution was bilaterally symmetrical. The greatest number were found in down-trajectory and lateral directions. Locally, the secondary craters formed arcuate patterns, clusters, and linear arrays radial to the crater. Relative sizes of secondary craters and the fragments that produced them varied systematically, but not regularly, with distance from the crater. Near the crater rim, in thick ejecta, essentially undeformed ejected fragments were larger than the craters they occupied (see blocks on crater rim in fig. 10). Others, farther out, were the same size as the crater they produced and deformed so they filled the secondary crater (fig. 18). Many of the fragments were smaller than the crater, deformed, and lined the crater they produced (fig. 19); others were less deformed (fig. 20). Fragments producing the secondary craters are partially (fig. 21) to completely ejected.

Commonly, each secondary crater shows bilateral symmetry across the plane of the trajectory of the secondary fragment, as at the crater of figure 22, where cohesive fragments impacted ripple-marked sand. Like the parent missile impact crater the secondary produced little or no ejecta up-trajectory; ejecta from it is found in lateral and down-trajectory directions. As this crater was produced in moist sand, the ejecta is composed of lumps scattered along radials from the crater. At the crater shown in figure 21, produced in dry gypsum sand, the ejecta forms a smooth light-gray apron on the down-trajectory side. Not all secondaries produced show such perfect symmetry. At some, the rotational energy of ejected fragments has caused a variety of results, including chains of pits where the fragment rolled and bounced, and ejected debris that is nonradial to the primary crater.

Fine ejecta from craters may produce many small craters (fig. 23) with a wide range of sizes. A multitude of secondary craters produced in sand by ejecta from a crater in sand may all be nearly the same size and cover the surface, resembling raindrop impressions. When the surface is hard, no secondaries are produced. Rather, piles of debris (fig. 24) and scattered fragments litter the surface.

DEFORMATION

Degree of deformation of both the missile and target varies mainly with the velocity of the missile at impact. Other variables affecting deformation of the missile and target are density of the missile and its components, design and strength of the missile and its components, size of the missile, and shape and orientation and trajectory at impact. At the highest velocities, destruction of the missile is so complete that it is difficult, if not impossible, to find pieces of it anywhere. At lower velocities, large warped and bent sections of the missile are scattered in the ejecta or buried along with fragments, wires, nuts, and bolts. Target properties such as density, cohesion, angle of internal friction, grain size, porosity, and pore fluids affect deformation mainly of the target. As response of the target depends on target material as well as missile velocity, deformations for craters differ in rock, alluvium, water-saturated lake beds, and sand. For the typical case, the deformation observed in the target material is of many kinds: compression, shearing, mixing of missile and target pieces, injections, banding, fracturing, and folding result from the shock and stress waves generated by the impact. A typical generalized case is described below.

Evidence for the wide range of types of deformation is found in ejecta from craters in moderately cohesive,

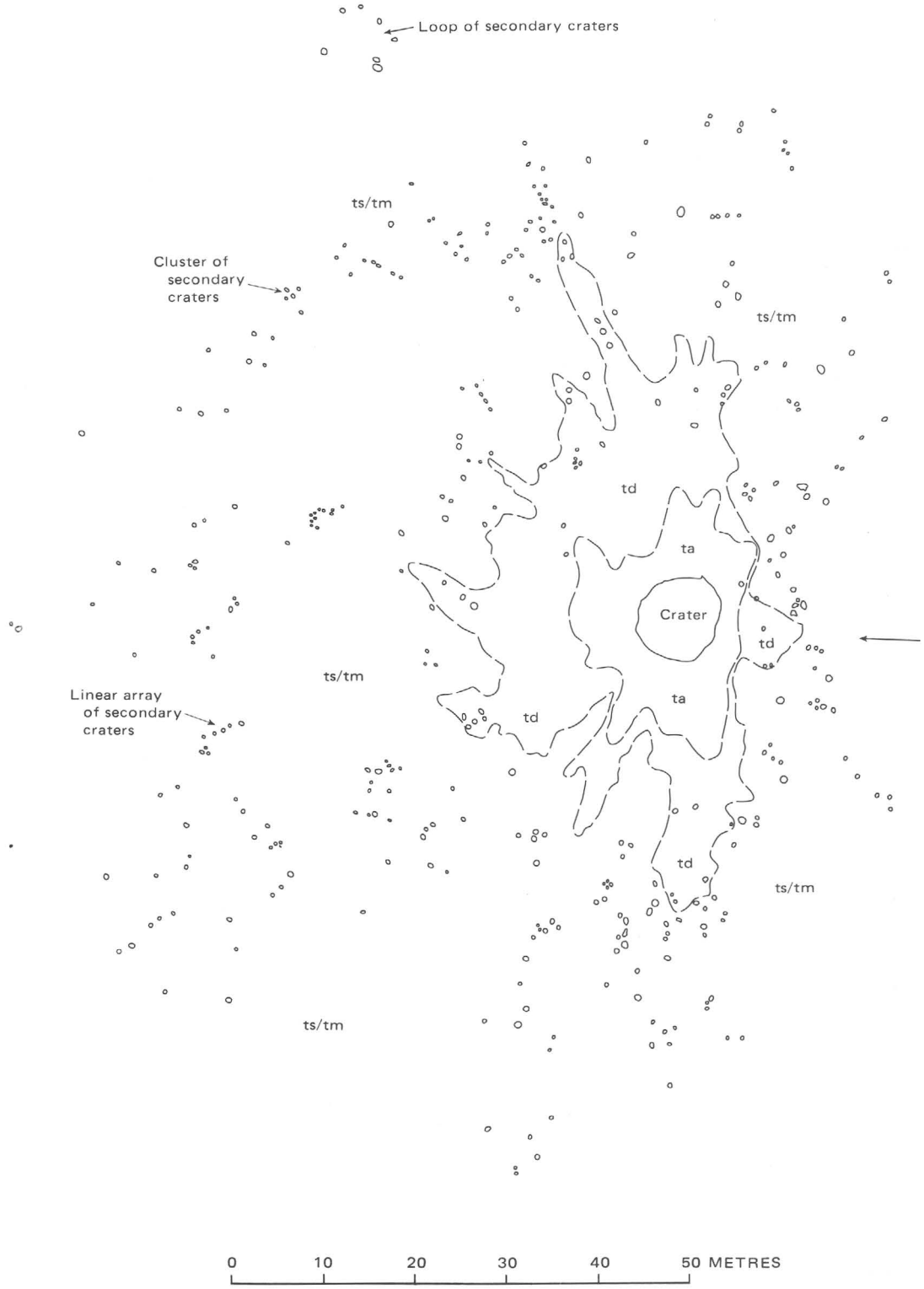

FIGURE 17.—Map of crater in water-saturated gypsum lake bed showing distribution of secondary impacts, thin to discontinuous ejecta, and thick ejecta. Crater rim shown by solid line; te—thick ejecta, td—thin to discontinuous ejecta, ts/tm— scattered ejecta on target material, small open circles—secondary impacts. Note concentration of secondary impacts in down-trajectory and lateral directions. Secondaries form linear arrays, local loops, and clusters. Arrow indicates trace of missile. (Crater 7; see also fig. 10.)

porous (density $\approx$ 1.6g/cm^3), dry to moist target materials where densities of some ejected fragments may equal or exceed the density of the target material, and small partly fused pieces of missile are scattered in

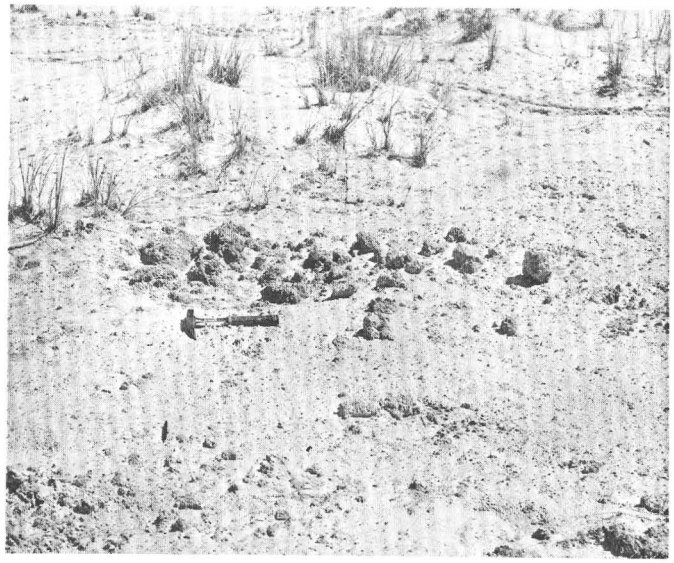

FIGURE 18.—Secondary crater filled by ejecta that produced it. Deformed fragment in crater is from lower gray layer. Pick is 30.5 cm long. (Ejecta from Crater 7.) Photograph courtesy of U.S. Army.

the ejecta along with contorted missile pieces. Some larger fragments of missile that failed by shearing are found. Shocked and deformed target materials are represented by sheared and compressed target material with dark-gray coatings of the fused and powdered missile (fig. 25*A*,*B*). Some sheared and compressed fragments have been compressed to densities as great as

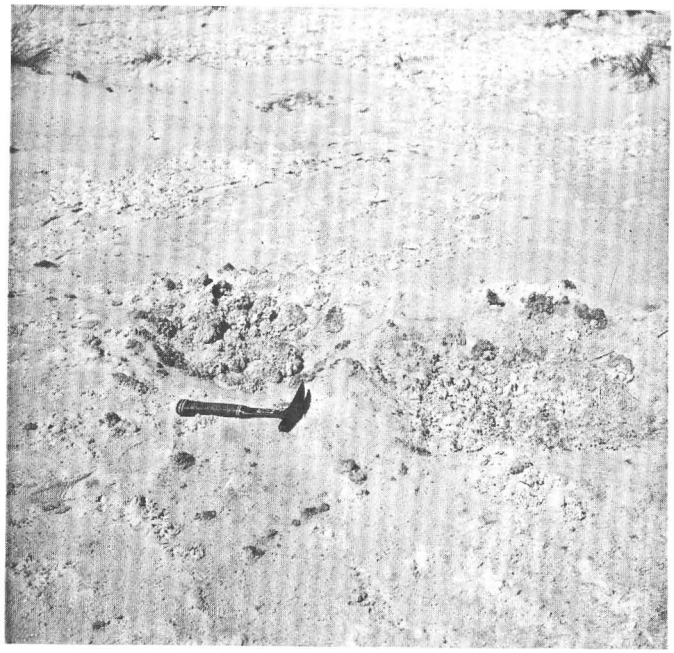

FIGURE 19.—Secondary impacts beyond thin to discontinuous ejecta. Secondary craters are larger than fragments that produced them. Secondary projectiles from dark-gray layer of wet gypsum have deformed floors of secondary craters and line them. Pick is 30.5 cm long. (Ejecta from Crater 7.) Photograph courtesy of U.S. Army.

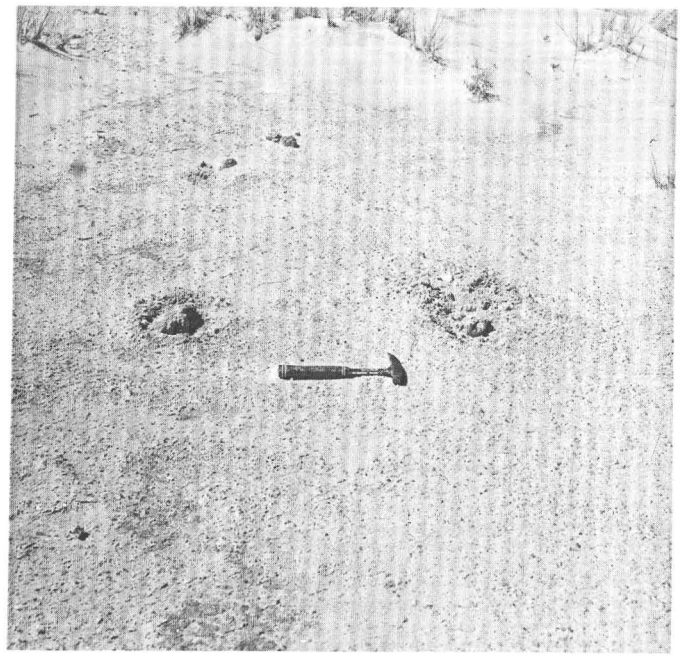

FIGURE 20.—Secondary craters produced by ejecta from red-brown layer in thin to discontinuous ejecta. Craters are larger than fragment that produced them. Fragment to left partly deformed, one to right deformed and broken. Pick is 30.5 cm long. (Ejecta from Crater 7.) Photograph courtesy of U.S. Army.

2.2 g/cm^3 and their surfaces are grooved and striated. Dark coatings of powdered and partly fused missile partly cover the grooved surfaces of many of these compressed fragments and fractures within them may be filled with powdered projectile. Many of them compressed, then failed in tension, as indicated by open fractures with hackly surfaces normal to the striated surfaces (fig. 25*C*). These coated compressed fragments are found in all map units from the crater floor to the limit of throwout. More intensely shocked material may be present in very fine debris wafted away by gentle winds or lost by dilution in the large quantities of other ejecta and materials surrounding the crater.

Much of the target material and projectile is pulverized and fragmented to sizes of 70 cm across and less for the target and 10 cm across and less for the projectile. Densities of ejected fragments range from more dense to less dense than the original target material. Pulverized and disaggregated debris have densities equal to the grain density of the target material. Most of the ejecta is relatively undeformed and has about the same density as the target material. Large blocks and fragments of relatively undeformed target material are concentrated near the rim of the crater, in slope material, and in thick ejecta, but are found in other map units farther from the crater, where they tend to be smaller. Fragments of this type are bounded by irregular, hackly surfaces, joint surfaces, the original ground surface, and, when pres-

FIGURE 21.—Secondary crater produced by fragment from gray layer. Secondary fragment is broken into pieces, deformed, and ejected from crater. Ruler, about 16 cm long, is on up-trajectory side. Light rim of crater is ejecta from lower gypsum sand superposed on darker materials of surface. (Ejecta from Crater 7.) Photograph courtesy of U.S. Army.

ent, bedding planes. They may be rectangular to irregular in shape. Relatively undeformed fragments are products of late-stage ejection where normal stresses in the shock wave and subsequent stress waves have

FIGURE 22.—Secondary craters produced by ejecta in moist ripple-marked sand. Handle of pick points up-trajectory. Note concentration of ejecta in lateral and down-trajectory directions and virtual absence up-trajectory. Tertiary ejecta is lumpy because sand was moist. (Ejecta from Crater 20.) Photograph courtesy of U.S. Army.

FIGURE 23.—Secondary craters produced by fine ejecta impacting cohesionless gypsum sand. Ruler is approximately 16 cm long; pick is 30.5 cm long. Ejecta from crater is moist gypsum lake beds. Lake beds overlain by 9 cm of dry gypsum sand. (Ejecta from Crater 11.) Photograph courtesy of U.S. Army.

dropped to values near and less than ambient conditions. They have failed in tension, forming new fractures, separating along preexisting fractures, or separating along bedding planes.

Parts of the missile have failed in tension. Occasionally nuts, bolts, and other components are found, showing preexisting boundaries controlled the manner in which they failed. Some small pieces of relatively undeformed missile are broken and partly to completely separated along hackly irregular fracture surfaces, suggesting tensile failure.

Beneath the ejecta the original ground surface is tilted away from the crater on the lateral and down-trajectory flanks of the crater. At some craters, layers at and near the ground surface can be traced craterward to the rim, then outward, overturned and superposed on themselves. Most commonly, overturned and jumbled blocks from the near surface rest upon the original ground surface and bury it. The original surface on the up-trajectory flank is generally exposed. Here the surface is level or even displaced downward, and open concentric fractures and faults occur at right angles to the surface.

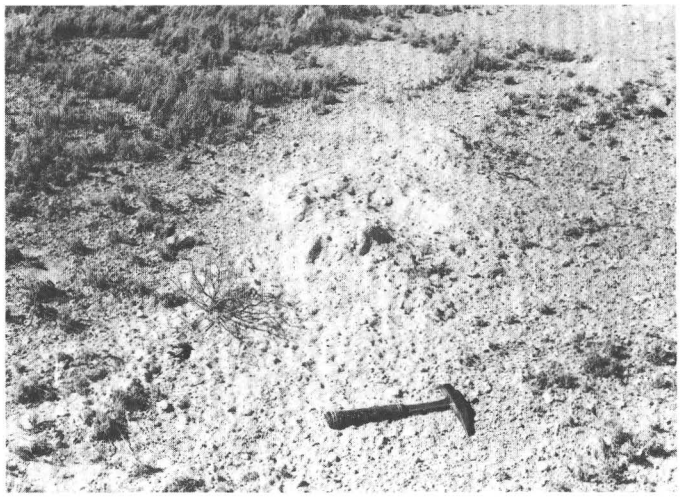

FIGURE 24.—Pile of debris and scattered fragments from crater in gypsiferous alluvium. Surface materials were so cohesive that no secondary craters formed. Pick is 30.5 cm long. (Ejecta from Crater 15.) Photograph courtesy of U.S. Army.

ZONES OF SUBSURFACE DEFORMATION

Studies of trenches through four craters indicate that the subsurface deformation can be classified into five zones (see for example, figs. 26 and 27): (1) mixed breccia, (2) sanded material, (3) a zone of conjugate fractures, (4) tilted and broken material, and (5) a zone of open fractures.

MIXED BRECCIA

Mixed breccia forms a lens composed of fragments of missile and compressed target material in a matrix of fine debris beneath the crater floor. The fragments are jumbled and no simple pattern can be seen. Surfaces of adjacent large fragments are rarely parallel. Fragments of both the compressed target material and missile are as large as 15 cm, but generally smaller. Many surfaces of the compressed target material are polished, striated, and grooved, showing that they have been sheared. Mixed breccia (fig. 28) is found below the center of the crater floor. Diameters of the mixed breccia bodies beneath the craters in alluvium with an underlayer of gypsum measure 1.2 to 1.5 m across where exposed; those in indurated gypsum dunes measure 2.1 to 2.3 m across. Boundaries of mixed breccia with adjacent units are gradational; a few distinct stringers of mixed breccia containing pieces of projectile penetrate the sanded material (fig. 29).

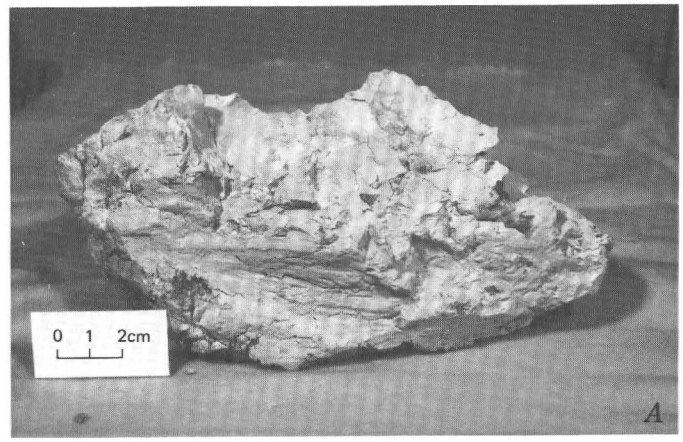

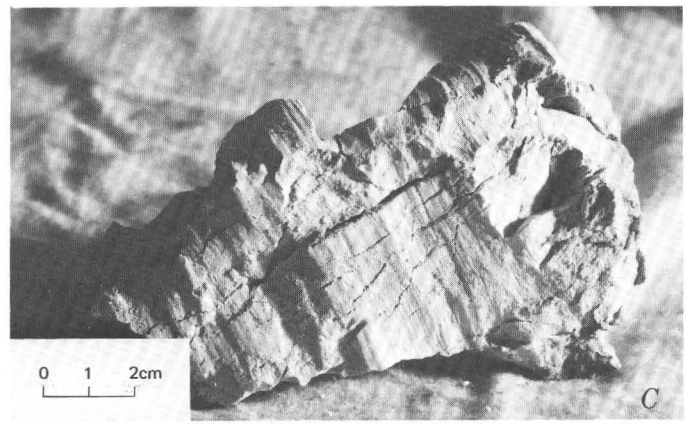

FIGURE 25.—Sheared and compressed target material and coated rocks. *A*, Sheared and compressed target material ejected from crater in colluvium. Note grooves and striations on lower surface of fragment (from Crater 16.) *B*, Coated fragment from crater in colluvium. Coating indicated by arrow is black and composed chiefly of powdered, fragmented, and fused projectile (from Crater 58.) Photography courtesy of U.S. Army. *C*, Sheared and compressed target material with grooves and striations on surfaces. Note open tension fractures transecting shear surfaces at right angles. Target was gypsiferous alluvium (from Crater 15.)

Evidence of displacement of materials of the mixed breccia is ample. Fragments of sheared and compressed materials identical with those of the mixed breccia are found in ejecta and slope material along with pieces of the missile. Although the sheared and compressed target material is found chiefly in the mixed breccia and thick ejecta, scattered small fragments are found up-trajectory and in the thin to discontinuous ejecta.

SANDED MATERIAL

Sanded material (fig. 30) is well developed only in craters in indurated gypsum. It is composed of disaggregated gypsum and small lumps of material that can be easily broken by finger pressure. No evidence of compression is found in the sanded zone and pieces of missile found appear to be cataclastic injections. Banding is developed in the sanded material near the contact with the mixed breccia, where bands are subparallel to the contact. Toward the zone of conjugate fractures, the banding is less distinct and the frequency of small lumps increases laterally. This unit, where exposed, surrounds the mixed breccia on all but the up-trajectory side; its symmetry is bilateral across the plane of the trajectory.

As the sanded material is banded subparallel to the adjacent contacts and has the same sense of symmetry as the ejecta, it represents fabric resulting from the flow of debris near the final stage of the ejection process.

ZONE OF CONJUGATE FRACTURES

The zone of conjugate fractures (fig. 31) is characterized by a crisscross fracture pattern. This pattern is closely spaced near the sanded zone, where fracture frequencies are about 0.8 to 1.2 per linear centimetre; frequencies decrease outward to about 0.3 per linear centimetre and less, at the boundary of the unit. Near the contact with sanded material, acute angles between fractures appear to be larger (near 70° to 60°) than those (near 60° to 50°) about a metre from the boundary. Although the two fracture sets normally show no relative displacement, they are locally offset a fraction of a centimetre or so along one fracture plane or the other. Such offsets, which suggest a shearing motion, are most frequent near the sanded zone boundary. The whole fracture pattern is flexed upward below the crater rim, where individual fracture planes can be followed along their curving traces.

Exposures of the zone of conjugate fracturing encircle the mixed breccia and sanded material. For craters in indurated gypsum dunes, such fracture zones are about 6.1 m across. For one of the craters produced in alluvium, it is about 4.6 m across, for the fourth crater we trenched it is poorly defined.

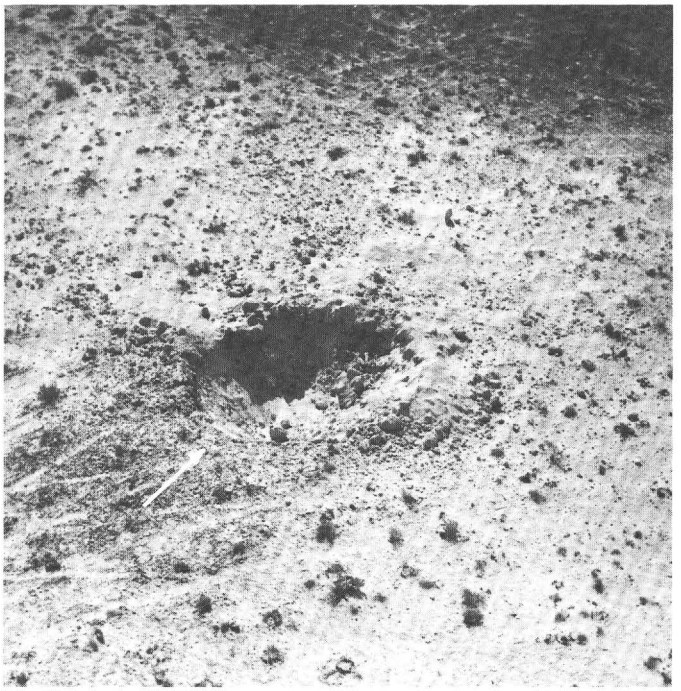

FIGURE 26.—Crater in indurated gypsum dunes produced by missile impact. Cross section shown in figure 27. Arrow indicates trace of missile. Note absence of ejecta on up-trajectory side, bilateral symmetry of ejecta, and large blocks of undeformed target material up to 0.46 m across. ($E_p = 16.0 \times 10^{15}$ ergs, $\Theta = 47.0°$ degrees, Crater 40, rim diameter about 5.6 m.) Photograph courtesy of U.S. Army.

TILTED AND BROKEN MATERIAL

In the tilted and broken material (fig. 32), widely spaced open fractures, some parallel to the ground surface and some perpendicular to it, form large blocks. The blocks, which are formed by tensile failure, are devoid of internal conjugate fractures and are themselves undeformed. Blocks of tilted and broken material, unlike lumps and pieces from the sanded material and zone of conjugate fractures, can be broken only with difficulty. Beneath the crater rim, the blocks and their bounding fractures have been rotated upward. In some, bands and layers can be traced from the tilted and broken zone as a continuous fold that overturns and continues in the ejecta.

The lateral extent of tilted and broken material is difficult to establish visually, but studies of similar craters in identical materials, using an engineering seismograph with a 3.05-m geophone-source spacing, indicate a significant change in acoustic velocities of indurated gypsum at distances between 5.5 and 8.9 m from the crater center for radials perpendicular to the trajectory planes; for radials down-trajectory within a metre of the crater rim, acoustic velocities have decreased to less than a third or a fourth of that of the undisturbed gypsum (fig. 33). Significant disruption of the materials to distances of nearly 3 to 4 crater radii is

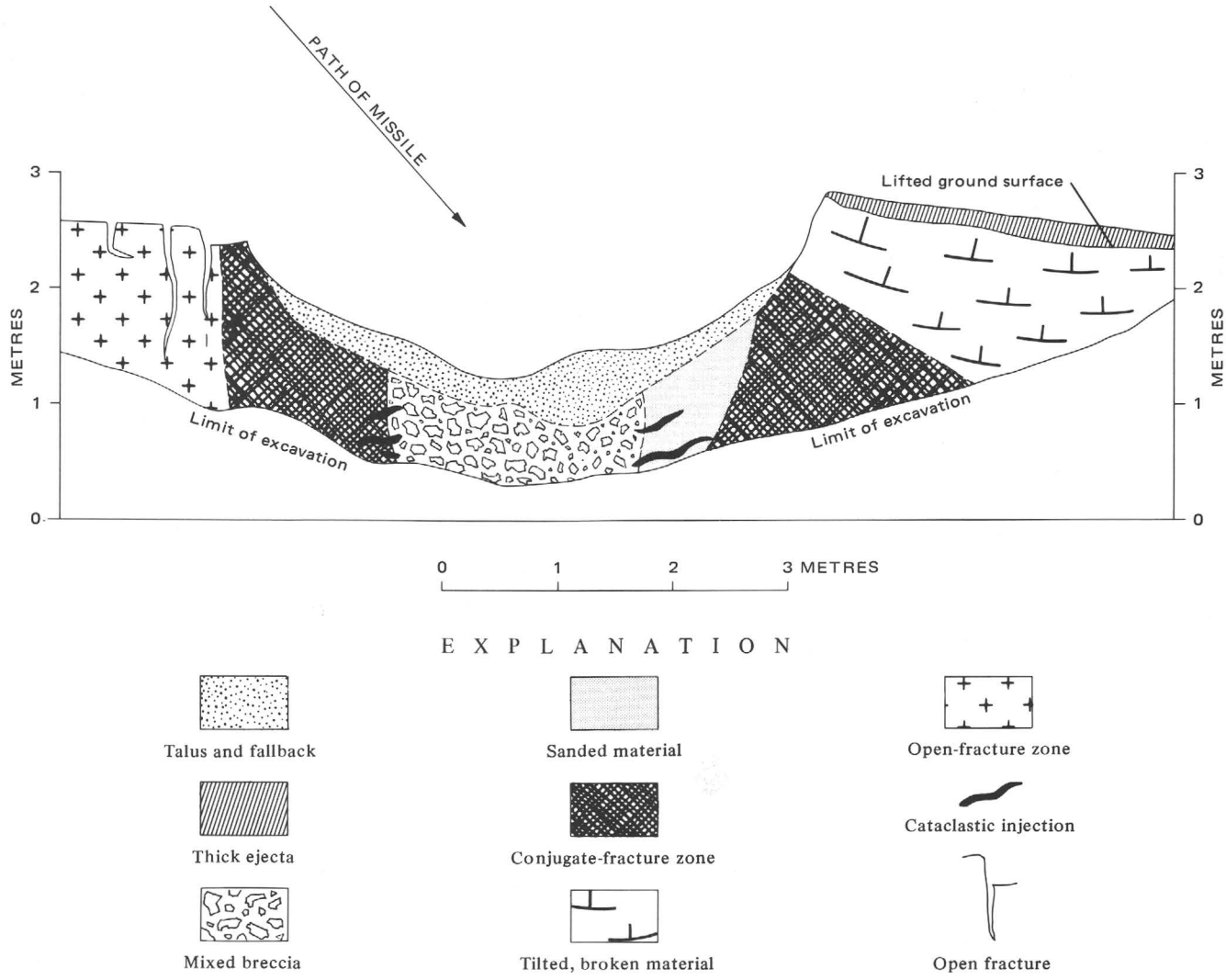

FIGURE 27.—Cross section of Crater 40 parallel to plane of trajectory showing subsurface deformation zones: mixed breccia, sanded material, zone of conjugate fractures, tilted and broken material, and zone of open fractures.

produced by the impact. No such clear change of acoustic velocity is found around the craters in alluvium, which had initially low acoustic velocities (Hans Ackerman, oral commun., 1969). It was possible to detect disruption of the material with other techniques. Strengths measured with a 3.8-cm-diameter shear vane were found to decrease toward the crater rim. Similar results were obtained with shear vanes and penetrometers around a crater in sandy silts and silty sands, shown in figure 34. Here again, little change is noted for craters in initially weak materials.

ZONE OF OPEN FRACTURES

The zone of open fractures (fig. 35) differs from tilted and broken material in that the original ground surface is often exposed and the original surface is level or displaced downward. Sparse, nearly vertical open fractures in the zone are concentric to the crater edge and confined to the up-trajectory side of the crater. Beneath the surface, shattered target material or conjugate fractures forming crisscross patterns are exposed on the up-trajectory crater wall (fig. 13). The conjugate fractures and tensile fractures perpendicular to them form diamond-shaped blocks with acute angles pointing upward and downward. Some of the conjugate fractures are grooved, striated, and coated with powdered projectile, whereas the tensile fractures are hackly and uncoated.

Layering provided a datum for tracing displacements of subsurface materials in the target material of two craters in silt (figs. 36, 16), Craters 35 and 36. In both craters, a layer of white gypsiferous silt was overlain by reddish-brown silty alluvium. The depth to the gypsiferous silt was 0.6 m (relatively shallow) for one (fig.

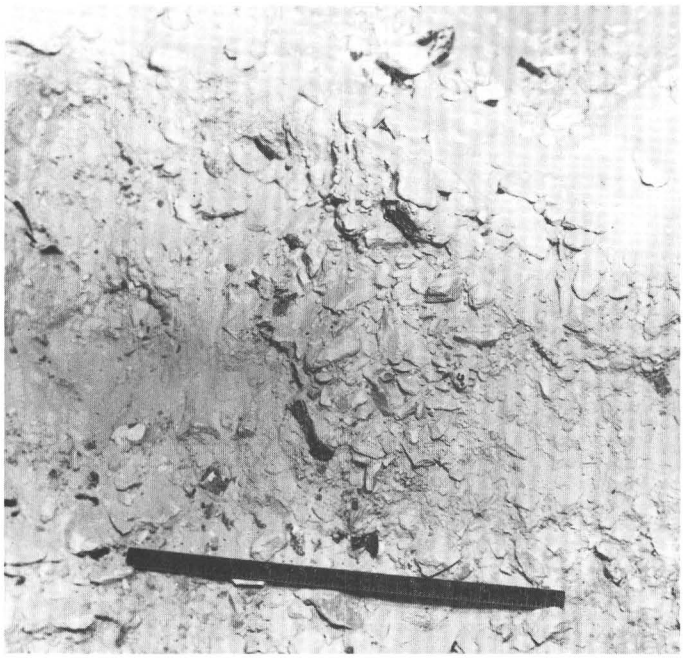

FIGURE 28.—Mixed breccia below crater floor. Dark fragments are pieces of missile. Note gray surfaces of some sheared and compressed gypsum, coated with thin layers of powdered missile. Rule is 0.305 m (12 in.) long. (Crater 40; see also fig. 26.) Photograph courtesy of U.S. Army.

36*A*,*B*), and about 1.0 m for the other (fig. 36*C*). For the first crater, the gypsiferous layer on the up-trajectory side was not displaced, and could be traced through a zone of intensive fracturing (zone of conjugate fractures) to the talus and fallback (fig. 36*A*). On the down-trajectory and lateral sides, the gypsiferous layer was folded and displaced upward (fig. 36*A*,*B*). A mixed breccia of gypsiferous silt and an intensely fractured zone were found beneath the crater floor. For the second

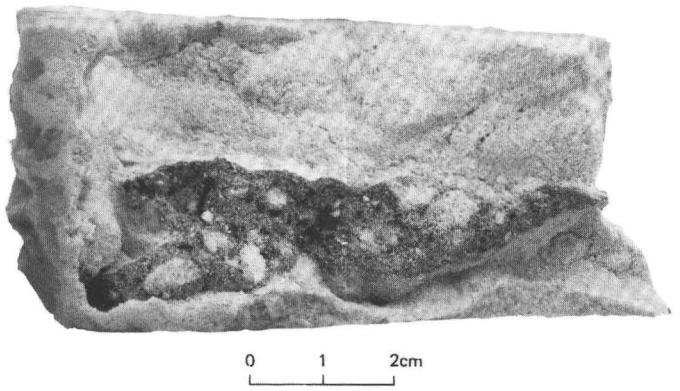

FIGURE 29.—Cataclastic injection of mixture of projectile and gypsum fragments into sanded zone. Injected unit is gray; sanded unit is white. Black fragments in injected unit are pieces of projectile; white fragments are gypsum; gray matrix is mixture of powdered projectile and sand-size grains of gypsum.

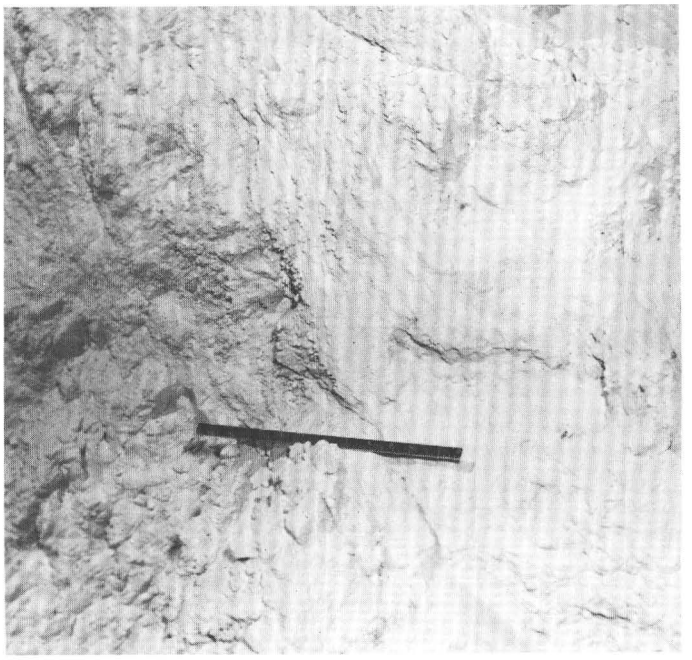

FIGURE 30.—Sanded material and banding. Conjugate fracture zone is toward left, mixed breccia and crater toward right. Rule is 0.305 m (12 in.) long. (Crater 40; see also fig. 26.) Photograph courtesy of U.S. Army.

crater, the deeper gypsiferous layer was displaced downward on the up-trajectory side and could be traced inward toward the center, where it was truncated. On the down-trajectory side, the gypsiferous layer, though

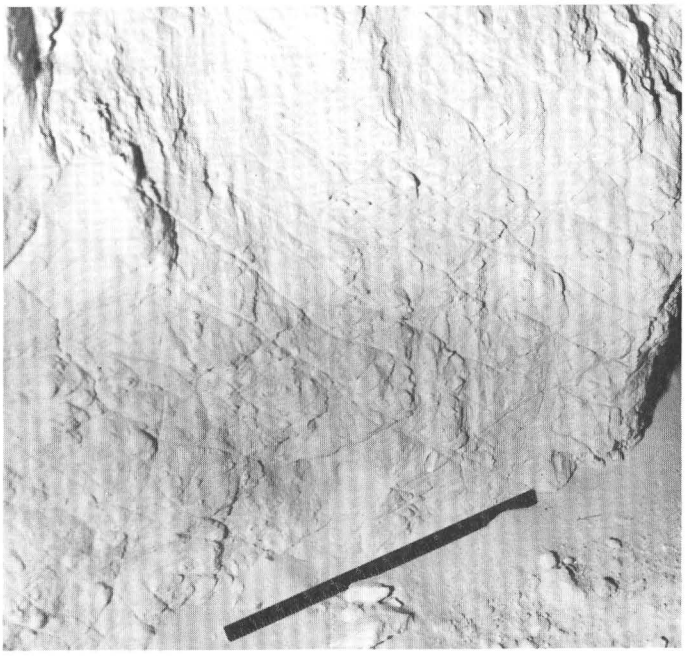

FIGURE 31.—Conjugate fractures. Sanded material (not shown) to left. Rule is 0.305 m(12 in.) long. (Crater 40; see also fig. 22.) Photograph courtesy of U.S. Army.

FIGURE 32.—Tilted and broken material exposed in upper wall of crater. One tilted and broken block indicated by arrow. Lower slope of crater wall is covered by talus (Crater 17). Photograph courtesy of U.S. Army.

brecciated, could be traced to the mixed breccia (fig. 36*C*). Here the mixed breccia, composed of sheared and compressed gypsum and pieces of missile, was displaced above the original horizon of the gypsiferous layer. Little or no gypsum was visible on the crater floor or walls prior to excavation, although some was present in the ejecta (fig. 16).

Although only four craters in fixed gypsum dunes and alluvium were trenched, the character of ejecta and craters indicate that significant variations in styles of deformation occur with target material. The variations are particularly marked for craters in rock, sand-colluvium, very low density alluvium, and water-saturated gypsum lake beds. Ejecta from impact craters in rock with initial densities as great as 2.6 g/cm^3 are composed of rock fragments, crushed rock, and pieces of deformed missile. There is no evidence for compression of target materials and subsurface deformation like that described above, or penetration of missile parts beneath the surface. Indeed, some craters produced in limestone are small and remarkably shallow (fig. 37). Craters in weakly cohesive sand and colluvium do not produce the large undeformed blocks characteristic of craters in more cohesive materials such as fixed gypsum dunes. Rather, the largest ejecta fragments are compressed and sheared target material, and most of the ejecta is undeformed sand or colluvial debris. The deformed or fragmented missile may be completely ejected or may remain partly below the surface, depending on impact velocity and angle of impact. When the target material has a low density, the amount of ejecta is small, and it contains no compressed target material or missile parts. These materials remained below the surface.

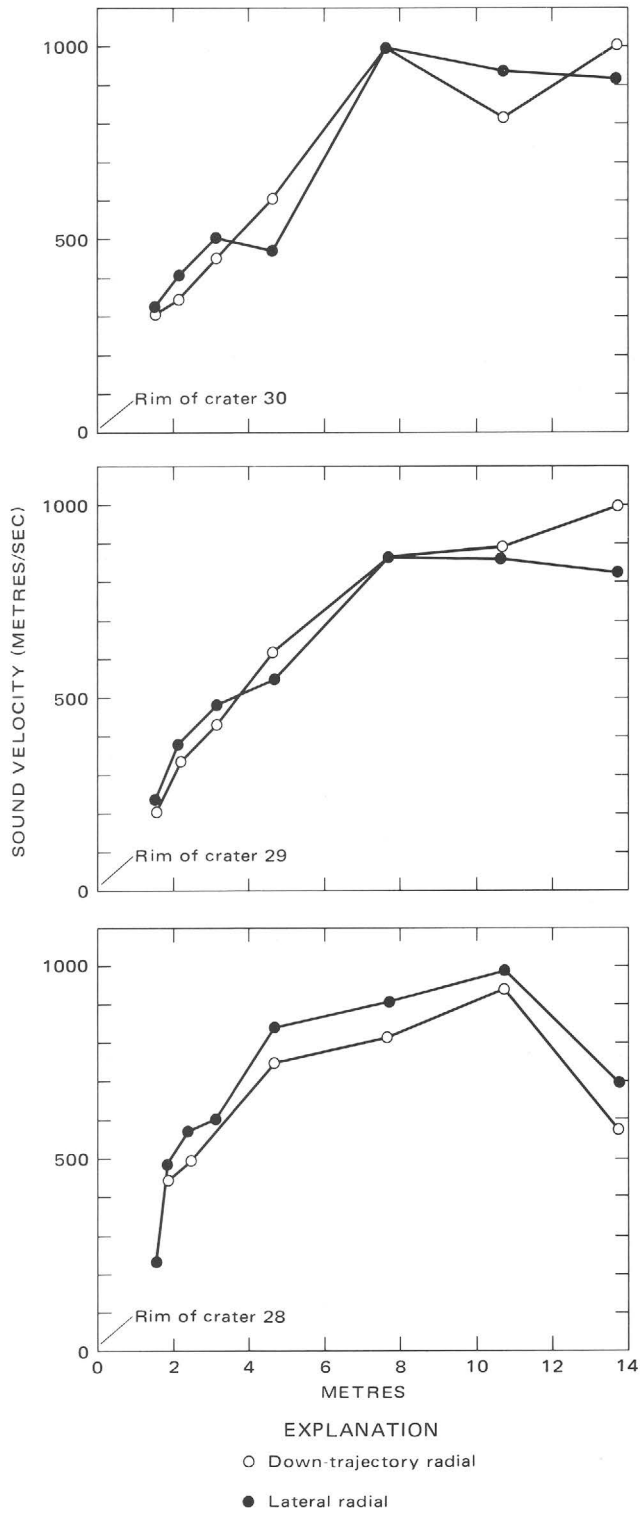

FIGURE 33.—Seismic velocities as a function of distance from crater rim. Open circles, velocities along a radial on down-trajectory flank; filled circles, velocities along a radial in lateral direction. Target was indurated gypsum dune. Geophone-source spacing, 3.05 m (10 ft). Note decrease in seismic velocity with decreasing distance from crater rim. (Craters 28, 29, and 30.)

The two craters in water-saturated gypsum lake beds differ from typical craters in two respects. First, ejecta from them contained no sheared and compressed target material; rather, many of the ejected fragments were essentially uncompressed or possibly dilated. Such a result might be expected because the pores of the lake beds were filled with water. Missile pieces were found outside one crater (Crater 7); none were found around the other (Crater 44). Second, the lake beds were layered such that deformation below the rims could be recognized and carefully traced. In both cases, the original beds were tilted upward on all crater sides. At the down-trajectory side of Crater 7 (fig. 38), a small white gypsum layer could be traced craterward from its original position below the surface where it steepened near the rim, overturned, and became part of the ejected flap. Up-trajectory, no layers could be traced continually, although the stratigraphic sequence in the ejecta was inverted. At Crater 44, folding and overturning below the rim was more complex and two layers formed a complex overturned syncline (fig. 38*B*).

Reasonable estimates of missile and target deformation can be made as a function of velocity of the missile at impact and density of the target, although there are other less important variables. Qualitatively, the importance of velocity in missile deformation results from the fact that the specific energy of the missile is proportional to the square of the velocity at impact. The importance of density results from a general correspondence of rock strength and density and hence deceleration of the missile at impact. Subsurface deformation of the target and the distribution of deformed material are strongly dependent on these variables. The degree of deformation of the missile is chiefly a function of its velocity and can be approximately classified into six groups (fig. 39): (1) bending the missile and stripping of appendages such as fins, (2) rupture of the missile and extensive internal damage to components, (3) rupture of missile, components, and spillage of the contained parts, (4) fragmentation of the missile and components into separate scattered contorted pieces, (5) powdering, fragmentation into pieces 10 or 15 cm across and less, partial melting, and partial to complete ejection of powder and pieces, and (6) powdering, fragmentation of missile into pieces a few millimetres across and less, partial melting, and ejection of all or most of the missile and its components. With each successive stage, it becomes increasingly difficult to find identifiable pieces of missile. At the highest velocities, the only identifiable remnants of the missile are dark gray coatings on fracture surfaces. The missile or pieces of it may be found at the surface, partly buried, or completely

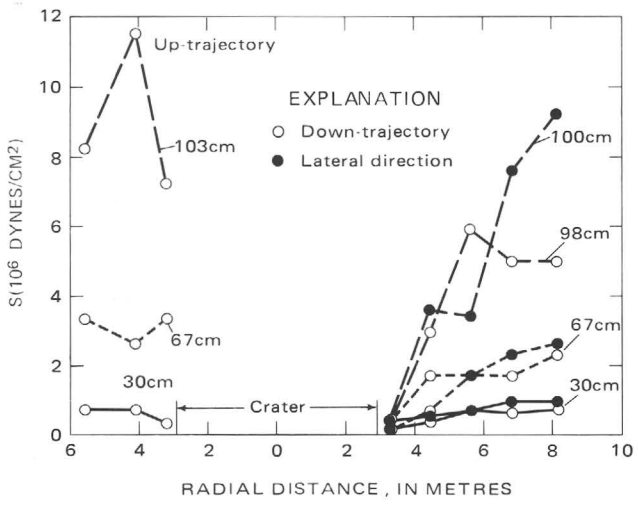

FIGURE 34.—Shear-vane measurement(s) for crater in fine silty sand and sandy silt along down-trajectory, lateral, and up-trajectory radial directions at various depths. Numbers indicate depth of measurement. Note large decrease of shear vane measurements near crater rim for lateral and down-trajectory sides. Change of shear-vane measurements not clearly correlated with distance from crater edge on up-trajectory edge. (Crater 24; see also frontispiece.)

FIGURE 35.—Open fracture near up-trajectory edge of crater to right. Surface between open fracture and crater wall displaced downward (Crater 17). Photograph courtesy of U.S. Army.

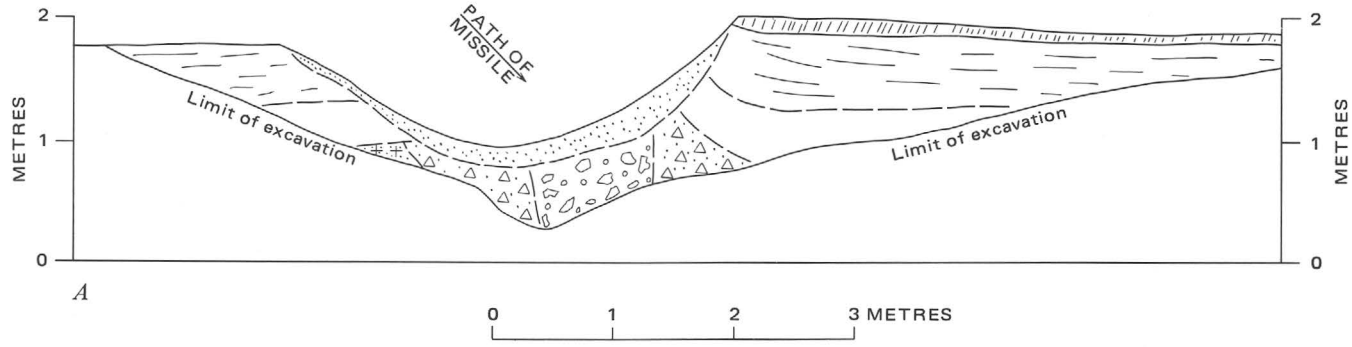

EXPLANATION

Talus and fallback

Fractured and brecciated gypsiferous silt

Silty alluvium

Thick ejecta

Gypsum layer

Mixed breccia gypsiferous silt

Gypsiferous silt

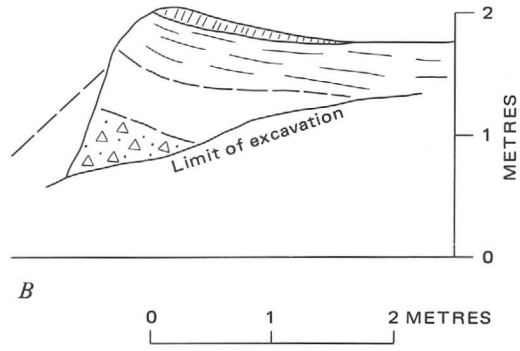

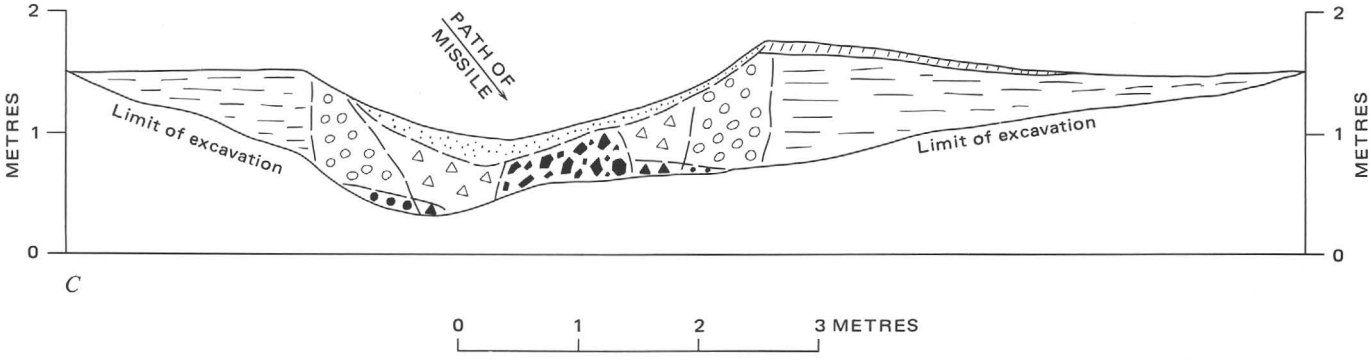

EXPLANATION

Mixed breccia of gypsum layer

Fractured silty alluvium

Fractured gypsum layer

Brecciated silty alluvium

Brecciated gypsum layer

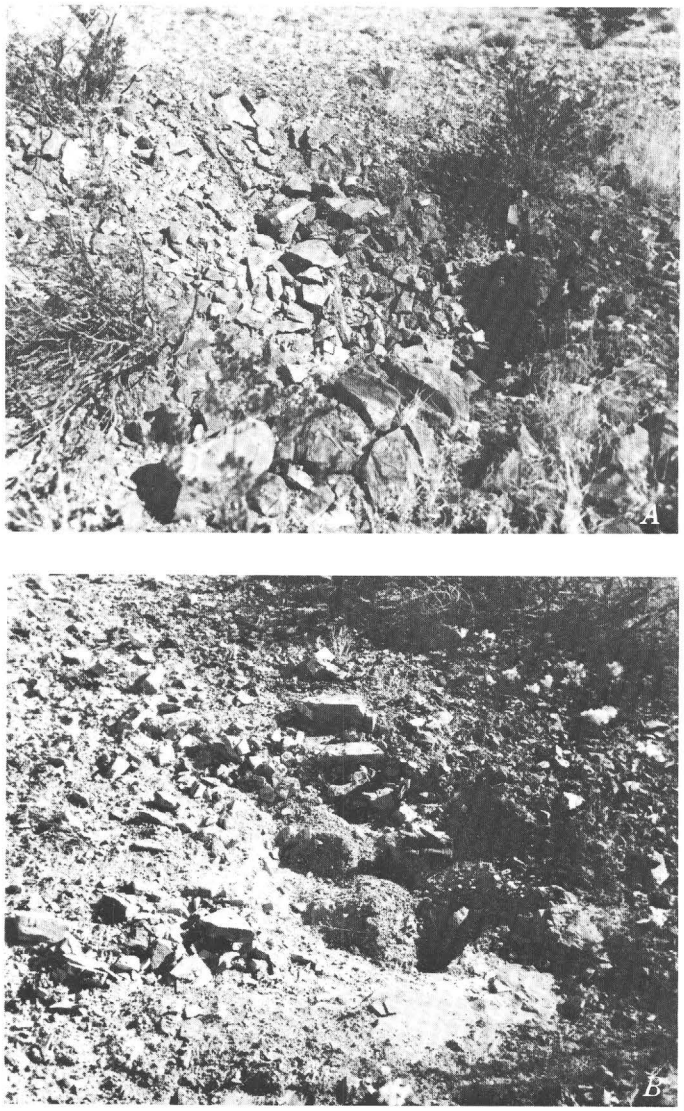

FIGURE 37.—Missile impact craters in rock. Craters are about 1.0 m across, less than 0.35 m deep. (E_p=2.9×10^{16} ergs, Θ=54°,Craters 22 and 23.) Photograph courtesy of U.S. Army.

buried. Estimated missile deformation and degree of burial are shown relative to density of target material in (fig. 39).

FIGURE 36.—Cross sections through craters, parallel and at right angles to plane of trajectory. *A*, Cross section through crater parallel to plane of trajectory showing mixed breccia and deformation of gypsum layer. Note gypsiferous layer is not displaced on up-trajectory side and is folded upward on down-trajectory side. (Crater 36; fig. 16.) *B*, Cross section through rim in lateral direction. Note gypsiferous layer is folded upward (Crater 35). *C*, Cross section through crater parallel to plane of trajectory showing mixed breccia composed chiefly of gypsum from gypsiferous layer (sheared and compressed) displaced upward above the horizon of the original layer. Gypsiferous layer on up-trajectory side has been fractured, brecciated, and displaced downward.

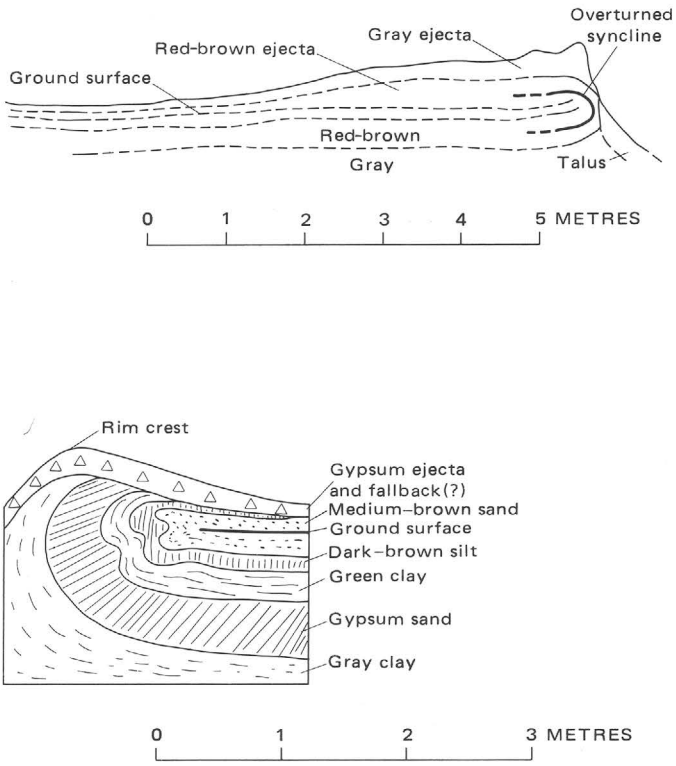

FIGURE 38.—Cross section showing structures observed in rims of craters in water-saturated gypsum lake beds. *A*, Simple overturned syncline on down-trajectory side. Crater is to right (Crater 7). *B*, Complex overturned syncline on down-trajectory side. Crater is to left (Crater 44).

Bomb-drop studies (Livingston and Smith, 1951, p. 105–110) form the basis for groups 1, 2, and 3. Fins from 1600AP and 2000SAP bombs are stripped from the body of the bomb and crumpled upon hitting sandstone ($\rho \approx$ 2.2 g/cm^3) at velocities up to 0.23 km/s with no deformation of the bomb bodies. Rupture of bomb walls occurs upon impact with sandstone at velocities near 0.3 km/s and contents such as ballast disperse and spill at velocities near 0.35 km/s. 2000GP bombs rebound from their craters in sandstone when impact velocities are near 0.29 km/s and penetrate less than their length at velocities less than 0.23 and 0.3 km/s. They are considered to be at the surface and unburied.

Data for groups 4, 5, and 6 come from missile impacts. Projectile debris from craters in sandstone and limestone in these groups are scattered across the surface to 60 m from the crater and none of it remains in the crater. At velocities exceeding 3.8 km/s, nearly all of the projectile, including coatings sheared and compressed fragments, are ejected when the target density is greater than 1.5 g/cm^3. Pieces of deformed projectile are rarely found, and where found, are a few milimetres across. Lines between deformation groups were drawn

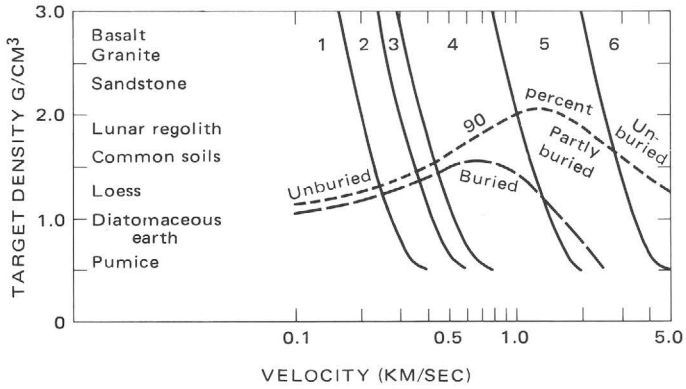

FIGURE 39.—Approximate velocities and densities for the six categories of projectile deformation and degree of burial of projectile or pieces of projectile resulting from impact with natural materials. Solid lines separate categories of projectile deformation: (1) bending missile body and stripping of appendages, (2) rupture of missile and extensive internal damage, (3) rupture of components and spillage, (4) fragmentation of missile and components with separate scattered contorted pieces, (5) powdering, fragmentation into pieces 15 cm across and less and partial melting, and (6) powdering, fragmentation into pieces a few millimetres across and less, partial melting, and ejection of all or most of missile parts. Dashed lines separate categories of degree of burial.

assuming deformation is proportional to target density times the square of the impact velocity.

Burial of projectile is based mainly on small-scale impact data. Missile impact data for complete burial is represented by only one crater. The laboratory data are from the impact of a BB with diatomaceous earth at 0.15 km/s (fig. 40). The BB penetrated about 2 diameters, forming a small tube. As shown in figure 40, the impact of a copper-jacketed lead .22 caliber bullet with diatomaceous earth ($\rho \approx 1.0$ g/cm) at 1.4 km/s did not produce a crater; rather, a camouflet formed beneath the surface of the target block connected to the surface by a small hole having about the same diameter as the projectile. Although banding in the diatomaceous earth can be traced across the camouflet, the brecciated cavity was found to have pieces of projectile scattered through it. Similar phenomena occurred for a missile impact crater in a target with a density near 1.2 g/cm^3. No pieces of projectile were found in the crater walls or ejecta, nor were fragments of sheared and compressed target materials coated with powdered projectile. A crater produced by a 0.178-g chrome steel sphere impacting diatomaceous earth (ρ=0.7 g/cm^3) at 4.42 km/s produced a crater and much of the projectile remained as small pieces beneath the surface (fig. 40) in small tubes below the crater floor.

The estimate of deformation, plotted (fig. 39) as a function of velocity of missile and density of material, represents a generalized description of impact phenomena and should not be taken as rigorous because of the large number of variables involved. Some suitably designed projectiles with large mass cross

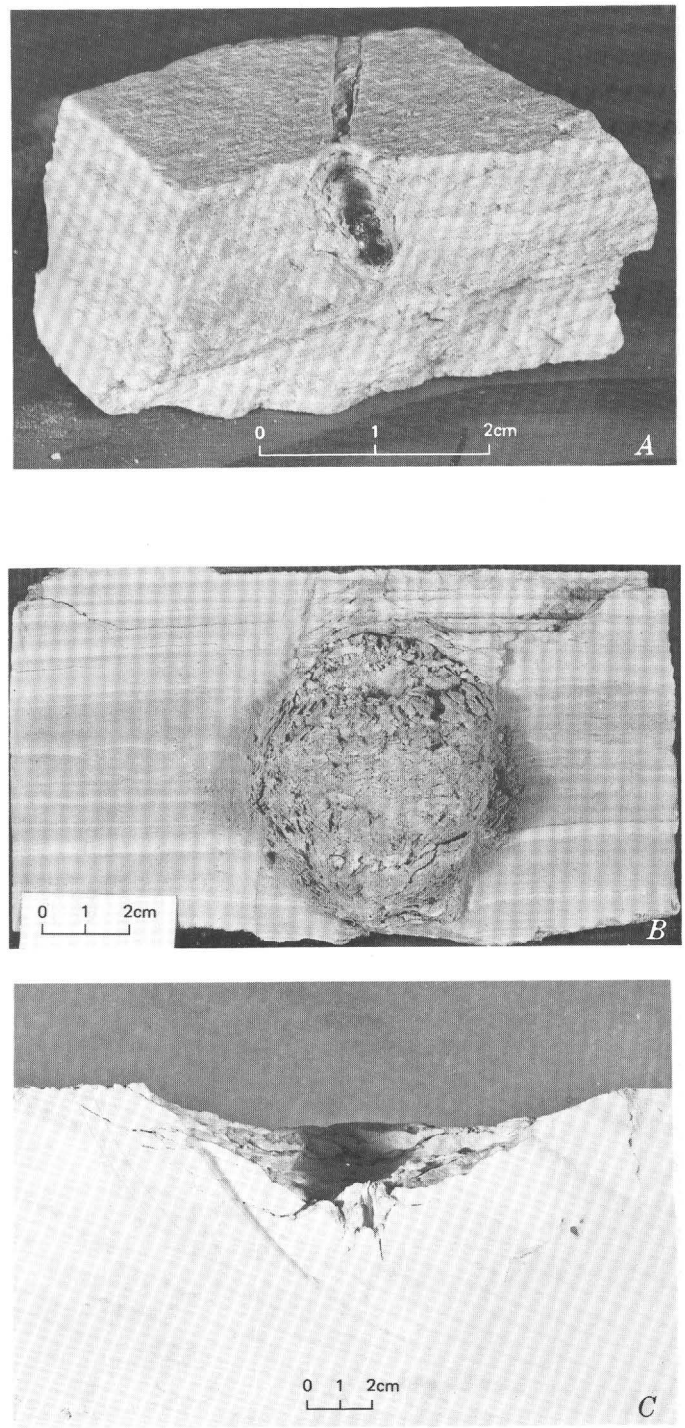

FIGURE 40.—Sawed sections showing results of small-scale experimental impacts with diatomaceous earth illustrating variety of impact phenomena. *A*, BB impact at about 0.15 km/s produces tubelike crater several BB diameters deep and one wide. *B*, Impact of copper-jacketed .22-caliber bullet at about 1.4 km/s produces cavity filled with breccia of diatomaceous earth and projectile pieces (experiment by Glen A. Miller, U.S. Geological Survey). Cavity connected to surface by small hole one projectile diameter across. Result similar to camouflet produced by deeply buried chemical explosives. *C*, Crater produced by impact of chrome steel sphere at 4.42 km/s in diatomaceous earth at Ames Research Center Free Flight Range, NASA.

sections penetrate rock and other natural materials to depths greater than 3.8 m at velocities near 0.3 km/s without being fragmented (Colp, 1968, p. 9, 12; Young, 1967a). Pore-pressure effects may substantially alter the estimate of projectile burial. In water-saturated targets, penetrations of slender projectiles at low velocities are greater than those in dry to moist targets (Young, 1967a; see tables 3 and 1). At higher velocities, where projectile fragmentation does occur, craters in water-saturated targets are larger and ejection of target-projectile material more complete than in porous, dry to moist targets (Moore and Lugn, 1965).

Response of target materials varies with projectile velocity and target density. Missile impacts produce crushing and disaggregation when the target material is rock. Target material compressed to densities near 2.0 g/cm^3 is abundant in craters in soils and materials with densities near 1.6 g/cm^3 in groups 5 and 6. For very low velocity impacts in soils, some compression occurs (Colp, 1968) in a plug driven ahead of the projectile and rock is crushed (Colp, 1968; Hartman, 1959). Sheared and compressed target material is absent in water-saturated targets.

QUANTITATIVE RELATIONS

MISSILE-IMPACT CRATER SIZE AND ENERGY

Quantitative correlations of dimensions of missile impact craters with each other and relative to missile kinetic energies show that: rim heights vary with rim radii, apparent crater radii with apparent crater depth, and rim radii with the sum of apparent crater depths and rim heights; apparent radii, apparent depths, crater volumes, and displaced masses vary with kinetic energy of the missile. Results of linear regression fits to the data in logarithmic form are shown in table 2 and figures 41 through 50. Not all craters were included in these least squares fits. Craters in water-saturated gypsum lake beds were excluded from the fit to data on volume, displaced mass, and kinetic energy because of the role of positive pore pressures in cratering. Others were excluded because they were not completely mapped, and for various other reasons. Craters excluded are listed in footnotes to table 2.

For some of the plots, the kinetic energy of the missile is corrected for the angle of impact using the sine of the angle. This correction was based on data for hypervelocity impacts of steel pellets with lead targets (Bryan, 1962).

Although the data show that the sizes of the craters correlate with the kinetic energy of the missiles, equations comparing apparent crater volumes and displaced masses with the kinetic energies of the missiles, corrected or uncorrected for impact angles, indicate that cratering becomes more efficient with increased kinetic energy; that is, the crater volume or displaced mass per unit of kinetic energy increases with kinetic energy. This increase is not accompanied by a significant change in crater shape as shown by the equation relating apparent depth and apparent radius. Rather, both the apparent depths and radii increase with kinetic energy in a manner consistent with greater cratering efficiency at greater kinetic energies.

The anomalously large displaced masses of craters in water-saturated lake beds and moist gypsum lake beds, relative to their respective kinetic energies corrected for angle of impact (fig. 50), are noteworthy. Plotted points for the craters in moist gypsum lake beds (fig. 50) are subparallel to the linear regression line but everywhere lie above it, thereby showing greater cratering efficiency at greater kinetic energies for a given target material. This is discussed further below.

COMPARISON WITH OTHER DATA ON EXPERIMENTAL IMPACTS

There appear to be correlations and similarities between missile impact craters and laboratory experiments as well as some low-velocity impact experiments in the field. Comparisons are somewhat impaired for several reasons: there are no laboratory experiments in the materials of the missile impacts; kinetic energies in laboratory experiments rarely exceed 10^{11} ergs; many laboratory experiments are performed at reduced pressures, whereas missiles impact in an atmosphere of air; and most of the missile velocities cannot be specified.

Increase of the efficiency of cratering with increase in the kinetic energy of the missile as found for missile impacts has been reported for craters produced by drill

TABLE 2.—*Results of least squares fits to missile impact data*
[Dimensions for equations are cm, cm^3, g, ergs, and degrees]

	Parameters	Equation	Standard error of estimate
1	Average rim height, rim radius[1]	$\bar{h}=0.118\ r_r^{0.944}$	0.078–0.178
2	Apparent depth, apparent radius[2]	$d_a=0.558\ r_a^{0.994}$	0.485–0.642
3	Apparent depth + avg. rim height, radius rim[1]	$d_a+\bar{h}=0.571\ r_r^{0.997}$	0.506–0.644
4	Apparent radius, kinetic energy[3]	$r_a=10^{-3.934}E_p^{0.412}$	$10^{-3.866}$–$10^{-4.002}$
5	Apparent radius, sine impact angle × kinetic energy[3]	$r_a=10^{-4.369}(\sin\theta E_p)^{0.445}$	$10^{-4.301}$–$10^{-4.437}$
6	Apparent depth, kinetic energy[4]	$d_a=10^{-4.182}E_p^{0.411}$	$10^{-4.082}$–$10^{-4.282}$
7	Apparent depth, sine impact angle × kinetic energy[4]	$d_a=10^{-4.588}(\sin\theta E_p)^{0.442}$	$10^{-4.488}$–$10^{-4.688}$
8	Apparent volume, kinetic energy[3]	$V_a=10^{-11.433}E_p^{1.205}$	$10^{-11.208}$–$10^{-11.658}$
9	Apparent volume, sine impact angle × kinetic energy[3]	$V_a=10^{-12.660}(\sin\theta E_p)^{1.298}$	$10^{-12.433}$–$10^{-12.887}$
10	Displaced mass, kinetic energy[3]	$M_d=10^{-11.086}E_p^{1.195}$	$10^{-10.845}$–$10^{-11.327}$
11	Displaced mass, sine impact angle × kinetic energy[3]	$M_d=10^{-12.272}(\sin\theta E_p)^{1.284}$	$10^{-12.027}$–$10^{-12.517}$
12	Rim radius, kinetic energy[4]	$r_r=10^{-3.311}E_p^{0.376}$	$10^{-3.241}$–$10^{-3.381}$
13	Rim radius, sine impact angle × kinetic energy[4]	$r_r=10^{-4.023}(\sin\theta E_p)^{0.426}$	$10^{-3.952}$–$10^{-4.094}$

[1]Sample size 51 (craters 1, 5, 9, 22, 23, 26, 35, 59, and 60 excluded).
[2]Sample size 52 (craters 9, 22, 23, 26, 35, 57, 59 and 60 excluded).
[3]Sample size 50 (craters 7, 44, 9, 22, 23, 26, 35, 57, 59, and 60 excluded).
[4]Sample size 53 (craters 7, 44, 9, 22, 23, 26, and 35 excluded).

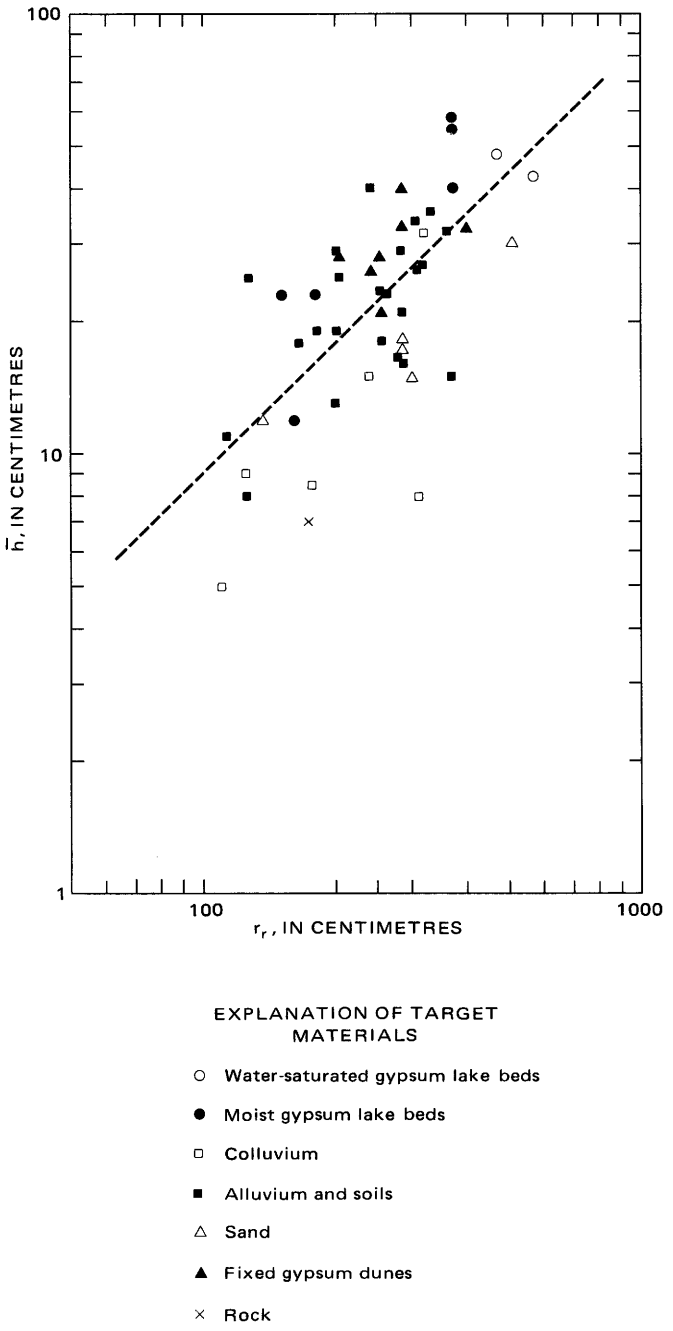

FIGURE 41.—Comparison between average rim height ($\bar{h}$) and rim radius (r_r). Dashed line represents least squares fit to 51 impact craters. Because of superposition, only 48 points are shown.

bits impacting synthetic stone and rock (Hartman, 1959, 1962), bullets impacting cement and marble at speeds up to about 610 m/s (Vanzant, 1963), artillery projectiles impacting rocks at up to 878 m/s (Tolch and Bushkovitch, 1947), and hypervelocity impact craters in basalt (Moore and others, 1965). Not all craters produced by projectile impact show an increase of efficiency with increased kinetic energy. The most notable exception is for impact cratering in cohesionless materials such as sand, where, for a given projectile, displaced mass is more nearly proportional to velocity than to kinetic energy and efficiency of cratering is therefore an inverse function of projectile velocity (Culp and Hooper, 1961; Cook and Mortensen, 1967; Oberbeck, 1970). For projectiles with constant velocity, displaced masses of craters in sand are proportional to the kinetic energy of the projectile raised to a power between 0.795 and 0.877 (Oberbeck, 1970). For experiments conducted in air, Cook and Mortensen (1967) find that volumes of craters produced by projectiles of equal sizes and velocities are larger in coarse sand than in fine sand.

Data on both ejected and displaced mass and kinetic energy for hypervelocity impacts with dense basalt (Moore and others, 1965) and sand (Oberbeck, 1970) extrapolated more than three orders of magnitude in energy converge near values of kinetic energies of 10^{15} ergs and ejected or displaced masses of 17×10^6 grams. These data, chiefly for normal incidence impacts at reduced pressures, are superposed on missile impact data for kinetic energies corrected for angle of impact) between 10^{15} and 10^{16} ergs. This relation is shown in the plots of figure 51, which represent the equation of Moore, Gault, and Heitowit (1965) (density ratio taken as 1), Oberbeck's equations for projectile velocities of 0.5 and 5.0 km/s, and the equation for missile impact

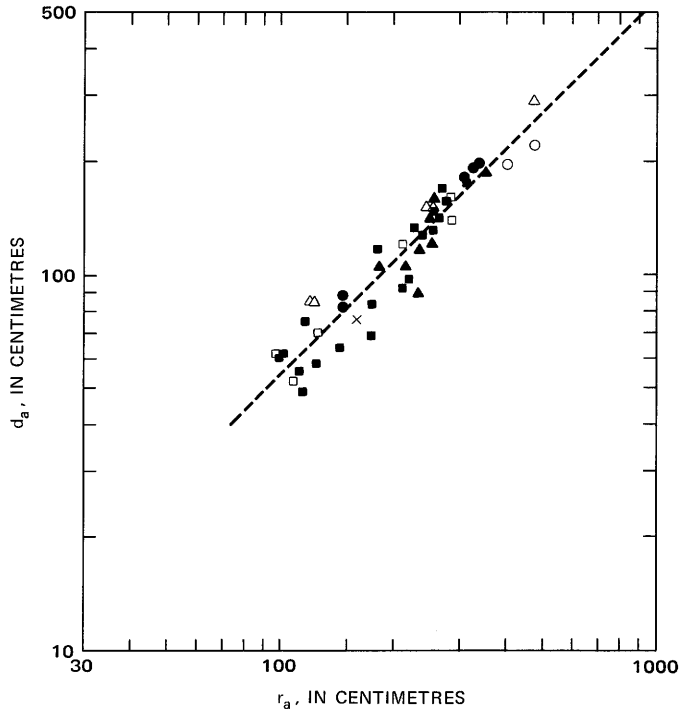

FIGURE 42.—Comparison between apparent crater depth (d_a) and apparent crater radius (r_a). Dashed line represents least squares fit to 52 impact craters. Because of superposition, only 48 points are shown.

cratering corrected for the angle of impact. For the experimental hypervelocity impacts with dense basalt, projectiles were accelerated to velocities of 0.88 to 7.3 km/s, attaining energies of 4.9×10^8 to 7.4×10^{11} ergs. Ejected masses[2] (M_e) ranged from several tenths of a gram to slightly more than 10^3 grams. For the experimental impacts with 200–700 μm quartz sand, projectiles were accelerated to 0.5 to 5.0 km/s, attaining energies of 2×10^7 to 10^{11} ergs. Craters had displaced masses between about 10 and 6×10^3 grams.

A crater produced by a missile impacting a sand dune of 40- to 100-mesh (0.147–0.417 mm) gypsum sand at known velocity allows a comparison with equations derived from small projectile impacts with sand in the laboratory. The missile produced a crater with an apparent volume of 97.5×10^6 cm^3 in the gypsum sand upon impact at 3.89 km/s with a kinetic energy of 73.5×10^{14} ergs. According to the Command at White Sands, the mass per unit area of the missile was between 95.5 and 24.8 g/cm^2, depending on how it hit. A mass per unit area near 95.5 g/cm^2 is most probable. Mortensen (1967), to explain his data on impact of .30-caliber and .22-caliber bullets in sand at velocities up to 1 km/s, proposed an equation of the form

$$\frac{E_p}{\frac{m}{A}\ (V_a)} = K(V_p)^{0.8}, \qquad (14)$$

where

E_p is the kinetic energy of the projectile,
m is the mass of the projectile,
A is the cross-sectional area of the projectile at impact,
V_a is the volume of the crater,

[2]Ejected mass (M_e) for small craters in basalt is the mass of material ejected from the crater. Displacement mass (M_d) is the product of target density and apparent crater volume.

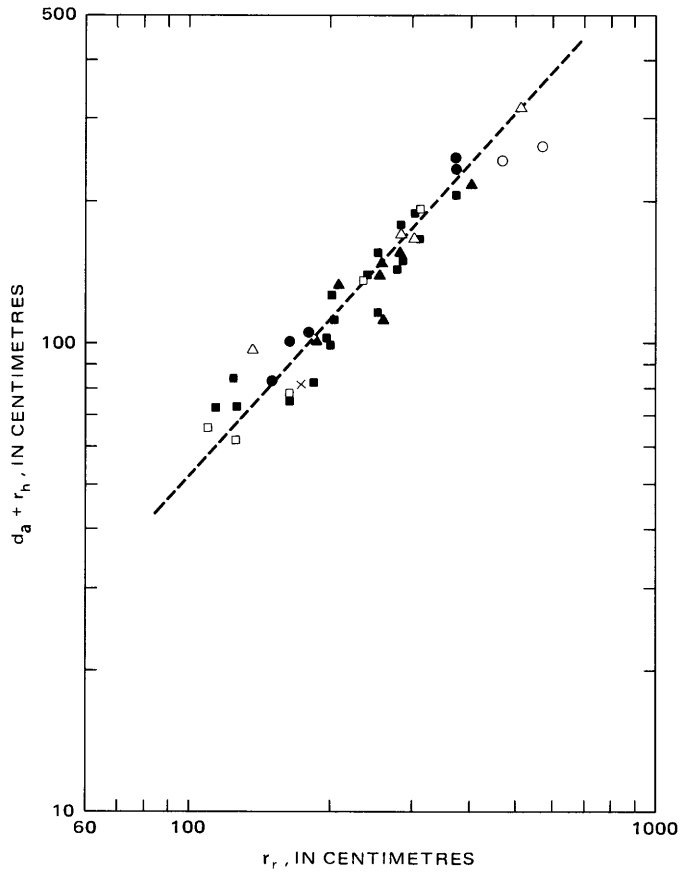

FIGURE 43.—Comparison between the sum of apparent crater depth and rim height (d_a and r_h) with rim radius (r_r). Dashed line represents least squares fit to 51 impact craters. Because of superposition, only 42 points are shown.

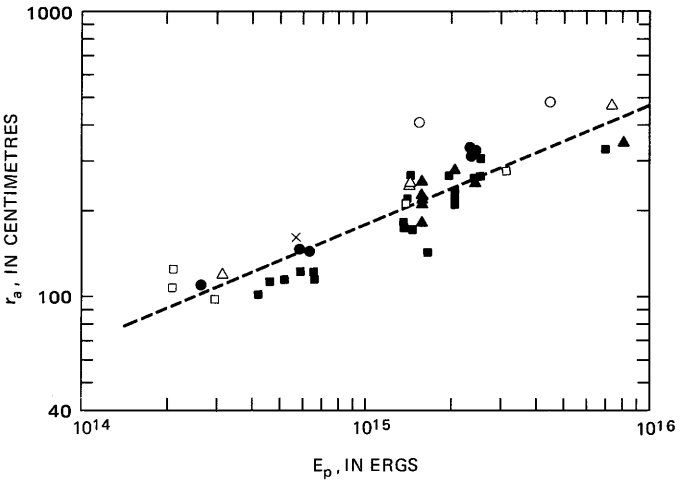

FIGURE 44.—Comparison between apparent radius (r_a) of crater and kinetic energy of missile (E_p). Dashed line represents least squares fit to 50 impact craters. Because of superposition, only 46 points are shown.

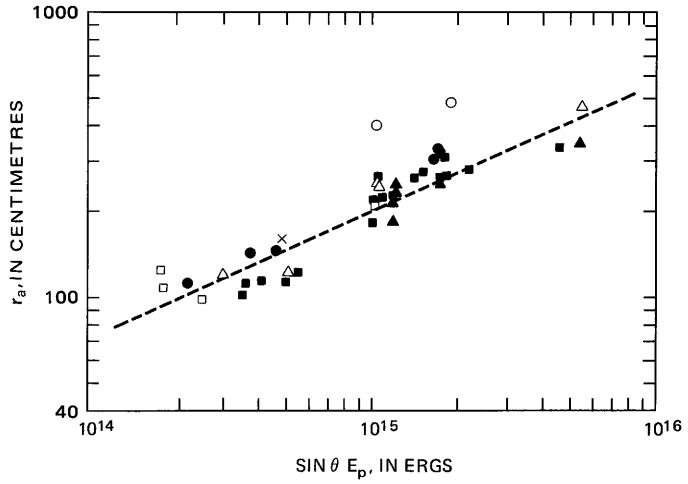

FIGURE 45.—Comparison between apparent radius (r_a) of crater and product of sine of angle of impact and kinetic energy of missile (sin Θ E_p). Dashed line represents least squares fit to 50 impact craters. Because of superposition, only 41 points are shown.

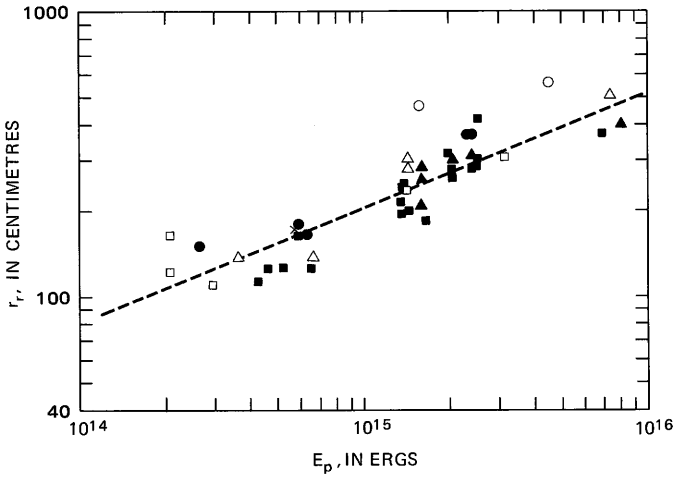

FIGURE 46.—Comparison between rim radius (r_r) and kinetic energy of missiles (E_p). Dashed line represents least squares fit to 53 impact craters. Because of superposition, only 43 points are shown.

V_p is the velocity of the projectile, and
K is a coefficient.

The value of the coefficient K depends on grain size of the target. For +20–14 mesh (0.833–1.17 mm) sand, K is 86.4; for +48–28 mesh (0.295–0.589 mm) sand, K is 110; and for +100–60 mesh (0.147–0.246 mm) sand, K is 210. Substitution of the appropriate values for the missile impact crater yields values of K between 27 and 103, a result indicating the missile impact crater is larger than expected. Adjustments for angle of impact further reduce these values of K.

It can be shown that Oberbeck's results (1970) can be fitted to equations of the form

$$\frac{E_p}{(\frac{m}{A})^{1/2} M_d} = CV_p, \qquad (15)$$

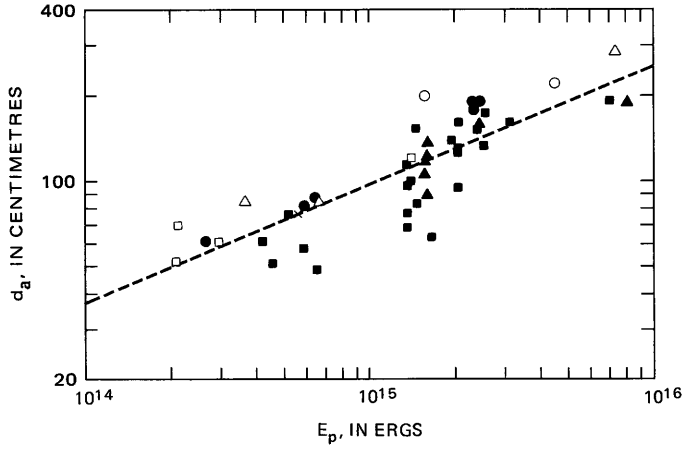

FIGURE 47.—Comparison between apparent depth (d_a) and kinetic energy of the missile (E_p). Dashed line represents least squares fit to data of 53 impact craters. Because of superposition, only 46 points are shown.

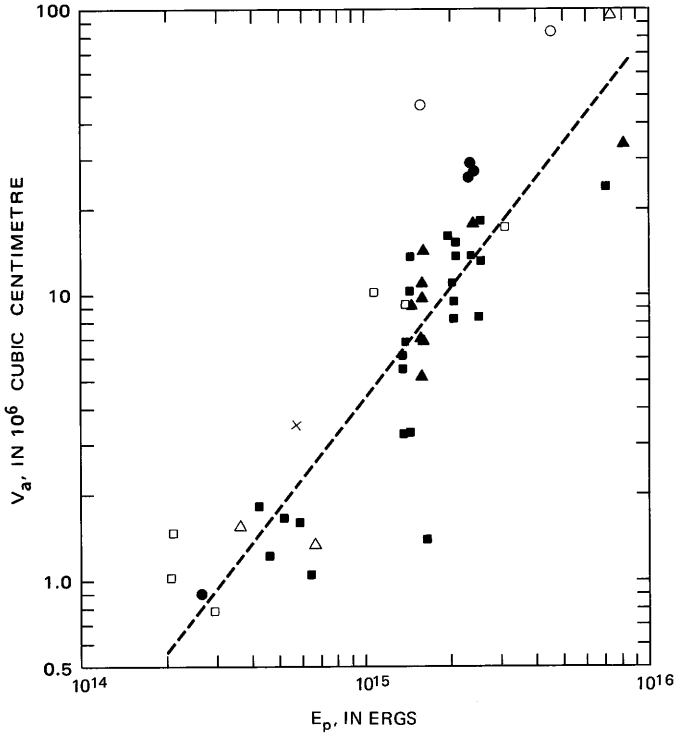

FIGURE 48.—Comparison between apparent crater volume (V_a) and kinetic energy (E_p). Dashed line represents least squares fit to data for 50 impact craters.

where $C = 47 \pm 7$. For the missile impact crater in gypsum sand (Crater 56), C is 14.3 to 27.9 or 9.9 to 19.4 when corrected for the angle of impact using $(\sin \Theta)^{2/3}$. The results are of same order of magnitude, but Crater 56 is larger than predicted. Direct comparison of the displaced mass and the kinetic energy $\times \sin \Theta$ for Crater 56 with Oberbeck's equation predicting the larger displaced masses indicates that Crater 56 is 1.8 times larger than expected. Indeed, it is about 1.8 times larger than the line of the least squares fit to the missile impact data. By all standards, Crater 56 is larger than expected. The reason for this is not entirely clear. The difference could arise from differences in projectile properties, errors in energy estimates for the missile, the effects of air pore pressures, or local terrain slope.

Low-velocity impact studies have been conducted in the moist gypsum lake beds at White Sands Missile Range (Young, 1967b). Slender projectiles, weighing 1.02×10^5 to 1.14×10^5 grams and 13.7 to 20.3 cm in diameter, were dropped at velocities between 48 and 84 m/s, producing tubelike craters 51 to 134 cm deep filled by the projectile. Displaced masses, taken as the target density $\times$ projectile cross section area $\times$ depth of penetration, yield ratios of kinetic energy to displaced masses between 0.46×10^8 and 0.99×10^8 ergs/g. These ratios are comparable to those of missile impact craters in the same material, which range between 0.32×10^8

ergs/g for the larger ones and 1.2×10^8 ergs/g for the smaller ones. The values are surprisingly close to those of the low-velocity penetrators, although there is little correspondence in characteristics of the missile impact craters and the low-velocity penetration.

COMPARISON WITH CRATERS PRODUCED BY EXPLOSIVES

Sizes of craters produced by missile impacts are generally near those produced by chemical explosives when the kinetic energies of the missiles (corrected for the angle of impact) are equal to the TNT equivalent energy of explosives with shallow depths of burial (Moore, Kachadoorian, and Wilshire, 1964; Moore, 1966a). Empirical correlations have been suggested for small laboratory impact craters in rocks and small explosion craters (Gault and others, 1963, p. 29; Gault and Moore, 1965) and shown for small experimental impact craters and explosive craters in sand (Oberbeck, 1970, 1971). The problem of exact comparisons for a variety of natural materials and projectile conditions is not resolved, however, The effects on impact cratering of target properties such as porosity, cohesion, angle of internal friction, moisture content, and equation of state and projectile properties such as density, velocity, size, shape, and equation of state have not been studied in sufficient detail.

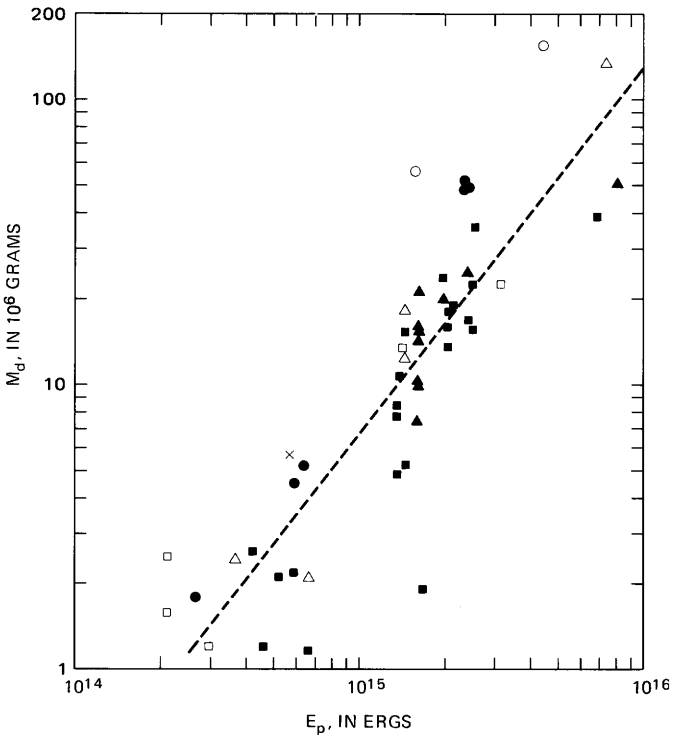

FIGURE 49.—Comparison of displaced mass (M_d) and kinetic energy of missile (E_p). Dashed line represents least squares fit to data for 50 impact craters.

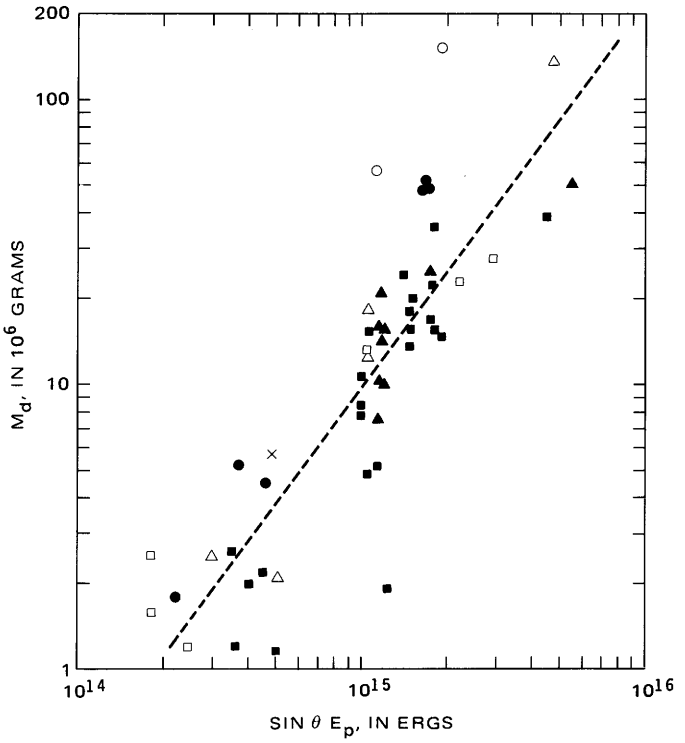

FIGURE 50.—Comparison of displaced mass (M_d) and product of sine of angle of impact and kinetic energy of missile (sin θE_p). Dashed line represents least squares fit to data for 50 impact craters.

Craters produced by explosives are markedly dependent on the scaled depth of burst[3] (Duvall and Atchison, 1957; Nordyke, 1961; Vortman, 1963); the equivalent scaled depth of burst for an impact event is not clear. Both the tube-crater in diatomaceous earth produced by the BB (fig. 40*A*) and the craters produced by low-velocity penetrators (Young, 1967b) bear little resemblance to craters produced by chemical explosives. The breccia-filled cavity produced in diatomaceous earth by the .22-caliber bullet (fig. 40*B*) is similar to camouflets produced by charges of chemical explosives with large scaled depths of burst that do not produce craters (U.S. Army Corps of Engineers, 1958). Some missile impact craters may be similar in that a breccia-filled cavity underlies an anomalously small crater (such as Crater 43). At velocities of 4.43 km/s, small craters are produced in diatomaceous earth (fig.

[3]The scaled depth of burst is a ratio of dimensions describing experimental conditions for an explosive event and is used to compare results from events with differing conditions. For cube-root or Lampson scaling, the scaled depth of burst is equal to the actual depth of burial of the explosive (d_{ob}) divided by the cube root of the TNT weight-equivalent of the explosive (W) or $d_{ob}/W^{1/3}$. It is commonly expressed in ft/(lb)$^{1/3}$ (Duvall and Atchison, 1957). For Nevada Test Site data, the scaled depth of burst has been taken as the actual depth of burial of the explosive divided by the 3.4th root of the TNT weight-equivalent of the explosive of $d_{ob}/W^{1/3.4}$. It is commonly expressed in m/(kiloton)$^{1/3.4}$ (Nordyke, 1962). Other scaling laws use different scaled depths of burst such as overburden scaling (Chabai, 1965), fourth-root scaling (Chabai, 1965; Herr, 1971), and counterpressure scaling (Sun, 1970). Small experimental impact craters in rock imply scaling laws for which scaled depths of burst would differ from all of those given here (Moore and others, 1965; Mandeville and Vedder, 1971; Gault and Moore, 1965).

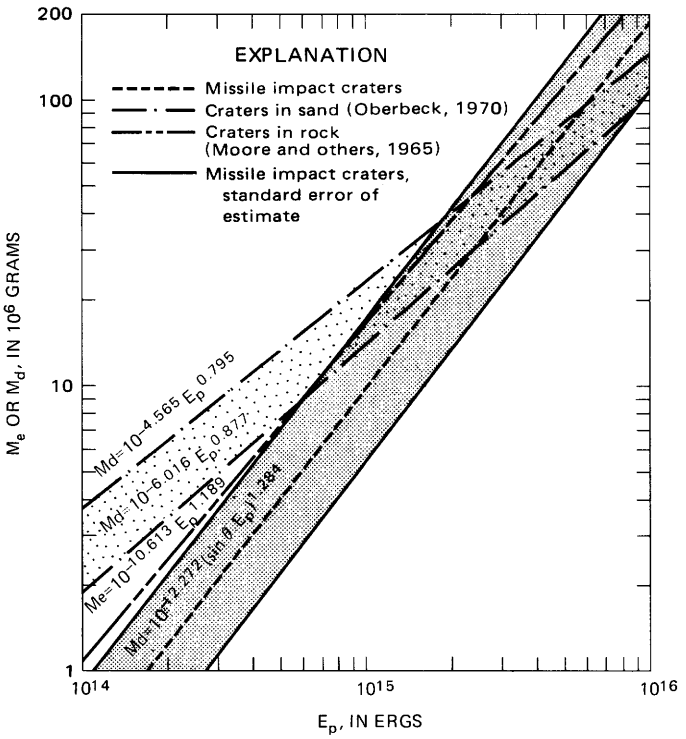

FIGURE 51.—Ejected (M_e) or displaced (M_d) mass and kinetic energy (E_p) corrected for angle of impact (sin Θ) for missile impact craters, extrapolation of hypervelocity impact equation for rock targets, and extrapolation of impact data on craters in sand. Results compare well in the region of 10^{15} to 10^{16} ergs.

40*C*). The effective scaled depth of burst for impacts with porous targets varies, especially with velocity.

For dense coherent rocks such as basalt, the dependence between cratering and projectile velocity is different. Projectiles at velocities near 0.21 km/s simply bounce upon impact and no crater is produced. Low-velocity projectiles with large masses per unit area (Young, 1967b), form tubelike craters. Small projectiles at velocities from 0.88 to 7.3 km/s produce craters by a combination of crushing and spallation (Moore, Lugn, and Gault, 1962). Variations similar to those described occur with missile impacts as in the very small craters in rock, for example, craters 22 and 23 in sandstone and limestone (fig. 37).

As part of a passive seismic study of missile impacts (Latham and others, 1970), craters were produced in colluvium and alluvium near the missile impact craters using commercial explosives detonated at small scaled depths of burial. Comparison of the displaced masses of craters produced by missile impacts and explosives with energies near the kinetic energies of the missiles (corrected for the angle of impact) show they are reasonably close (fig. 52; table 4). For impact craters in colluvium, there was no evidence for a camouflet; the craters compare well with explosive craters with small scaled depths of burst (0.15 m/(kg)$^{1/3}$ or 0.38 ft/(lb)$^{1/3}$). Other impact craters in colluvium are close to the explosive craters in colluvium plotted in figure 52. As other data on craters produced by chemical explosives (Robertson, 1966) agree fairly well with the results for colluvium (fig. 52), the results appear valid. Both the impact crater (Crater 43) and explosive craters in alluvium are anomalously small for their energies when compared with the other craters in alluvium. One impact crater (Crater15) in alluvium about a mile to the south of Crater 43 is consistent with the results for impacts and explosive craters in colluvium. The cause for the samll explosive craters may be a caliche layer in the alluvium. Mapping shows one of the explosive craters (0.12 m/kg$^{1/3}$ or 0.29 ft/lb$^{1/3}$) was clearly affected by this layer because a flat floor with a central peak was produced at the appropriate depth for the caliche layer (see also, U.S. Army Corps of Engineers, 1958b). On the

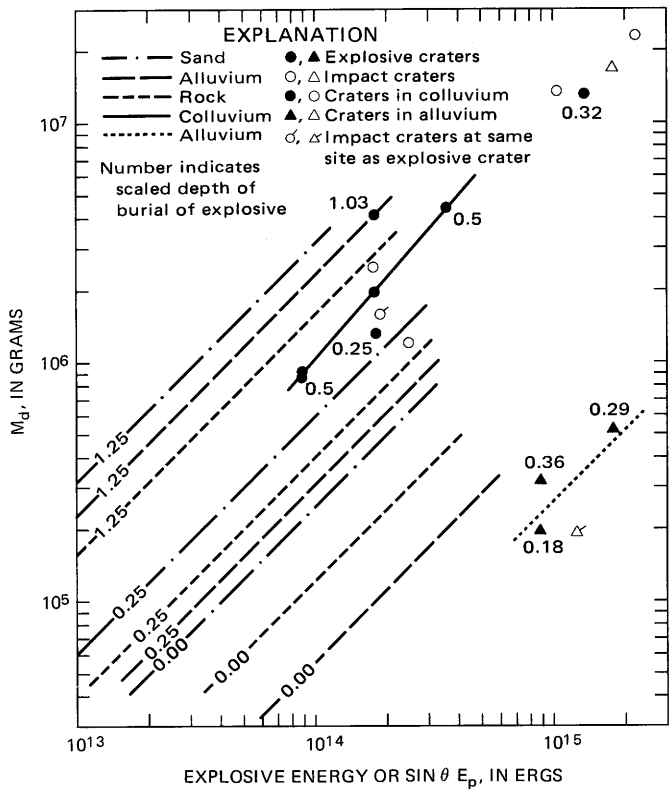

FIGURE 52.—Comparison of displaced masses of craters produced by chemical explosives (after Robertson, 1966), chemical explosive experiments at White Sands Missile Range, and missile impact craters with comparable energies. Filled circles represent craters produced by chemical explosives in colluvium with scaled depth of burst indicated; open circles, missile impact craters in colluvium; flagged open circle, missile impact crater in same material as chemical explosive craters; filled triangles, craters produced by chemical explosives in alluvium with scaled depths of burst indicated; open triangle, missile impact crater in alluvium near explosive craters; flagged open triangle, missile impact crater in same material as explosive crater. Scaled depth of burial is in ft/(lb)$^{1/3}$ (1.0 ft/(lb)$^{1/3}$=0.40 m/kg$^{1/3}$).

other hand, ejecta from the missile impact crater contained large amounts of the caliche and there was no flat floor. Because there were few or no missile pieces in the ejecta, the pieces must have remained below the surface in a brecciated mass. This suggests that Crater 43 may have had a camouflet somewhat like that in diatomaceous earth (fig. 40*B*). Simple generalizations about equivalent scaled depths of burial for impact craters are unjustified and few simple correlations can be expected for projectile velocities as great as 7 km/s (see for example, Gault and others, 1966; Moore and Robertson, 1966; Moore, Gault, Heitowit, and Lugn, 1964; Moore and others, 1965).

Additional parallels between explosive craters and missile impact craters exist. Both explosive and impact craters produced in very wet fine-grained materials are larger than their dry counterparts for energies near 10^{15} ergs (Moore and Lugn, 1965; fig. 53). The missile impact craters in water-saturated targets (Craters 7 and 44) are five to six times larger than the least squares regression line (fig. 50). Generalized results from explosive cratering experiments (Robertson, 1966) yield a similar result, and explosive craters with energies near 10^{15} ergs are about 10 times larger than their dry counterparts (fig. 53). Further, both explosive and impact craters produced in a wide variety of natural materials exhibit a large amount of scatter (fig. 52). Craters produced in sand, rock, and alluvium with the same scaled depths of burial and charge energies differ in size and much of the scatter in the missile impact data may result from such effects.

Structurally, explosive craters and missile impact craters are similar. Mixed breccias were produced by the Jangle U and Teapot ESS explosive cratering experiments (Shoemaker, 1960) and conjugate fractures are produced in materials around detonated explosives (Allsman, 1960). Sheared and compressed alluvium are common in ejecta from craters produced by explosives at the Nevada Test Site.

DISCUSSION OF DATA

Six aspects of the data on missile impact craters are critical: (1) the relation of the symmetry of the crater to the path of the missile, (2) the effect of the angle of impact on crater size, (3) the relation of crater size to impact energy, (4) the compression of target material, (5) the effects of water in the target material, and (6) extrapolation of data on sizes of missile impact craters to larger and smaller craters.

SYMMETRY AND PATH OF MISSILE

As mapping has shown, ejecta and crater profiles are normally bilaterally symmetrical about the plane of the missile trajectory, a result of the oblique trajectory.

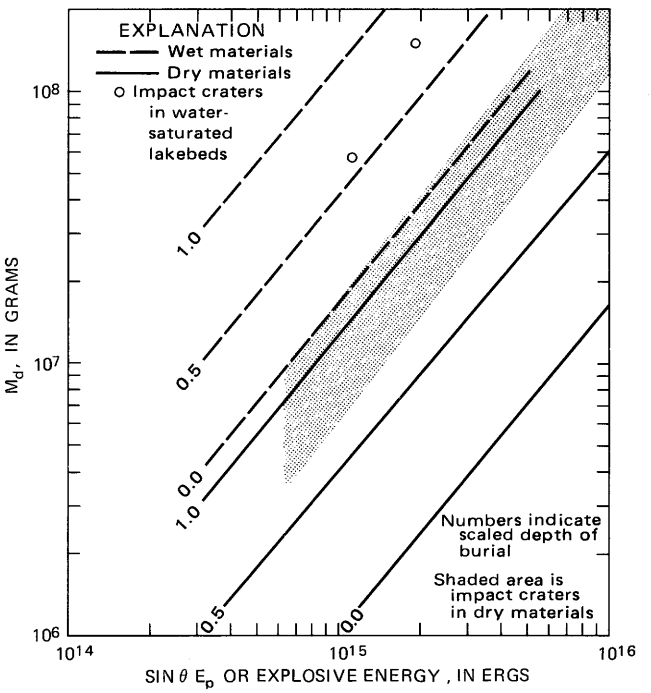

FIGURE 53.—Comparison of impact and explosive (after Robertson, 1966) craters in dry to moist targets and water-saturated targets. Note that craters produced in wet materials are larger than those produced in dry materials when the energies are the same and scaled depths are equal.

Conservation of momentum suggests that this type of symmetry should arise from an oblique impact and that there should be a concentration of ejecta down-trajectory. A rough estimate of the direction of origin of the missile can be made when the crater is on flat terrain. This has been done for a number of craters using chiefly thick ejecta patterns around the crater and observing the side of the crater which has little or no thick ejecta. The mapped lines of thick ejecta extending in lateral directions from the up-trajectory side of the crater tend to be at right angles to the trace of the missile.

Estimates of direction of origin for a number of craters are plotted in figure 54, where it may be seen that one group of missiles originates from a point along an azimuth of 35°, a second group from points along an azimuth between 135° and 195° (reference for azimuths is arbitrary). As these azimuths are consistent with the directions of the launch sites, crater symmetry yields some information on the direction of origin of the missile.

ANGLE OF IMPACT

The effect of angle of impact on crater size is not clearly understood. The sine of the angle of impact was used here to compensate for the effect of the oblique trajectory on crater size, in agreement with data on hypervelocity impacts with lead targets (Bryan, 1962).

Some workers have reported a sine-squared dependence with angle of impact (Partridge and Van Fleet, 1958). This does not seem reasonable for missile impact craters since it would increase the slope of the volume or displaced mass-energy curves significantly. Data of other workers (Gault and others, 1965, p. 129), using sand targets, indicate that the kinetic energy should be corrected using the two-thirds power of the sine of the impact angle. This correction would not critically affect the missile impact results reported here. For impact angles less than about 15°, a furrow or a chain of craters may be produced. Such a result has been obtained for laboratory impacts in sand with angles of impact of 4° (Swift and others, 1970).

The possibility that a large angle of impact might actually result in smaller apparent craters in certain target materials, especially porous ones, and with certain projectiles, especially dense, long slender ones, cannot be ignored. In such cases shock and stress waves could propel projectile and target materials chiefly in the directions of the trajectory but partly radial to it. For a vertical impact, materials would then be driven mainly downward in the target, resulting in camouflets such as the one described for diatomaceous earth. For an oblique impact, most of the shock and stress waves would propagate in the target material along the trajectory but some would propagate upward at an angle to the local surface. Radial components of the waves would interact with the local free surface, ejecting material to produce a larger crater than that for a vertical impact. Morphology of the missile impact craters, the cross sections through them, and ejecta distributions support this. With very small angles of impact, furrows would be produced. The largest apparent craters in porous rocks, then, could result from some angle of impact between perhaps 30° and 60°.

CRATER SIZE AND ENERGY

Linear dimensions of the craters were found to be proportional to the kinetic energies of the missile (corrected or uncorrected for the angle of impact) raised to a power near 0.4 and the relation of crater volume and displaced masses with energy was commensurate with those for the linear dimensions (table 2). This result differs significantly from Lampson scaling for explosive cratering (see for example, Duvall and Atchison, 1957), and Nevada Test Site scaling (Nordyke, 1962). Lampson scaling implies linear dimensions are proportional to the cube root of energy and that crater volume is proportional to energy; the Nevada Test Site scaling indicates linear dimensions are proportional to the $^1/_{3.4}$th power of energy or charge weight. Indeed, the results for missile impacts are more akin to data on small laboratory impact experiments with rocks for

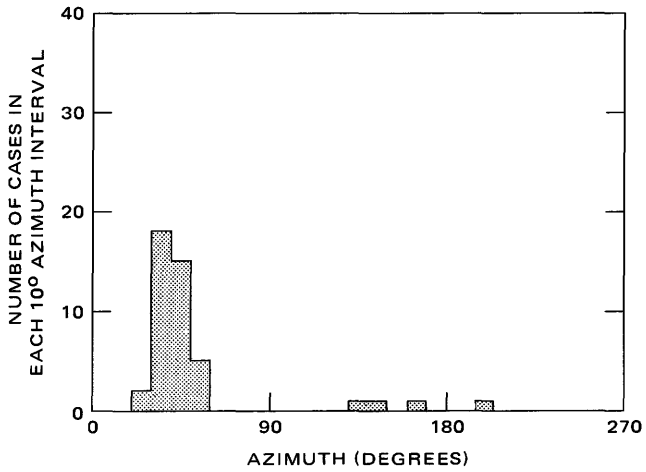

FIGURE 54.—Azimuths of traces of missile estimated from crater morphology and ejecta distribution. Reference for azimuths is arbitrary.

which volumes and displaced masses are proportional to the 1.189th power of the projectile kinetic energy. Such a relation could arise for a number of reasons: (1) some of the data on missile impacts are near a threshold condition for crater formation; (2) the effective strength of the target material decreases with increase in size; and (3) masses, sizes, length-to-width ratios, and orientations of the missiles at impact differ in a systematic but unknown manner with energy. It is not possible to differentiate the effect of these parameters; their possible effects are discussed below.

Some of the craters produced may be near a velocity or specific kinetic energy threshold below which craters do not form. This threshold may be of two types. The first relates to dense cohesive materials such as rock for which no craters are produced when the specific kinetic energy is too small. For the impact of ¼-inch-diameter hemispherical drill bits impacting synthetic stone at a velocity of 4.3 m/s, craters form by crushing and spalling above kinetic energies of 4.1×10^8 ergs; but below this energy no spalling occurs and relatively small craters are formed (Hartman, 1959). A BB impacting basalt at velocities near 0.15 km/s bounces without producing a crater. Some missile impacts with rock may be near such an energy threshold (Craters 22 and 23; fig. 37). The threshold of the second type is a factor in cratering in porous targets, illustrated with diatomaceous earth (fig. 40). At low velocities small apparent craters result because subsurface breccia-filled cavities are produced whereas at higher velocities more nearly hemispherical shock and stress waves produce a crater by ejection and spallation of target material. The existence of a threshold condition could mean that equations of the form given in table 2 are not correct, that the fit is of the form

$$V_a = K(E_p - E_0)^n, \qquad (16)$$

where K is a coefficient, n is a power coefficient, and E_0 is threshold energy required for cratering. Data available are not sufficient to test such an equation for the missile impact craters.

Crater size-energy relations similar to those for the missile impact craters have been reported by a number of observers (Hartman, 1959; Vanzant, 1963; Moore and others, 1965; Mandeville and Vedder, 1971) for very small impact craters. The data have been explained as a result of an increase in the ratio of body forces and surface forces with increase in size of event (Vanzant, 1963) and a decrease in strength of materials with increase in size because of defects which statistically increase in length or become prevalent in jointed or fractured materials (Moore, and others, 1965; Hubbert and Willis, 1957).

The third possibility cannot be explored in any detail because data available are not complete. If missiles with lower kinetic energies impacted with an orientation systematically different than those with higher energies, the mass per unit area of the impacting missiles could conceivably produce a systematic bias in the relation of crater dimensions to kinetic energy. Alternatively, some other property such as bulk density of the missiles may vary systematically with kinetic energy.

COMPRESSION OF TARGET MATERIAL

Large parts of the ejecta and mixed breccia beneath the crater floors are composed of sheared and compressed target material when the target material is compressible and projectile conditions are suitable. Compressible target materials include alluvium, indurated gypsum dunes, and sand. For some craters as much as 20 to 30 percent of the ejecta is composed of fragments compressed to densities as high as 2.2 g/cm^3 from materials with initial densities of 1.2 to 1.6 g/cm^3. The fragments are bounded on some or all sides with striated and grooved surfaces showing movement between fragments and indicating high confining pressures.

Both high confining pressures and compression of target material is an expected result from impact craters in porous materials. Graphic impedance match solutions for peak shock pressures (Gault and Heitowit, 1963) resulting from the impact of aluminum and nylon projectiles with porous targets at 3.9 km/s are one hundred to several hundred kilobars, as shown in figure 55*A*, a plot of data on shock compression of natural materials after Bass, Hawk, and Chabai (1963). Shock pressures this high produce much compression of some materials. Ratios of compressed volume to original

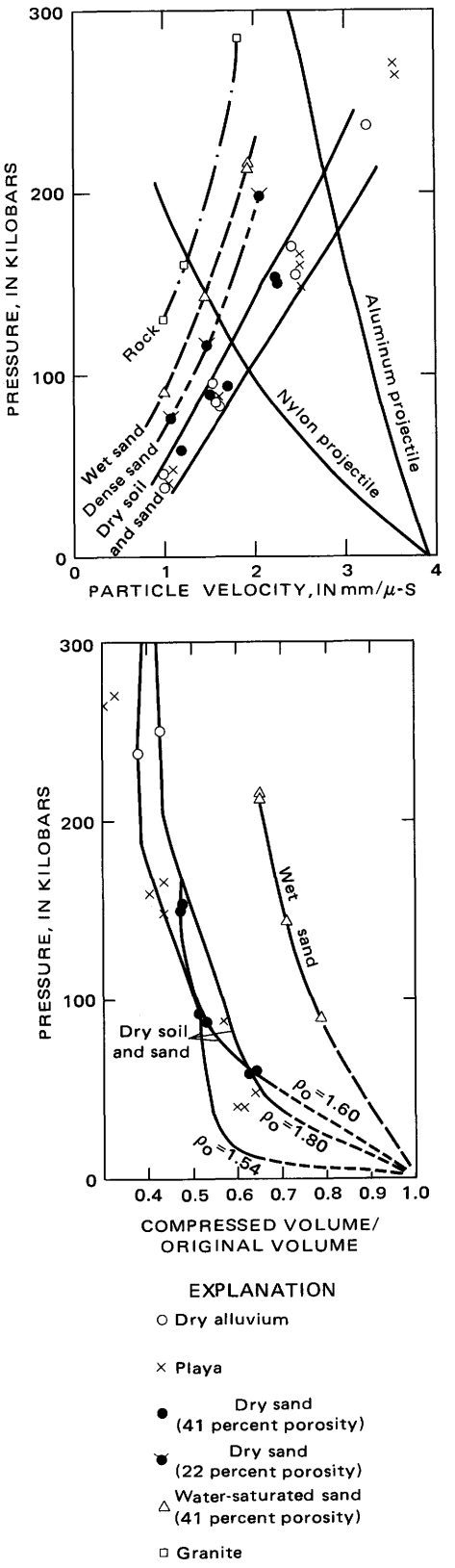

FIGURE 55.—*A*, Graphic impedance match solutions for peak shock pressures produced by the impact of nylon and aluminum projectiles with dry soils and sand, water-saturated sand, and granite at 3.9 km/s. *B*, Compression of dry soils, sand, and water-saturated sand in shock wave. Note sizable compression of soil at shock pressures as low as 5 to 10 kbar. After Bass, Hawk, and Chabai, (1963).

volume are 0.57 to 0.38, corresponding to compressed densities of about 3.2 to 4.0 g/cm^3 for original densities (ρ_0) of 1.3 and 1.54 g/cm^3 (fig. 55*B*). Compression of sand (ρ_0=1.6 g/cm^3) and alluvium (ρ_0=1.8 g/cm^3) in shock waves to densities of 2.0 g/cm^3 may occur at pressures as low as 25 to 30 kbar. For low density alluvium (ρ_0=1.54 g/cm^3), a shock pressure as low as 10 kbar can result in compression to densities near 2.0 g/cm^3. Compression of dry target material is expected for projectile velocities down to 1 km/s and probably less.

WATER CONTENT

Missile impact craters in water-saturated gypsum lake beds and in moist gypsum lake beds have two features in common. Their ejecta includes little or no sheared or compressed target material and the craters tend to be larger than those in the drier materials (fig. 50). The craters in water-saturated gypsum lake beds (Craters 7 and 44) have displaced masses five to six times larger than the regression line in figure 50; those in moist gypsum lake beds are 1.5 to 2.5 times larger. Hugoniot data suggest that peak shock pressures will be greater (fig. 55) because initial densities (ρ_0=1.98) and water content are greater. Absence of evidence for compressed material must be related to water content and decompression. The large crater sizes may be the result of large transient positive pore pressures, which would reduce the shear stress required for rupture (Hubbert and Rubey, 1959).

A simple analysis will illustrate how positive pore fluid pressures could affect crater size. The shear strength of a soil can be described (Hubbert and Rubey, 1959) by

$$\tau=\pm[\tau_0+(s-p)\tan\phi], \tag{17}$$

where

- τ is the shear stress required for failure,
- τ_0 is the cohesion,
- s is the normal stress,
- p is the pore fluid pressure, and
- ϕ is the angle of internal friction.

When positive pore fluid pressures equal the normal stress across the plane of failure, $\tau=\tau_0$ and the angle of internal friction is effectively zero. The work expended in forming a hemispherical crater (w_s) against the compressive strength, which is twice the shear strength for an angle of internal friction of zero, is

$$w_s=4\pi\int_{r_1}^{r_2}\left[\tau_0+(s-p)\tan\phi\right]r^2dr. \tag{18}$$

Consider the case of the water-saturated target. If τ_0 is taken as 10^7 dynes/cm^2, $s=p$ for a water-saturated condition, and r_2, the final radius of the hemispherical cavity, is 280 cm, then

$$w_s=4\pi\int_0^{2.80}10^7r^2dr=0.92\times10^{15}\text{ ergs.}$$

Consider the case of the dry target. When p is zero, the shear strength is a function of the normal stress and the compressive strength is a function of shear strength and angle of internal friction. Peak shock pressure decay for the Stagecoach cratering experiments in Nevada Test Site alluvium (Sun, 1970, p. 2014) may be expressed by

$$P=4.637\times10^{15}r^{-2.423}, \tag{19}$$

where P is the peak shock pressure and r is the distance from the origin of shock. For the Stagecoach crater with a radius near 1,786 cm and a depth of burst of 1,042 cm (Sun, 1970, table 2), the peak shock pressures decayed to 4.7×10^7 dynes/cm^2 at the crater edge. If peak shock pressures decay to this value at the edge of a hemispherical missile impact crater in alluvium with a radius of 155 cm, the equation for pressure for the missile impact is

$$P=8.7\times10^{12}r^{-2.423}, \tag{20}$$

Where P is considered to represent the maximum principal stress in a Mohr-Coulomb diagram (Hubbert and Rubey, 1959). It can be shown that the normal stress S is approximately $^4/_9$ of the maximum principal stress so that

$$s\approx3.9\times10^{12}r^{-2.423}. \tag{21}$$

When this equation for s is inserted in equation (18),

$$w_s=\frac{4\pi}{\tan\phi}\int_0^r(\tau_0+3.9\times10^{12}\tan\phi\ r^{-2.423})\ r^2dr$$

$$=18\left[\frac{10^7r^3}{3}+\frac{2.7\times10^{12}r^{0.577}}{0.577}\right]_0^{155}$$

$$=1.8\times10^{15}\text{ ergs.}$$

These calculations indicate that twice as much energy is expended in forming a hemispherical crater in dry alluvium with a cohesion of 10^7 dynes/cm^2 as in forming a hemispherical crater in water-saturated material, sixtimes larger, and with the same cohesion. The larger value for the crater in alluvium might be too large because positive pore pressures due to air have been neglected. In any event, the difference can be accounted for semiquantitatively using the Mohr-Coulomb failure criteria and effects of pore pressures.

EXTRAPOLATION TO LARGER SIZES

Extrapolation of the equations representing the relations between dimensions of the missile impact craters and kinetic energies (see table 2, fig. 56) to impact

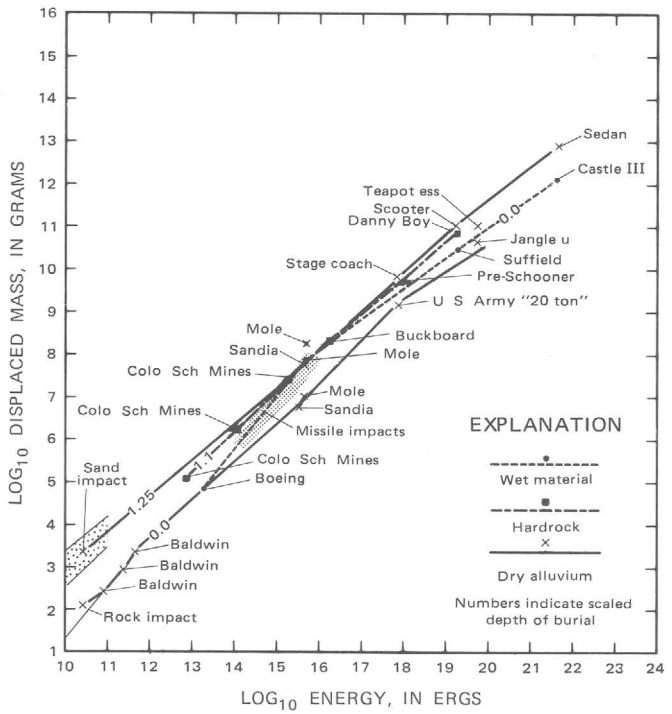

FIGURE 56.—Comparison of data on craters produced by chemical and nuclear explosives (after Robertson, 1966) and experimental impact craters. Data on impact craters in sand from Oberbeck (1970). Data on impact craters in rock from Moore, Gault, and Heitowit (1965).

energies greater than 10^{16} ergs is probably not valid. Large volumes of rock are commonly, if not always, fractured and jointed (see for example, Hubbert and Willis, 1957, p. 159–160) such that on a grand scale the rocks are made up of cohesionless angular blocks. Displaced masses and energies of explosive craters, which compare well with missile impact energies in the region of 10^{15} ergs (fig. 56), yield no indication that such an extrapolation would be valid. Large explosive craters in very cohesive, but jointed and fractured basalt suggest scaling laws change above 10^{15} ergs (Nordyke and Wray, 1964).

The data on these missile impact craters may lie in a transitional region where scaling laws change. The relations between displaced masses and energies for impact craters in sand (Oberbeck, 1970) and rock (Moore, and others, 1964) intersects near 10^{15} ergs of kinetic energy. Extrapolation of equations for craters in sand (Oberbeck, 1970) to kinetic energies of 10^{20} ergs yield displaced masses of $10^{11.52}$ and $10^{11.34}$ grams, which lie within the bounds drawn for alluvium (fig. 56). Extrapolation using equations for small impact craters in rock and missile impacts fails to predict displaced masses of large explosive craters in alluvium with small scaled depths of burial. Apparently cohesion and strength of rocks become less important for large cratering events (Gault and Moore, 1965), because the pervasive fractures and joints in rocks make them behave more like cohesionless materials. Despite unknowns and discrepancies between individual sets of data, cratering experiments using chemical and nuclear explosives provide the data for best estimates of energies of large natural hypervelocity objects producing large impact craters on the Earth and Moon (Shoemaker, 1960, p. 431; Baldwin, 1963, ch. 7).

APPLICATIONS TO LUNAR PROBLEMS

Data collected during the study of missile impact craters apply to a number of problems of lunar studies: (1) the nature of the lunar surface materials (Moore, 1966b, 1968b), (2) sizes and morphologies of craters produced by the impact of Ranger spacecraft (Moore, 1968a) and other vehicles (Latham and others, 1970), (3) the explanation of certain features imaged by Surveyor (Shoemaker, Morris, and others, 1969), (4) support for the Apollo passive seismic experiment (Latham and others, 1970), (5) interpretation of craters seen in Apollo orbital photographs (Moore, 1971b, 1972), (6) training of astronauts, and (7) properties of returned lunar samples.

NATURE OF LUNAR SURFACE

The use of crater morphology to assess the nature of lunar surface materials using missile impact data and other data on explosive craters requires that: (1) the craters employed be produced by impact, (2) the existence and nature of crater erosion be recognized, (3) the relation between crater morphology and crater size be understood, and (4) the resolution and angle of illumination of the photographs be taken into account. The first requirement was justified for small craters, as meteors and meteoroids are known to bombard the Moon. The second requirement was fulfilled when erosion of lunar craters by micrometeors and meteors was postulated (Moore, 1964), then substantiated by Ranger images (Trask, 1966) and subsequent photography (Soderblom, 1970). Such an interpretation of the erosional process requires that only fresh, or eumorphic, craters with maximum relief be used to appraise the mechanical properties, because floors, blocks, and rims of the older craters are partly filled, degraded, and subdued. The third requirement has been established by experimentation and observation. Craters in rock several metres in diameter tend to be rimless, whereas those in cohesionless sand have raised rims. Craters near 30 m across have rims regardless of the material (see for example, Spruill and Paul, 1965). Ejecta of 30-m craters in rock contain a great number of blocks up to about 1 m across; craters in sand contain no blocks. Large craters in rock have both raised rims and large blocks in the ejecta (Spruill and Paul, 1965; Boutwell,

1928). The last requirement, resolution, is illustrated in figure 57 by a 33-m and a 10-m crater produced by chemical explosives in dense basalt flows at the Nevada Test Site (Vortman and others, 1960, Shot 11). When the resolution is 22 cm (fig. 57*A*), a great number of blocks are visible in and around both the large and small craters. When the resolution is 85 cm (fig. 57*B*), a few large blocks are visible and smaller ones appear as lumps.

When the requirements given are taken into account, an assessment of the surface and subsurface peoperties can be made. For example, the highest resolution (26 cm) images of Ranger IX (fig. 58) clearly show craters down to a metre in size. On the images, fresh craters down to 1 m across have continuous raised rims and large depth-to-diameter ratios characteristic of soillike materials with low cohesions and densities near 1.6 g/cm^3. Larger fresh craters do not contain blocks, nor is the surface near the crater littered with many blocks larger than 26 cm. The near-surface materials imaged by Ranger IX are soillike with a grain size substantially less than 26 cm. Slopes of small crater walls are from 32° to 38° (Choate, 1966), implying that the angle of internal friction is near that for cohesionless terrestrial soils.

RANGER AND OTHER IMPACTS

Predictions of the sizes of the craters produced by the impacts of Ranger spacecraft, SIVB stages of Apollo, and Lunar Module Ascent Stages were made using missile impact data. Craters produced by the impact of Ranger spacecraft were estimated to be 12.2 ± 3 m (letter to I. G. Recant and T. P. Hansen, Lunar Orbiter Project Office, Dec. 10, 1965), craters produced by the impact of SIVB stages of Apollo, 57 ± 17 m, Ascent stage craters, 4 ± 2 m across (Latham and others, 1970). Craters produced by Ranger spacecraft (fig. 59) turned out to be near 13 to 15 m (Whitaker, 1972 ; Moore, 1972), SIVB impact craters near 40 m across (Whitaker, 1972). An overestimate of the size of SIVB craters may have resulted from not taking into account the bulk density of the SIVB, which was very low (for effect of projectile density, see Moore and others, 1965; Birkhoff and others, 1948). The small crater size predicted for the impact of the Ascent Stages, when compared with the size predicted by Whitaker (1972), result from the small angle of impact, an effect Whitaker neglected.

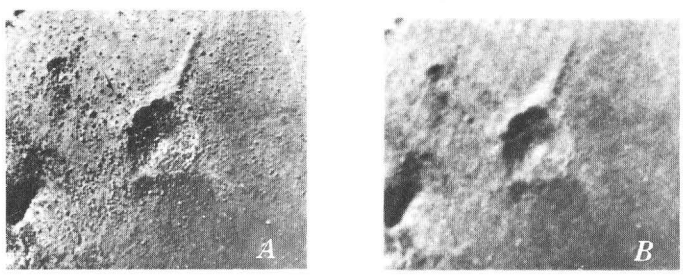

FIGURE 57.—Effect of resolution on appearance of craters formed in rock. Large crater in center about 33 m across, small one at lower left is about 10 m across. *A*, Identification resolution near 22 cm. *B*, Identification resolution near 85 cm.

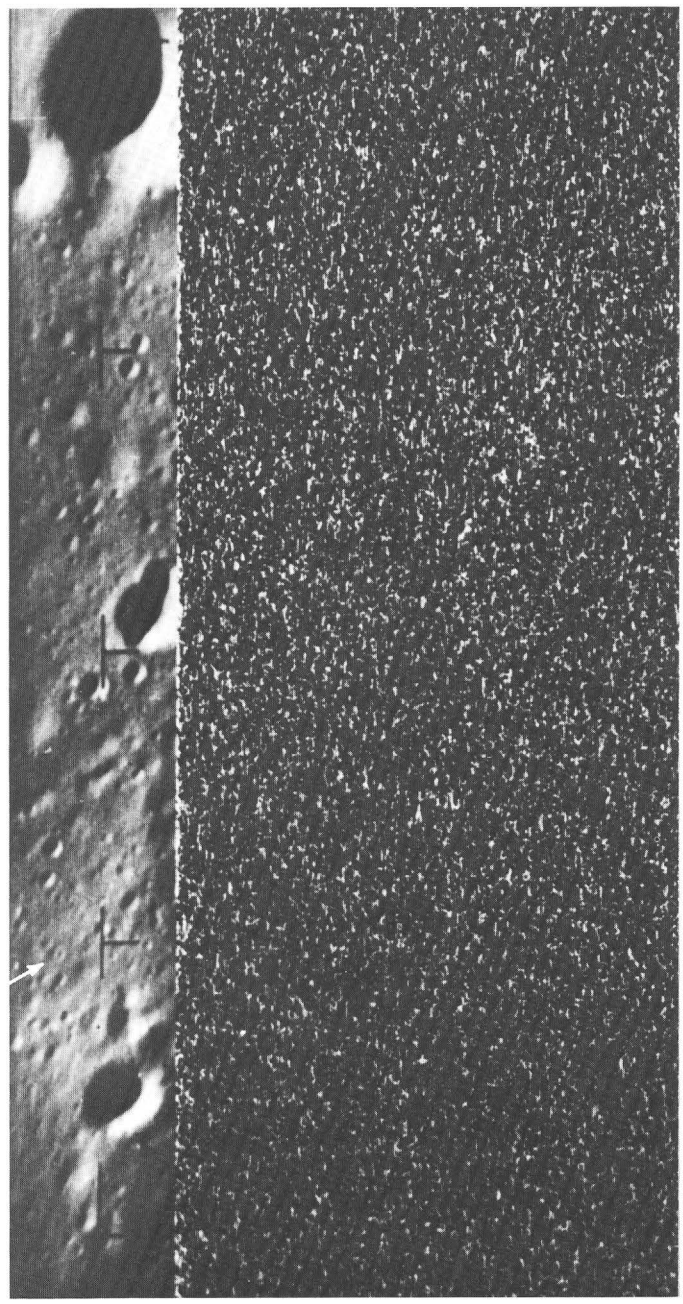

FIGURE 58.—Last B-camera frame of Ranger IX (B–88) showing rimmed fresh craters down to 1 m across with raised rims. Distance between reticles about 40 m; identification resolution near 26 cm. Arrow indicates 1-m, fresh-rimmed crater indicating low cohesion of surface material. Note general absence of large blocks around larger craters, indicating materials are unlike dense basalt flows.

SURVEYOR IMAGES

Data on phenomena associated with missile impacts have been used to account for observations made using

Surveyor images, in particular interpretations of fresh craters and their ejecta were used to assess the nature of surface and near-surface materials at the Surveyor I Landing site (Rennilson and others, 1966). For Surveyors VI and VII (Shoemaker, Morris, and others, 1969), low-velocity secondary impacts were identified by analogy with similar features around missile impact craters (compare fig. 60 with figs. 18 and 22).

PASSIVE SEISMIC EXPERIMENT

Data on amplitudes of the initial seismic signal produced by missile impacts were a useful guide for predicting amplitudes of initial seismic signals (P-wave) produced by impact on the lunar surface. The lack of similarity of subsequent seismic signals points up the large differences between the structure of terrestrial and lunar rocks (Latham and others, 1970).

APOLLO ORBITAL PHOTOGRAPHS

A number of lunar craters photographed from orbit by the Apollo missions to the Moon are similar to missile impact craters in their morphologies but larger. Some of these lunar craters exhibit striking bilateral symmetry similar to that of Crater 7 (Moore, 1971a, fig. 2–34); others yield evidence for inverted stratigraphy (Moore, 1971b, fig. 2–31). One crater photographed by Apollo 16 is quite similar to missile impact craters in that little or no ejecta is found on the up-trajectory side of the crater while lighter ejecta, including large blocks, is found in lateral and down-trajectory directions (fig. 61). Data on missile impact craters in cohesive targets has contributed to establishing an empirical relation between diameters of largest blocks ejected from craters and crater diameters (Moore, 1971b, 1972).

ASTRONAUT TRAINING

The principal use of missile impact craters in the training of astronauts was to establish in their minds how lunar impact craters could be used to obtain samples from beneath the lunar regolith and to train them to recognize features that were expected in small lunar craters. Impact craters are natural drill holes in the local materials, and samples from beneath the surface can be collected on their rims and flanks (see Shoemaker, 1960). Samples from rims of progressively larger craters yield samples from progressively greater depths. This principle was employed on all Apollo missions. For example, some of the fragments collected at the Apollo 11 site were derived from West crater (180 m diameter), 400 m east of the Apollo 11 site (Shoemaker, Bailey, and others, 1969); Apollo 12 astronauts made a conscious effort to examine craters of various sizes (Shoemaker and others, 1970); and collection of samples from large craters 340 to 900 m across were

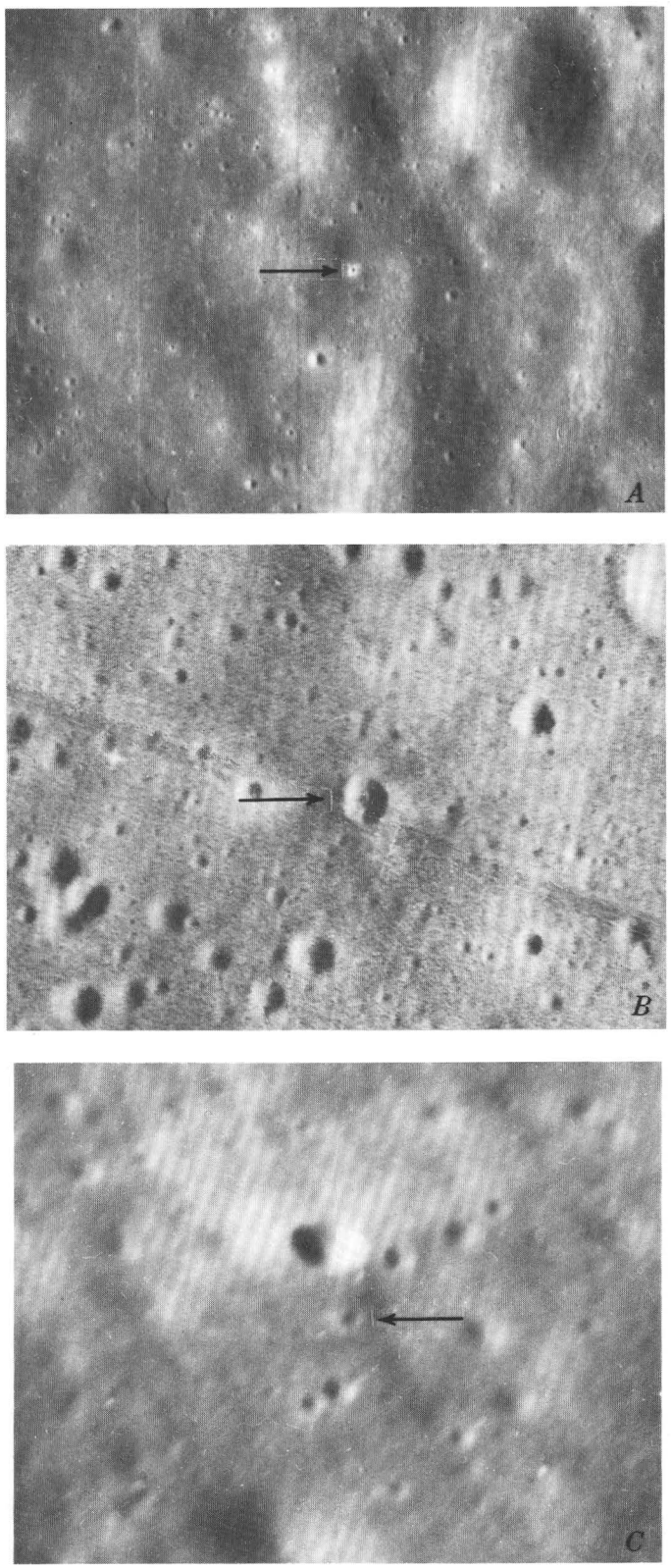

FIGURE 59.—Craters produced by Ranger impacts. *A*, Impact crater made by Ranger VII. Crater near 14 m across (Apollo 16 Panoramic Camera frame 5420). *B*, Impact crater made by Ranger VIII (Lunar Orbiter II, photograph H 70, framelets 601 and 602). Crater is 13.8 by 13 m. *C*, Impact crater made by Ranger IX. Crater near 14 m across. (Apollo 16 Panoramic Camera frame 4658.)

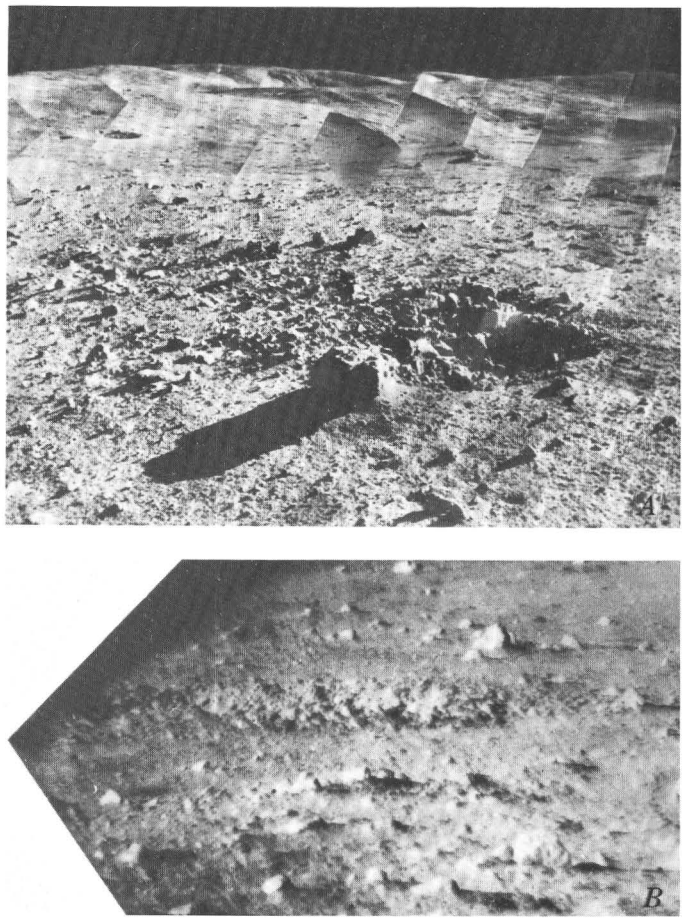

FIGURE 60.—*A*, Secondary impact crater about 3 m in diameter near Surveyor VII (compare with fig. 22). Projectile smaller than crater it produced. *B*, Secondary impact crater on lunar surface near Surveyor I for which projectile fills crater (compare with fig. 18).

prime goals for Apollo 14 and 16 astronauts (Swann and others, 1971; Muehlberger and others, 1972).

The nature of asymmetry of craters and ejecta was also used to help identify secondary craters.

LUNAR SAMPLES

Ejecta from missile impact craters is similar to ejecta from lunar craters. In particular, undeformed blocks and fragments of ejecta occur along with sheared and compressed fragments with grooves and striations as well as rocks with coated surfaces (fig. 62). Sample 14047 (fig. 62*A*) is an example of sheared lunar regolith material collected from the west rim of a sharp 5-m-diameter crater at station B of the Apollo 14 site. This sample was a clod of regolith material partly bounded by planar surfaces that were grooved and striated (Swann and others, 1971, p. 74–75) like fragments in the ejecta from missile impact craters (fig. 25). The planar surfaces of 14047 (Swann and others, 1971, p. 75, fig. 3–35) are similar to some fragments in the ejecta from missile impacts, units bounded by fractures in shattered and fractured material (fig. 14), and units bounded by fractures in the zone of conjugate fractures (fig. 31).

Many fragments collected on the Moon have surfaces coated with glass and pulverized, partly melted debris like material collected at the Apollo 17 (Apollo Lunar Geology Investigation Team, 1973, p. 63; fig. 62*B*) and 14 sites (Swann and others, 1971; fig. 62*C*). Many of these coatings have been injected along fractures (fig. 62*B,C*) and contain metal particles in glass (Wosinski and others, 1972; fig. 62*C*). Similar coatings are found on fragments of sheared surfaces of compressed target material (fig. 25), along some conjugate fractures (fig. 14), to a lesser extent on tensile fractures normal to grooved and striated surfaces. Much of the coating on fragments from missile impact craters is powdered and disaggregated projectile material but it is also, in part, fused metal and vesiculated material from the missile. Impact cratering accounts for the coated rocks on the lunar surface, especially those concentrated on the flanks of small craters.

Injections of clastic debris along fractures are found in lunar samples (Wilshire and others, 1973). In one such rock, shown in figure 62, mobilized white clastic debris fills fractures within shattered darker gray rock; in some respects similar to the cataclastic injection in rocks shown in figure 29.

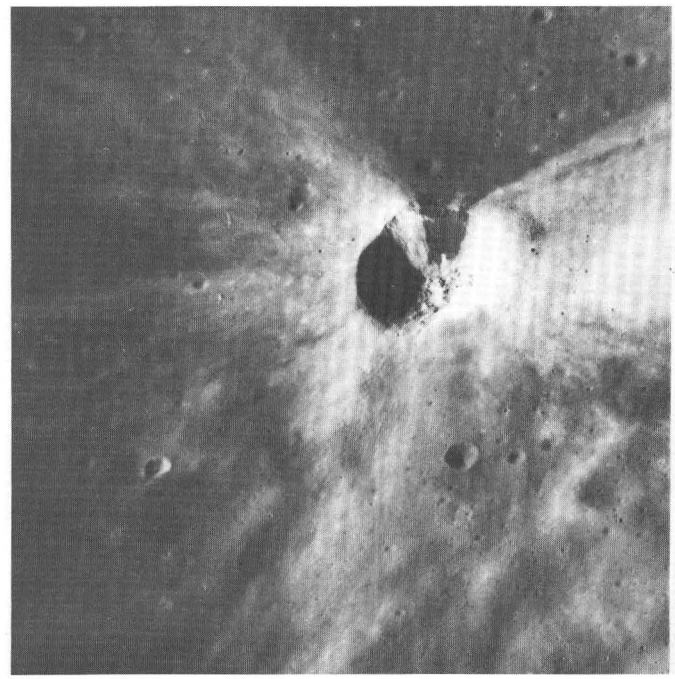

FIGURE 61.—Apollo 16 Panoramic Camera photograph showing oblique view of 2-km-diameter crater. South is toward top of picture. Note asymmetrical ejecta, exposures, and talus of dark material on up-trajectory wall, and large blocks on lateral and down-trajectory flanks (AS–16 Panoramic Camera frame 4511).

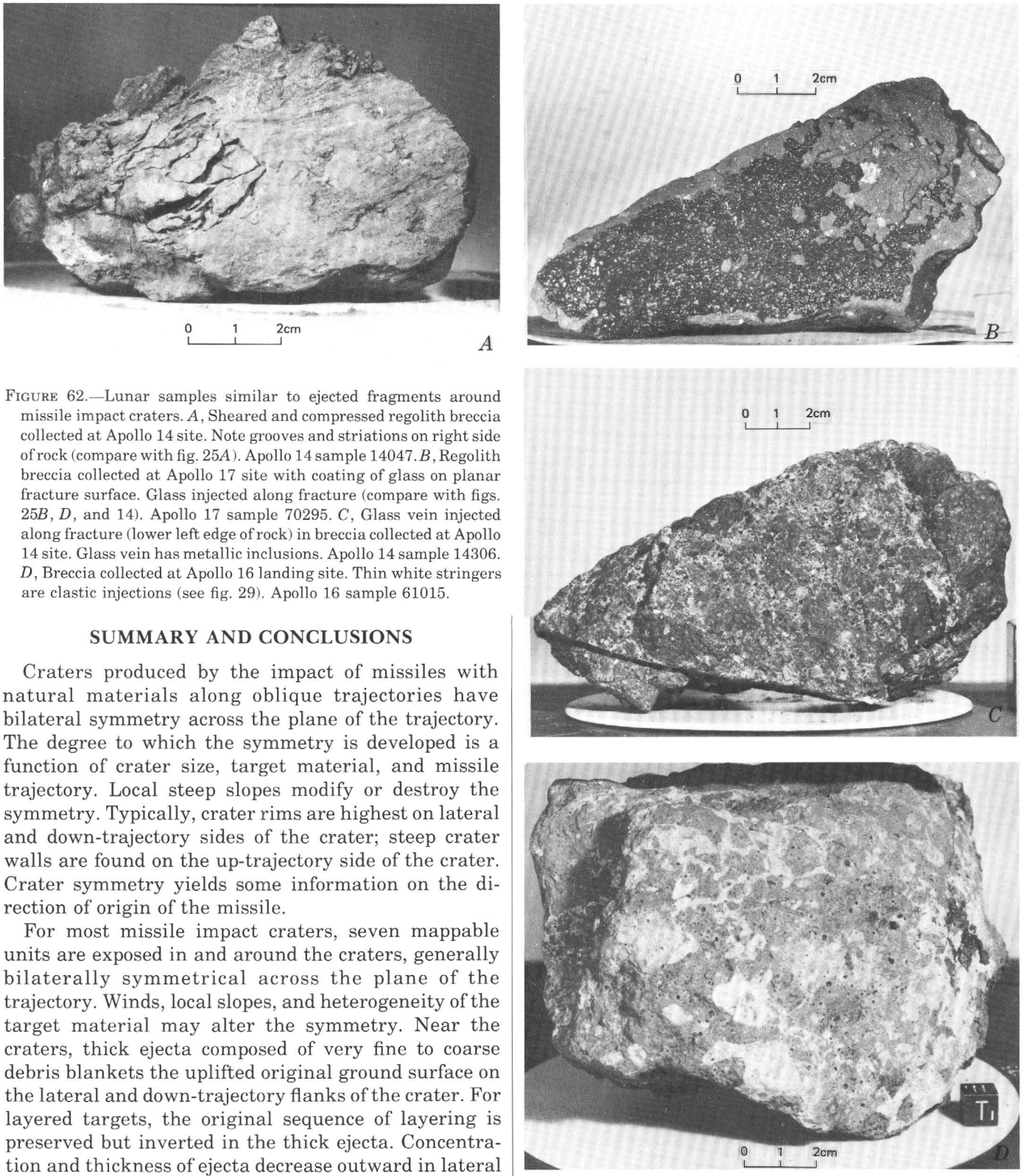

FIGURE 62.—Lunar samples similar to ejected fragments around missile impact craters. *A*, Sheared and compressed regolith breccia collected at Apollo 14 site. Note grooves and striations on right side of rock (compare with fig. 25*A*). Apollo 14 sample 14047. *B*, Regolith breccia collected at Apollo 17 site with coating of glass on planar fracture surface. Glass injected along fracture (compare with figs. 25*B*, *D*, and 14). Apollo 17 sample 70295. *C*, Glass vein injected along fracture (lower left edge of rock) in breccia collected at Apollo 14 site. Glass vein has metallic inclusions. Apollo 14 sample 14306. *D*, Breccia collected at Apollo 16 landing site. Thin white stringers are clastic injections (see fig. 29). Apollo 16 sample 61015.

SUMMARY AND CONCLUSIONS

Craters produced by the impact of missiles with natural materials along oblique trajectories have bilateral symmetry across the plane of the trajectory. The degree to which the symmetry is developed is a function of crater size, target material, and missile trajectory. Local steep slopes modify or destroy the symmetry. Typically, crater rims are highest on lateral and down-trajectory sides of the crater; steep crater walls are found on the up-trajectory side of the crater. Crater symmetry yields some information on the direction of origin of the missile.

For most missile impact craters, seven mappable units are exposed in and around the craters, generally bilaterally symmetrical across the plane of the trajectory. Winds, local slopes, and heterogeneity of the target material may alter the symmetry. Near the craters, thick ejecta composed of very fine to coarse debris blankets the uplifted original ground surface on the lateral and down-trajectory flanks of the crater. For layered targets, the original sequence of layering is preserved but inverted in the thick ejecta. Concentration and thickness of ejecta decrease outward in lateral and down-trajectory directions, becoming thin to discontinuous and then scattered. Up-trajectory, ejecta is usually absent, thin to discontinuous, or scattered on the surface, but it may be thick in some cases. Some fragments are ejected as far as 330 m from the crater. Within the crater, slope material composed

of talus and fallback partly cover crater walls and cover crater floors. Locally, tilted and broken target material may be exposed in upper crater walls on the lateral and down-trajectory sides of the crater. For most craters, shattered and fractured target material is exposed on the up-trajectory crater wall and open fractures concentric to the crater edge are exposed on the level or even downwarped up-trajectory flank.

Most of the ejecta are fragments of target material, disaggregated target material, and crushed target material. The larger fragments are relatively undeformed. For porous targets, significant amounts of the ejected fragments have been deformed by shearing and compression of the target material. Some sheared and compressed fragments have surfaces coated with a dark mixture of fragmented, powdered, and partly fused missile.

When the surface materials around missile impact craters have low cohesion and large fragments are ejected from the crater, a great number of secondary impact craters are produced. The distribution of the secondary impacts has bilateral symmetry when the surrounding surface is uniform. A continuous spectrum of secondary craters is produced. Near the crater ejected fragments may be larger than the crater they produce or about the same size. Farther from the crater, secondary fragments deform, break up, and partly fill secondary craters that are larger than the fragment. At greater distances, secondary fragments are smaller than the craters they produce and are completely ejected from the crater.

Subsurface deformation of the target material is complex. A breccia composed of a mixture of fragmented and powdered missile and sheared and compressed target material underlies the crater floor. For craters in fixed gypsum dunes, a sanded zone with flow banding surrounds the mixed breccia on the down-trajectory and lateral sides of the breccia. Cataclastic injections of mixed projectile pieces and target material from the mixed breccia penetrate into the sanded zone. In alluvium, a breccia with no missile pieces surrounds the mixed breccia. A zone of conjugate fractures surrounds the central breccias and sanded material. Near the surface beneath the down-trajectory and lateral flanks of the crater, the target material is tilted upward and broken. Beneath the up-trajectory flank, open fractures are found. In the ejecta, fragments are found that have the same properties as the fragments in the subsurface deformation zones. For layered targets, materials from lower layers are displaced upward in the mixed breccia and rather complex folding may occur beneath the crater rim.

Missile or projectile behavior and deformation during impact is chiefly a function of target material and projectile velocity although there are other variables. At low velocities, projectiles are slightly deformed, whereas at velocities exceeding 3.9 km/s, they are fragmented into very small pieces, powdered, and fused. Where targets are porous, the missile or fragmented missile tends to remain completely or partly below the surface, particularly at the lower velocities; where dense and coherent, the missile or pieces of it tend to remain above the surface as ejecta.

Linear dimensions of the missile impact craters are proportional to the 0.412 to 0.445 power, while displaced masses are proportional to the 1.205 to 1.298th power of kinetic energy. Extrapolation of data on displaced masses and energies of hypervelocity impact craters in rock and sand converge and intersect the missile impact data at kinetic energies near 10^{15} to 10^{16} ergs.

There are a number of parallels between craters produced by chemical explosives and missile impacs: (a) they are about the same size when the scaled depth of burst of the explosive is small and the TNT energy of the explosive is equivalent to the kinetic energy of the missile; (b) craters produced in water-saturated targets are larger than their dry counterparts; (c) their size is dependent on target material; (d) both types of craters commonly have mixed breccia beneath their floors; (e) both have sheared and compressed target material in their ejecta when the target is porous; (f) they have similar fracture patterns and deformations; and (g) the original stratigraphy or sequence of layering is preserved overturned in the ejecta near the flank and rim.

Some problems concerning impact craters are unresolved: (a) the effect of impact angle on the size of the crater is not clear and may vary with target and projectile properties; (b) the equivalent scaled depth of burst of an impact event clearly varies with projectile and target properties in a manner not entirely understood; (c) energy and velocity thresholds for cratering are not clearly defined; and (d) the relation between crater size and missile properties is not entirely resolved because of the large number of variables in target material and projectile conditions at impact.

Compression of porous target materials is expected, as some missile velocities are sufficient to produce shock pressures of several hundred kilobars, and experimental data on shock-wave compression of porous materials indicate significant compression may occur at pressures near 5 to 10 kbar and greater. The large size of craters in water-saturated targets probably results from low effective target strengths produced by positive pore pressures during shock compression of the target.

Data on craters produced by chemical and nuclear explosives with shallow depths of burial provide the basis for best estimates of energies of large natural hypervelocity impact craters.

The study of craters produced by missile impacts has contributed to lunar science in many ways: (a) the character of their ejecta and shape was used to assess some of the properties of lunar surface materials; (b) they were used to predict sizes of craters produced by artificial impact on the Moon; (c) certain features photographed by Surveyors were found to be consistent with similar features around missile impact craters, (d) missile impacts were used to help calibrate the Apollo Passive Seismic Experiment, (e) many craters seen in Apollo orbital photographs were found to be morphologically and geologically similar to missile impact craters, (f) data on missile impact craters and their ejecta were used to help train astronauts in recognizing certain features of lunar craters and in collecting samples; and (g) fragments ejected from missile impact craters were found to have properties similar to fragments collected on the lunar surface.

REFERENCES CITED

Allsman, P. L., 1960, Analysis of explosive action in breaking rock: Am. Inst. Mining Metall. Petroleum Engineers Trans., v. 217, p. 469–478.

Apollo Lunar Geology Investigation Team, 1973, Documentation and environment of the Apollo 17 samples, a preliminary report: U.S. Geol. Survey Interagency Rept., Astrogeology 71, 322 p., 5 pl.

Baldwin, R. B., 1949, The face of the Moon: Chicago, Univ. Chicago Press, 239 p.

———1963, The measure of the Moon: Chicago, Univ. Chicago Press, 488 p.

Bass, R. C., Hawk, H. L., and Chabai, A. J., 1963, Hugoniot data for some geologic materials: Sandia Corp. Rept. SC–4903 (RP), 18 p.

Birkhoff, Garrett, MacDougal, D. P., Pugh, E. M., Taylor, Sir Geoffrey, 1948, Explosives with lined cavities: Jour. Appl. Physics, v. 19, p. 563–582.

Bryan, G. M., 1962, Oblique impact of high velocity steel pellets on lead targets: Symposium on Hypervelocity Impact, 5th, Denver, Colo., Oct. 30–Nov. 1, 1961, Proc., v. 1, pt. 2, p. 511–534.

Boutwell, W. D., 1928, The mysterious tomb of a giant meteorite: Natl. Geog. Mag., v. 53, no. 6, p. 721–730.

Chabai, A. J., 1965, On scaling dimensions of craters produced by buried explosives: Jour. Geophys. Research, v. 70, p. 5075–5098.

Charters, A. C., 1960, High-speed impact: Sci. Am., v. 203, no. 4, p. 128–140.

Charters, A. C., Denardo, B. P., and Rossow, V. J., 1957, Development of a piston-compressor type light-gas gun for the launching of free-flight models at high velocity: Natl. Advisory Comm. Aeronautics Tech. Note, NACA TN 4143, 95 p.

Choate, Raul, 1966, Lunar slope angles and surface roughness from Ranger photographs: California Inst. Technology Jet Propulsion Lab. Tech. Rept. 32-994, p. 411–432.

Colp, J. L., 1968, Terradynamics: A study of projectile penetration of natural earth materials: Sandia Labs, Rept., SC-DR-68-215, 61 p.

Cook, M. A., and Mortensen, K. S., 1967, Impact cratering in granular materials: Jour. Appl. Physics, v. 38, no. 13, p. 5125–5128.

Culp, F. L., and Hooper, H. L., 1961, Study of impact cratering in sand: Jour. Appl. Physics, v. 32, p. 2480.

Curtis, J. S., 1962, An accelerated reservoir light-gas gun: Natl. Aeronautics and Space Adm. Tech. Note, NASA TN D-1144, 22 p.

Duvall, W. I., and Atchison, T. C., 1957, Rock breakage by explosives: U.S. Bur. Mines Rept. Inv. 5356, 52 p.

Fullmer, C. V., 1966, Cratering characteristics of wet and dry sand: Boeing Co. Rept. D-2-90683-1, 98 p.

Gault, D. E., and Heitowit, E. D., 1963, The partition of energy for hypervelocity impact craters formed in rock: Symposium on Hypervelocity Impact, 6th, Cleveland, Ohio, Apr. 30–May 2, 1963, Proc., v. 2, pt. 2, p. 419–456.

Gault, D. E., and Moore, H. J., 1964, Scaling relationships for microscale impact craters: Hypervelocity Impact Symposium, 7th, Tampa, Fla., Nov. 17–19, 1964, Proc., v. 6, p. 341-351.

Gault, D. E., Quaide, W. L., and Oberbeck, V. R., 1965, Interpreting Ranger photographs from impact cratering studies, *in* Hess, W. N., Menzel, D. H., and O'Keefe, J. A., eds., The nature of the lunar surface, *in* Proceedings 1965 IAU-NASA Symposium, Goddard Space Flight Center, Greenbelt, Md., April 15-16, 1965: Baltimore, Md., John Hopkins Press, p. 125–140.

Gault, D. E., Quaide, W. L., Oberbeck, V. R., and Moore, H. J., 1966, Luna 9 photographs—Evidence for a fragmental surface layer: Science, v. 153, p. 985–988.

Gault, D. E., Shoemaker, E. M., and Moore, H. J., 1963, Spray ejected from the lunar surface by meteoroid impact: Natl. Aeronautics and Space Admin. Tech. Note, NASA TN-D-1767, 39 p.

Gilbert, G. K., 1893, The Moon's face, a study of the origin of its features: Philos. Soc. Washington [D.C.] Bull. 12, p. 241–292.

Hartman, H. L., 1959, Basic studies of percussion drilling: Mining Eng., v. 11, no. 1, p. 68–75.

———1962, Crater geometry relations in percussive drilling-single blow studies: Mine and Quarry Eng., v. 28, p. 530–536.

Herr, R. W., 1971, Effects of the atmospheric-lithostatic pressure ratio on explosive craters in dry soil: Natl. Aeronautics and Space Admin. Tech. Rept., NASA TR-R-366, 88 p.

Hooke, Robert, 1664, Micrographia or some physiological descriptions of minute bodies made by magnifying glasses with observations and inquiries thereupon: reprinted New York, Dover Publ. Inc., 1964, 273 p.

Hörz, Freidrich, 1969, Structural and mineralogical evaluation of an experimentally produced crater in granite: Contr. Mineralogy and Petrology, v. 21, p. 365–377.

Hubbert, M. K., and Rubey, W. W., 1959, Role of fluid pressure in mechanics of fluid-filled porous solids and its application to overthrust faulting: Geol. Soc. America Bull., v. 70, p. 115–166.

Hubbert, M. K., and Willis, D. G., 1957, Mechanics of hydraulic fracturing: Am. Inst. Mining Metall. Petroleum Engineers, v. 210, p. 153–166.

Ives, H. E., 1919, Some large-scale experiments imitating the craters of the moon: Astrophys. Jour., v. 50, p. 245–250.

Johnson, J. B., 1962, Small-scale blasting in mortar: U.S. Bur. Mines Rept. Inv. 6012, 22 p.

Latham, G. V., McDonald, W. G., and Moore, H. J., 1970, Missile impacts as sources of seismic energy on the Moon: Science, v. 168, p. 242–245.

Livingston, C. W. and Smith F. L., 1951, Bomb penetration project: Colorado School of Mines Research Foundation, Inc., CSM-280-51-5 (Available from Document Service Center, Armed Services Tech. Inf. Agency, U.B.B., Dayton, Ohio; A.S.T.I. 183749, reel C–6953), 245 p.

Mandeville, J. C. and Vedder, J. F., 1971, Microcraters formed in glass by low denisty projectiles: Earth and Planetary Sci. Letters, v. 11, p. 297–306.

Meydenbauer, A., 1882, Die Gebilde der Mondoberfläche: Sirius, v. 15, p. 59–64.

Moore, H. J., 1964, Density of small craters on the lunar surface, *in* Pt. D:Studies for space flight program, Astrogeol. Studies Ann. Prog.

Rept., Aug. 24, 1962–July 1, 1963: U.S. Geol. Survey open-file report, p. 34-51.

———1966a, Craters produced by missile impacts, *in* Crater Investigations, Pt. B., Astrogeol. Studies Ann. Prog. Rept. July 1, 1965, to July 1, 1966: U.S. Geol. Survey open-file report, p. 79–105.

———1966b, Interpretation of small lunar craters, *in* Space Flight Investigations, Pt. D, Astrogeol. Studies Ann. Prog. Report, July 1, 1965 to July 1, 1966: U.S. Geol. Survey open-file report, p. 43–69.

———1966c, Cohesion of material on the lunar surface, *in* Ranger VIII and IX, Part II: Experimenters' analyses and interpretations: California Inst. Technology Jet Propulsion Lab. Tech. Rept. 32-800, p. 263–270.

———1968a, Ranger VIII and gravity scaling of lunar craters: Science, v. 159, p. 333–334.

———1968b, Impact craters and the lunar surface [abs.]: Internatl. Geol. Cong., 23d, Prague 1968, Repts., Abs., p. 345.

———1969, Subsurface deformation resulting from missile impact, *in* Geological Survey research 1969: U.S. Geol. Survey Prof. Paper 650–B, p. B107–B112.

———1971a, Craters produced by missile impacts: Jour. Geophys. Research, v. 76, no. 23, p. 5750–5755.

———1971b, Lunar impact crater, *in* Analysis of Apollo 10 photography and visual observations: Natl. Aeronautics and Space Admin. Spec. Publ. NASA SP-232, p. 24–26.

———1972, Ranger and other impact craters photographed by Apollo 16, *in* Apollo 16 Preliminary Science Report, Part J: Natl. Aeronautics and Space Admin. Spec. Publ. NASA SP-315, p. 29–45 to 29–51.

Moore, H. J., Cummings, David, and Gault, D. E., 1967, Use of infrared imagery and color photography in study of missile impact craters: Natl. Aeronautics and Space Admin., Earth Resources Surv. Prog., Tech. Letter NASA-75, 6 p.

Moore, H. J., Gault, D. E., and Heitowit, E. D., 1965, Change of effective target strength with increasing size of hypervelocity impact craters: Hypervelocity Impact Symposium, 7th, Tampa, Fla., Nov. 17–19, 1964, Proc., v. 4, Theorys, p. 35–45.

Moore, H. J., Gault, D. E., Heitowit, E. D., and Lugn, R. V., 1964b, Hypervelocity impact craters in porous cohesive targets, *in* Astrogeol. Studies Ann. Prog. Rept., July 1, 1963, to July 1, 1964: U.S. Geol. Survey open-file report, p. 93–143.

Moore, H. J., Kachadoorian, Reuben, and Wilshire, H. G., 1964a, A preliminary study of craters produced by missile impacts, *in* Crater investigations, pt. B, Astrogeol. Studies Ann. Prog. Rept., July 1, 1963 to July 1, 1964: U.S. Geol. Survey open-file report, p. 58-92.

Moore, H. J., Kachadoorian, Reuben, and McCauley, J. F., 1968, Imagery of craters produced by missile impacts: Natl. Aeronautics and Space Admin. Tech. Letter NASA-103, 38 p.

Moore, H. J. and Lugn, R. V., 1965, A missile impact in water-saturated sediments, *in* Crater Investigation, pt. B., Astrogeol. Studies Ann. Prog. Rept., July 1, 1964 to July 1, 1965: U.S. Geol. Survey open-file report, p. 101–126.

Moore, H. J., Lugn, R. V., and Gault, D. E., 1962, Experimental hypervelocity impact craters in rock: Symposium on Hypervelocity Impact, 5th, Denver Colo., Oct. 30-Nov. 1, 1961, Proc., v. 1, pt. 2, p. 625–643.

Moore, H. J. and Robertson, F. G., 1966, Hypervelocity impact craters in pumice, *in* Crater Investigations, pt. B, Astrogeol. Studies Ann. Prog. Report, July 1, 1965 to July 1, 1966: U.S. Geol. Survey open-file report, p. 107–125.

Mortensen, K. S., 1967, A fundamental study of cratering in granular materials with an application to lunar craters, University of Utah, Salt Lake City, Utah, Ph.D. thesis: Ann Arbor, Mich., University Microfilms, 132 p.

Muehlberger, W. R., Batson, R. M., Boudette, E. L., and others, 1972, Apollo 16 Preliminary Science Report: Natl. Aeronautics and Space Admin. Spec. Publ. NASA SP-315, p. 6–1 to 6–81.

Nordyke, M. D., 1961, Nuclear craters and preliminary theory of the mechanics of explosive crater formation: Jour. Geophys. Research, v. 66, p. 3439–3459.

———1962, An analysis of cratering data from desert alluvium: Jour. Geophys. Research, v. 67, p. 1965–1974.

Nordyke, M. D., and Wray, W., 1964, Cratering and radioactivity results from a nuclear cratering detonation in basalt: Jour. Geophys. Research, v. 69, p. 675–689.

Oberbeck, V. R., 1970, Laboratory simulation of impact cratering with high explosives: Natl. Aeronautics and Space Admin. TMX-62010, 41 p.

———1971 Laboratory simulation of impact cratering with high explosives: Jour. Geophys. Research, v. 76, p. 5732–5749.

Partridge, W. S., and Van Fleet, H. B., 1958, Similarities between lunar and high-velocity impact craters: Astrophys. Jour., v. 128, p. 416–419.

Rennilson, J. J., Dragg, J. L., Morris, E. C., Shoemaker, E. M., and Turkevich, A., 1966, Lunar surface topography, *in* Surveyor I mission report, Part II, Scientific data and results: California Inst. Technology Jet Propulsion Lab. Tech. Rept. 32-1023, p. 7–44.

Robertson, F. G., 1966, Compilation of data on craters produced by explosives, *in* Crater Investigations, pt. B., Astrogeol. Studies Ann. Prog. Rept., July 1, 1965 to July 1, 1966: U.S. Geol. Survey open-file report, p. 127–134.

Shoemaker, E. M., 1960, Penetration mechanics of high velocity meteorites, illustrated by Meteor Crater, Arizona: Internat. Geol. Cong., 21st, Norden 1960, Rept., pt. 18, p. 418–434.

———1962, Interpretation of lunar craters, chap. 8, *in* Kopal, Zdnenêk, ed., Physics and astronomy of the Moon, New York and London, Academic Press, 538 p.

Shoemaker, E. M., Bailey, N. G., Batson, R. M., and others, 1969, Geologic setting of the lunar samples returned by the Apollo 11 mission, *in* Apollo 11 Preliminary Science Report: Natl. Aeronautics and Space Admin. Spec. Publ. NASA SP-214, p. 41–83.

Shoemaker, E. M., Batson, R. M., Bean, A. L., and others, 1970, Preliminary geologic investigation of the Apollo 12 landing site, *in* Apollo 12 Preliminary Sci. Report: Natl. Aeronautics and Space Admin. Spec. Publ. NASA-SP-235, p. 113–161.

Shoemaker, E. M., Gault, D. E., Moore, H. J., and Lugn, R. V., 1963, Hypervelocity impact of steel into Coconino Sandstone: Am. Jour. Science, v. 261, p. 668–682.

Shoemaker, E. M., Morris, E. C., Batson, R. M., Holt, H. E., Larson, K. B., Montgomery, D. R., Rennilson, J. J., and Whitaker, E. A., 1969, Television observations from Surveyor, *in* Surveyor Program Results: Natl. Aeronautics and Space Admin. Spec. Publ. NASA SP-184, p. 19–128.

Soderblom, L. A., 1970, A model for small-impact erosion applied to the lunar surface: Jour. Geophys. Research, v. 75, p. 2655–2661.

Spruill, J. L., and Paul, R. A., 1965, Crater measurements—Project pre-Schooner: U.S. Army Corps Engineers Nuclear Cratering Group, Plowshare, Final Rept., PNE 502 F, 134 p.

Sun, James M. S., 1970, Energy counter-pressure scaling equations of linear crater dimensions: Jour. Geophys. Research, v. 75, p. 2003–2027.

Swann, G. A., Bailey, N. G., Batson, R. M., and others, 1971, Preliminary geologic investigations of the Apollo 14 landing site, *in* Apollo 14 preliminary science report: Natl. Aeronautics and Space Admin. Spec. Publ. NASA SP-272, p. 39–85.

Swift, H. F., McGetchin, T. R., Preonas, D. D., and Johnson, S. W., 1970, Apollo 12 Lunar Module impact—Laboratory simulation and possible downrange ballistics effects: Science, v. 169, p. 851–854.

Tolch, N. A., and Bushkovitch, A. V., 1947, Penetration and crater volume in various kinds of rocks as dependent on caliber, mass, and striking velocity of projectile: Ballistic Research Labs., Aberdeen Proving Ground, Md., Rept. 641, 22 p.

Trask, N. J., 1966, Size and spatial distribution of craters estimated from Ranger photographs, *in* Rangers VIII and IX, pt. II—Experimenters' analyses and interpretations: California Inst. Technology Jet Propulsion Lab. Tech. Rept. 32–800, p. 252–263.

U.S. Army Corps of Engineers, 1953, The unified soil classification system: U.S. Army Corps Engineers Waterways Expt. Sta. Tech. Memo 3–357, 30 p., 9 pls.

———1958a, Cratering effects of surface and buried HE charges in loess and clay: U.S. Army Corps Engineers Waterways Exp. Sta. Tech. Rept. 2–482, 18 p., 47 pls.

———1958b, Effects of a soil-rock interface on cratering: U.S. Army Corps Engineers Waterways Exp. Sta. Tech. Rept. 2–478, 28 p.

U.S. Bureau of Reclamation, 1963, Earth manual, 1st ed.: U.S. Govt. Printing Office, Wash., D.C., 783 p.

Vanzant, B. W., 1963, Dynamic rock penetration tests at atmospheric pressure, *in* Fairhurst, C., ed., Rock mechanics; Proceedings of Fifth Symposium on Rock Mechanics, University of Minnesota, May 1962: New York, Pergamon Press, MacMillan Co., p. 61–91.

Vortman, L. J., 1963, Cratering experiments with large high-explosive charges: Geophysics, v. 28, no. 3, p. 351–368.

Vortman, L. J., and others, 1960, Project Buckboard, 20-ton and ½-ton high explosive cratering experiments in basalt rock: Project Plowshare, Final Report Sandia Corp., SC-4675(RR) TID-4500, 308 p.

Whitaker, E. A., 1972, Artificial lunar impact craters: Four new identifications, *in* Apollo 16 preliminary science rept., Pt. 1: Natl. Aeronautics and Space Admin. Spec. Rept. NASA SP-315, p. 29–30 to 29–45.

Wilshire, H. G., Stuart-Alexander, D. E., and Jackson, E. D., 1973, Apollo 16 rocks—Petrology and classification: Jour. Geophys. Research, p. 2379–2392.

Wosinski, J. F., Williams, J. P., Korda, E. J., Kane, W. T., Carrier, G. B., and Schrurs, W. W. H., 1972, Inclusions and interface relationships between glass and breccia in lunar sample 14306,50, *in* Proceedings Third Lunar Science Conference: Geochim. et Cosmochim. Acta Suppl. 3, M.I.T. Press, v. 1, p. 853–864.

Young, C. W., 1967a, The development of empirical equations for predicting depth of an earth-penetrating projectile: Sandia Labs. Rept. SC–DR–67–60, 41 p.

———1967b, Low velocity penetration tests in natural earth targets of selenite and gypsite: Sandia Corp. Rept. SC–DR–66–2695, 102 p.

TABLE 3.—*Data on missile impacts—lithologic description and physical parameters*

Target				Projectile		Crater						Mapping		Photographs
Crater No.	Material	Geology	Density g/cm³	Kinetic energy, 10^{14} ergs	Impact angle, (°)	Apparent depth d_a, cm	Apparent radius r_a, cm	Rim radius r_r, cm	Rim height $\bar{h}$, cm	Apparent volume V_a, 10^6cm³	Displaced mass M_d, 10^6 grams	Mappers	Date	White Sands Nos. and others
1	Fine sand (SP), uniform, light brown, nonplastic cohesionless to weakly cohesive, dry to moist	Dune	1.6	3.62	56.2	85	120	137	----	1.55	2.47	H. J. Moore SP/4 G. Hensz	4/64	29-040-2296-2651 to 2653 AFMDC, and aerials
2	Sandstone (rock), fine- to medium-grained, nonplastic, sorted, light tan, indurated, dry	Sandstone	2.5	5.72	56.8	76	160	172	7	1.37	3.42	H. J. Moore Lt. B. Hughes	4/64	29-040-1917-2473 to 2478 AFMDC and aerials
3	Silt (ML), very pale orange, LL-30, PL-25; low cohesion, dry to moist	Soil	1.1	6.51	50.4	49	114	126	25	1.05	1.16	R. Kachadoorian	2/64	AFMDC
4	Silty fine sand (SM), pale-yellow-brown, nonplastic fines, low cohesion, dry to moist	Alluvium	1.4	5.92	50.4	58	123	164	18	1.60	2.24	R. Kachadoorian	2/64	AFMDC
5	Silty fine sand (SM), pale-yellow-brown, nonplastic fines, low cohesion, dry to moist	Alluvium	1.4	4.58	51.4	55	112	125	----	1.23	1.72	R. Kachadoorian	2/64	AFMDC
6	Silt, sandy (ML), mod. orange-pink LL-32, PL-24, low cohesion, dry to moist	Alluvium	1.4	13.8	46.4	98	220	238	40	7.68	10.8	H. J. Moore H. Wilshire	7/64	AFMDC
7	Coarse-silty to clayey sand, crystalline well-graded (SM-SC), very light gray cohesive LL-20, PL-17, water saturated, water to ≈ 30%, gypsum lake beds	Gypsum	1.2–1.6	15.7	45.9	198	402	463	48	46.1	73.8	H. J. Moore H. Wilshire	8/64	29-040-4084-5284 to 5290 AFMDC and aerials
8	Silt (ML), very pale orange, low cohesion, dry to moist	Alluvium	1.45	4.23	56.2	61	102	113	11	1.81	2.62	R. Kachadoorian W. Quaide	11/64	None
9	Sandstone (rock), medium-grained(?), light tan, nonplastic indurated, dry	Sandstone	≈2.5	5.70	56.2	≈61	≈140	≈140	----	2.0 (est.)	5.0 (est.)	R. Kachadoorian W. Quaide	11/64	None
10	Sand, silty (SM), well-graded, pale reddish brown, LL-26, PL-25, low cohesion, dry to moist	Alluvium	1.5	2.95	56.8	61	98	110	5	.78	1.17	H. J. Moore R. Kachadoorian	11/64	None
11	Clay, sandy (CL), light gray, grains of gypsum, LL-14, PL-28, high cohesion, moist	Gypsum lake beds	1.98	5.92	51.0	82	146	180	23	2.27	4.50	H. J. Moore R. Kachadoorian	1/65	Unclassified negatives held by U.S. Geological Survey
12	Silt (ML), pale-yellow-brown, LL-34, PL-32, cohesion low, water 4.9 percent	Alluvium	1.21	5.21	51.0	76	115	125	8	1.68	2.03	R. Kachadoorian H. J. Moore	2/65	None
13	Sand (SP), fine-grained, uniform, light brown, very low cohesion, dry to moist	Dune	1.55	6.63	51.0	85	122	137	12	1.34	2.08	R. Kachadoorian H. J. Moore	2/65	29-040-0382-2535, 39, 41
14	Clay, sandy (CL), light gray, grains of gypsum, LL-14, PL-28, high cohesion, moist, lake beds	Gypsum lake bed	1.98	2.65	56.6	61	112	150	23	.90	1.78	H. Holt P. Margolin		
15	Clayey silts (ML), pale yellow, brown, LL-27, PL-26, low cohesion, dry to moist	Colluvium	1.16–1.34	24.1	45.7	150	259	281	29	13.5	17.0	H. J. Moore R. Kachadoorian	5/65	29-040-3152-6194 to 6219
16	Sand, gravelly, silty (SM), pale yellow, brown, LL-27, PL-23, low cohesion, dry to moist	Colluvium	1.33–1.4	31.4	45.0	160	280	314	31	17.1	23.0	H. J. Moore R. Kachadoorian	5/65	29-040-3153-6157 to 6176
17	Silts and very fine sand (CL-ML), grayish-orange, LL-18, PL-14, low cohesion, dry to moist gypsiferous over sandy silt (ML), uniform pale-yellow-brown, LL-32, PL-23, high cohesion, dry to moist fixed gypsum dune	Alluvium	1.42–1.46	19.7	45.0	140	266	317	27	16.4	24.0	H. J. Moore	6/65	29-040-3154-6177 to 6193
18	Sandy silt (ML), uniform, pale-yellow-brown, LL-32, PL-23, high cohesion, dry to moist, fixed	Fixed gypsum dune	1.40–1.44	24.1	45.7	160	255	314	27	17.7	25.0	H. J. Moore	6/65	29-040-3155-6561 to 6572
19	Clayey silt (ML), very pale orange, LL-30, PL-25, moderate cohesion, water 12%, moist		1.33	20.7	46.0	159	278	304	32	15.4	20.5	H. J. Moore D. Cummings	10/65	29-040-5099-11024 to 11043
20	Clayey silt (ML) and silty clay, pale-yellowish-brown, LL-43, PL-40, moderate cohesion, water 6–10%		1.9–2.1	25.2	45.8	177	312	360	31	18.1	36.0	H. J. Moore H. Holt	10/65	29-040-5099-11044 to 11063

TABLE 3.—*Data on missile impacts—lithologic description and physical parameters — Continued*

Target				Projectile		Crater						Mapping		Photographs
Crater No.	Material	Geology	Density g/cm³	Kinetic energy, 10^{14} ergs	Impact angle, (°)	Apparent depth d_a, cm	Apparent radius r_a, cm	Rim radius r_r, cm	Rim height $\bar{h}$, cm	Apparent volume V_a, 10^6 cm³	Displaced mass M_d, 10^6 grams	Mappers	Date	White Sands Nos. and others
21	Sandy silt (ML), grayish-red, LL-34, PL-30, low cohesion, water ≈ 3%	Soil and colluvium	1.7–1.8	2.10	58.0	70	125	165	8	1.49	2.61	H. J. Moore R. Kachadoorian H. Holt	1/66	29-040-0268-1120 to 1139
22	Sandstone(?) (rock), dry	Rock	≈2.5	2.90	58.0	----	----	----	----	----	----	Not mapped	----	29-040-0268-1140 to 1142
23	Limestone(?) (rock), dry	Rock	≈2.7	2.90	58.0	⟨35	----	≈50	----	----	----	Estimated from photograph	----	29-040-0268-1143 to 1147
24	Silty fine sand (SM), uniform, to well-graded in upper part, LL-25, PL-25, sandy silt (ML), nonplastic in lower part, light brown, low cohesion in upper part, moderate cohesion in lower part, water 2–7 percent	Sand-alluvium	1.64–1.81	25.1	45.8	171	265	305	26.0	13.4	23.1	H. J. Moore H. Holt J. M'Gonigle	6/66	29-040-2984-6326 to 6364
25	Silty sand (SM), and silty, clayey sand (SC), light to moderate brown, LL-23, PL-20, moderate cohesion, dry to moist		1.74–2.03	25.1	45.8	134	256	286	16	8.30	15.7	H. J. Moore J. M'Gonigle	6/66	29-040-2988-6323 to 6381
26	Sand, dune	Dune		25.1	45.8	----	----	----	----	----	----	Not mapped		29-040-2167-6325 to 6367
27	Not sampled but like crater 6	Alluvium	1.4 (est)	13.5	47.8	116	182	199	13	5.50	7.70	D. Cummings D. Gault	7/66	29-040-3277-7535 to 7538
28	Sandy silt (ML), uniform, pale-yellow-brown, LL-32, PL-23, high cohesion, water 1–6 percent	Fixed gypsum dune	1.37–1.56	15.8	47.0	119	233	257	21	11.0	16.1	H. J. Moore D. Cummings	7/66	29-040-3277-7526, 27 29-040-5106-10880 to 10882
29	Sandy silt (ML), uniform, pale-yellow-brown, LL-32, PL-23, high cohesion, water 1–6 percent	Fixed gypsum dune	1.37–1.56	15.8	47.0	107	215	257	38	6.98	10.3	H. J. Moore D. Cummings	7/66	29-040-3277-7532 to 7534 29-040-5106-10876 to 10883
30	Sandy silt (ML), uniform, pale-yellow-brown, LL-32, PL-23, high cohesion, water 1–6 percent	Fixed gypsum dune	1.37–1.56	15.8	47.0	104	182	206	28	5.20	7.65	H. J. Moore D. Cummings	7/66	29-040-3277-7530, 31 29-040-5106-10878 to 10886
31	Sand, silty (SM), well-graded, light brown, nonplastic fines, low cohesion, water 5 percent	Alluvium	1.56–1.77	20.4	46.4	127	237	279	16	9.49	15.8	H. J. Moore N. J. Trask	10/66	29-040-5108-10837 to 10862
32	Sand, silty (SM), well-graded light brown, nonplastic fines, low cohesion, water 4 percent	Alluvium	1.56–1.77	20.4	46.4	131	226	257	23	10.9	18.1	H. J. Moore N. J. Trask	10/66	29-040-5108-10839 to 10859
33	Sand, silty (SM), well-graded, light brown, nonplastic fines, some boulders brought to surface, low cohesion, dry to moist	Alluvium	1.56–1.77	20.4	46.4	94	210	255	23	8.27	13.6	H. J. Moore N. J. Trask	10/66	29-040-5108-10838 to 10860
34	Not sampled but like crater 6	Alluvium	1.4 (est)	20.7	46.2	152	270	312	≈36	13.6	19.0	J. D. Crossen J. M'Gonigle	10/66	29-040-5112-10891 to 10909
35	Silt (ML), pale-yellow-brown, nonplastic, low cohesion, dry to moist, overlying very pale orange sand (SM), nonplastic fines composed of gypsum, well-graded, low to moderate cohesion, water 6 percent	Alluvium	1.42	13.5	47.8	----	----	----	----	----	----	Cross section		29-040-0964-2769 to 2803
36	Silt (ML), pale-yellow-brown, nonplastic, overlying very pale orange sand (SM), nonplastic fines composed of gypsum, well-graded, low to moderate cohesion, water 2–6 percent	Alluvium, gypsum lake beds	1.42	13.5	47.8	97	220	251	18	6.03	8.58	H. J. Moore J. F. McCauley	3/67	29-040-0964-2793 to 2811
37	Sandy silt (ML), uniform, pale-yellow-brown, LL-32, PL-23, high cohesion, water 1–6 percent	Fixed gypsum dune	1.37–1.55	16.0	48.0	88	231	259	24	6.84	9.99	H. J. Moore R. Kachadoorian	3/67	29-040-1059-3956 to 3987
38	Sandy silt (ML), uniform, pale-yellow-brown, LL-32, PL-23, high cohesion, water 1–6 percent	Fixed gypsum dune	1.37–1.55	16.0	48.0	121	252	286	33	10.7	15.6	H. J. Moore R. Kachadoorian	3/67	29-040-1059-3958 to 3978
39	Sandy silt (ML), uniform, pale-yellow-brown, LL-32, PL-23, high cohesion, water 1–6 percent	Fixed gypsum dune	1.37–1.56	16.0	47.0	136	224	283	40	9.86	14.4	H. J. Moore J. F. McCauley	6/67	29-040-2632-5836 to 5841 29-040-2986-6202 to 6213
40	Sandy silt (ML), uniform, pale-yellow-brown, LL-32, PL-23, high cohesion, water 1–6 percent	Fixed gypsum dune	1.37–1.56	16.0	47.0	140	249	281	17	14.4	21.1	H. J. Moore J. F. McCauley	6/67	29-040-2632-5827 to 5843
41	Sandy silt (ML), uniform pale-yellow-brown, LL-32, PL-23, high cohesion, water 1–6 percent	Fixed gypsum dune	1.47–1.51	81.0	42.3	188	350	400	32	33.9	50.5	H. J. Moore J. F. McCauley	6/67	None
42	Sandy silt (ML), moderate brown, LL-36, PL-31, low cohesion, dry to moist	Colluvium	1.2–1.5	13.8	48.0	122	210	236	15	9.33	13.5	H. J. Moore J. F. McCauley	6/67	29-040-2631-5809 to 5815
43	Silt (ML), pale-yellow-brown nonplastic, low cohesion, dry to moist	Gypsiferous alluvium	1.4	16.5	47.0	64	144	182	19	1.38	1.59	H. J. Moore G. Ulrich T. Offield	9/67	29-040-4506-9774 to 9797

TABLE 3.—*Data on missile impacts—lithologic description and physical parameters — Continued*

Target				Projectile		Crater						Mapping		Photographs
Crater No.	Material	Geology	Density g/cm³	Kinetic energy, 10^{14} ergs	Impact angle, (°)	Apparent depth d_a, cm	Apparent radius r_a, cm	Rim radius r_r, cm	Rim height $\bar{h}$, cm	Apparent volume V_a, 10^6cm³	Displaced mass M_d, 10^6 grams	Mappers	Date	White Sands Nos. and others
44	Silt, sandy to clayey (NL), yellowish brown, layered, LL-31 to 38, PL-20 to 32, plasticity low to medium, moderate to low cohesion, water saturated, moist to 30 percent	Gypsum lake beds	1.85	44.6	25.1	218	486	562	43	83.4	154.0	H. J. Moore G. Ulrich T. Offield	9/67	Seven, no numbers
45	Sandy clay (CL), pale-yellow-brown, LL-34, PL-16, moderate cohesion, water 6–7 percent	Alluvium	1.36	14.4	47.5	155	265	284	21	11.3	15.4	H. J. Moore R. Kachadoorian P. Margolin	11/67	29-040-5931-11466 to 11483
46	Sand (SW), uniform, grayish orange-pink, very low cohesion, water 0–6 percent	Gypsum dune	1.35	14.4	47.5	152	242	283	18	9.33	12.6	H. J. Moore R. Kachadoorian P. Margolin	11/67	29-040-5831-11464 to 11478
47	Sand (SW), uniform grayish orange-pink, very low cohesion, water 0–6 percent	Gypsum dune	1.35	14.4	47.5	152	250	301	15	13.6	18.3	H. J. Moore R. Kachadoorian P. Margolin	11/67	29-040-5831-11465 to 11484
48	Clay, sandy (CL), light gray, gypsum, LL-14, PL-28, high cohesion, water 7–13 percent	Gypsum lake beds	1.98 (est.)	6.45	34.8	88	144	164	12	2.62	5.19	H. J. Moore P. Margolin	11/67	None
49	Sand, silty (SM), pale reddish-brown, nonplastic fines, low cohesion, water 0–5 percent	Alluvium-colluvium	1.54	2.09	60.6	52	109	125	9	1.02	1.57	H. J. Moore P. Margolin	3/68	29-040-1181-3164 to 3179
50	Silt (ML), very light gray, LL-35, PL-28, high cohesion, water 7–13 percent	Gypsum lake beds	1.85	23.2	46.2	179	308	370	55	25.9	48.0	H. J. Moore P. Margolin L. Youd	6/68	29-040-2947-6143 to 6157
51	Silt (ML), very light gray, LL-35, PL-28, high cohesion, water 7–13 percent	Gypsum lake beds	1.80	24.1	46.2	189	326	368	58	27.1	48.7	H. J. Moore P. Margolin L. Youd	6/68	29-040-2947-6143 to 6157
52	Silt (ML), very light gray, LL-35, PL-28, high cohesion, water 7–13 percent	Gypsum lake beds	1.80	23.5	46.2	192	335	369	40	29.1	52.4	H. J. Moore H. Wilshire S. Kieffer	11/68	29-040-C-5578-10330 to 10344
53	Sand, silty (SM), light brown, uniform, nonplastic fines, moderate cohesion, water 3.2 percent	Alluvium	1.5–1.6	69.6	40.6	194	328	368	15	24.1	38.6	H. J. Moore R. Kachadoorian S. Kieffer	1/69	29-040-C-0214-1387 to 1404
54	Clay, sandy (CL), very pale orange, LL-20, PL-18, moderate cohesion, water 4.6 percent	Alluvium	1.5–1.6	13.5	52.0	69	174	200	29	3.16	4.86	H. J. Moore H. Wilshire	4/69	Not numbered
55	Clay, sandy (CL), pale yellow brown, nonplastic, moderate cohesion, water 2.6 percent	Alluvium	1.6–1.7	14.5	52.0	84	172	199	19	3.27	5.23	H. J. Moore H. Wilshire	4/69	Not numbered
56	Sand (SP), fine-grained, uniform, very pale orange, very low cohesion, water 0–3 percent	Gypsum dune	1.4	73.5	36.5± 5	290	470	506	30	97.5	136.0	H. J. Moore S. Kieffer	6/69	29-040-C-2627-4732 to 4749
57	Not sampled but like crater 15	Alluvium		15.8	47.0	88	----	205	≈25	----	----	Not mapped		24-040-C-3277-7528, 29, 29-040-5106-10885
58	Sand, silty (SM), well-graded, some boulders and cobbles brought to surface	Colluvium	≈2.0	50.0	35.0	140	286	315	8	13.9	27.8	H. J. Moore R. Kachadoorian	1/73	29-040-0031-0164 to 0180
59	Not sampled but like crater 6	Alluvium	1.4 (est.)	13.5	47.8	116	----	214	----	----	----	Not mapped		29-040-3277-7535 to 7538
60	Not sampled but like crater 6	Alluvium	1.4 (est.)	13.5	47.8	76	----	214	----	----	----	Not mapped		29-040-3277-7535 to 7538

TABLE 4.—*Data on explosive craters–lithologic description and physical parameters*

Target			Explosive				Crater						Mapping		Photographs
Crater No.	Material	Density ρ g/cm^3	Charge weight, lbs (TNT equiv.)	Energy, 10^{14} ergs	Depth of burst dob, ft	Scaled depth of burst λ, ft/lb$^{1/3}$	Apparent depth d_a, cm	Apparent radius r_a, cm	Rim radius r_r, cm	Rim height h, cm	Apparent volume V_a, 10^6g	Displaced mass Md, 10^6g	Mappers	Date	White Sands Nos. and others
43–1	Silt (ML), pale yellow brown, nonplastic, low cohesion, dry to moist	1.4	100 (93)	17.7	1.31	0.29	92	187	219	15	3.77	5.28	H. J. Moore G. Ulrich G. Offield	9/67	29–040–4506 9974 to 9977 9979 to 9982
43–2			50 (47)	8.8	1.31	.36	52	176	195	11	2.29	3.21	H. J. Moore G. Ulrich T. Offield	9/67	9984, 9985 9987, 9990 9992 to 9997
43–3			50 (47)	8.8	.66	.18	56	145	175	7	1.40	1.96	H. J. Moore G. Ulrich T. Offield	9/67	
49–1	Sand, silty (SM), pale reddish brown, nonplastic fines, low cohesion, water 0–5 percent	1.5	5 (4.66)	.88	.83	.5	46	101	113	2	.55	.85	H. J. Moore P. Margolin	3/68	None
49–2			10 (9.32)	1.77	.54	.25	58	105	130	9	.82	1.26	H. J. Moore P. Margolin	3/68	
49–3			10 (9.32)	1.77	1.08	.51	58	115	143	13	1.26	1.94	H. J. Moore P. Margolin	3/68	
49–4			10 (9.32)	1.77	2.17	1.03	92	149	163	7	2.71	4.17	H. J. Moore P. Margolin	3/68	
49–5			20 (18.6)	3.54	1.33	.5	79	151	176	13	2.79	4.30	H. J. Moore P. Margolin	3/68	
49–6			5 (4.66)	.88	.83	.5	44	94	114	6	.58	.89	H. J. Moore P. Margolin	3/68	
L–7	Sand, clayey (SC), pale reddish brown, plastic fines, low cohesion, colluvium	1.54	20 (18.6)	3.54	1.58	.6	71	145	176	16	2.81	4.33	H. J. Moore R. Kachadoorian	2/68	None
L–8	Silt, clayey (MH), pale reddish brown, LL-53, PL-39, low cohesion, alluvium	2.07	75 (69.9)	13.3	1.31	.32	96	199	229	~9	6.20	12.83	H. J. Moore R. Kachadoorian	2/68	

GPO 690-250